Coarse-grained molecular-dynamics simulations of segmental motion and mechanical properties in polymer films and nanocomposites

Citation for published version (APA):
Davris, T. (2017). *Coarse-grained molecular-dynamics simulations of segmental motion and mechanical properties in polymer films and nanocomposites*. [Phd Thesis 1 (Research TU/e / Graduation TU/e), Applied Physics and Science Education]. Technische Universiteit Eindhoven.

Document status and date:
Published: 02/02/2017

Document Version:
Publisher’s PDF, also known as Version of Record (includes final page, issue and volume numbers)

Please check the document version of this publication:

• A submitted manuscript is the version of the article upon submission and before peer-review. There can be important differences between the submitted version and the official published version of record. People interested in the research are advised to contact the author for the final version of the publication, or visit the DOI to the publisher's website.
• The final author version and the galley proof are versions of the publication after peer review.
• The final published version features the final layout of the paper including the volume, issue and page numbers.

Link to publication

General rights
Copyright and moral rights for the publications made accessible in the public portal are retained by the authors and/or other copyright owners and it is a condition of accessing publications that users recognise and abide by the legal requirements associated with these rights.

- Users may download and print one copy of any publication from the public portal for the purpose of private study or research.
- You may not further distribute the material or use it for any profit-making activity or commercial gain
- You may freely distribute the URL identifying the publication in the public portal.

If the publication is distributed under the terms of Article 25fa of the Dutch Copyright Act, indicated by the “Taverne” license above, please follow below link for the End User Agreement:

www.tue.nl/taverne

Take down policy
If you believe that this document breaches copyright please contact us at:

openaccess@tue.nl

providing details and we will investigate your claim.

Download date: 04. Oct. 2023

Coarse-grained molecular-dynamics simulations of segmental motion and mechanical properties in polymer films and nanocomposites

Theodoros Davris

A catalogue record is available from the Eindhoven University of Technology Library

ISBN: 978-94-028-0480-5

Cover design by: Theodoros Davris

Printed by: Ipskamp Printing

This work is part of the FOM Foundation’s research project #11VEC06. It was also sponsored by the Stichting Nationale Computerfaciliteiten (National Computer Facilities Foundation, NCF) through the usage of its supercomputer facilities, with financial support from the Nederlandse Organisatie voor Wetenschappelijk Onderzoek (Netherlands Organization for Scientific Research, NWO).

Copyright © 2016 by Theodoros Davris

Coarse-grained molecular-dynamics simulations of segmental motion and mechanical properties in polymer films and nanocomposites

PROEFSCHRIFT

ter verkrijging van de graad van doctor aan de Technische
Universiteit Eindhoven, op gezag van de rector magnificus
prof.dr.ir. F.P.T. Baaijens, voor een commissie aangewezen door
het College voor Promoties, in het openbaar te verdedigen op
donderdag 2 februari 2017 om 16:00 uur

door

Theodoros Davris

geboren te Marousi, Griekenland

Dit proefschrift van het proefontwerp is goedgekeurd door de promotoren en de samenstelling van de promotiecommissie is als volgt:

voorzitter: prof. dr. ir. G.M.W Kroesen
promotor: prof. dr. M.A.J. Michels
copromotor: dr. A.V. Lyulin
leden: prof. dr. D. Bonn (University of Amsterdam)
dr. A.R.C. Baljon (San Diego State University)
dr. A. Simone (TU Delft)
prof. dr. P.A. Bobbert
prof. dr. F. Toschi

Het onderzoek of ontwerp dat in dit proefschrift wordt beschreven is uitgevoerd in overeenstemming met de TU/e Gedragscode Wetenschapsbeoefening.

Contents

1 Introduction..1
  1.1 The technological relevance of polymer nanocomposites........................ 2
  1.2 The mechanical properties of polymer nanocomposites 4
  1.3 Polymers under Confinement.. 7
  1.4 Outline of the Thesis 9
  References 10
2 Models and Methods..15
   2.1 Molecular-dynamics simulations: basic principles 16
      2.1.1 Chosen statistical ensembles 18
   2.2 Simulated polymer models... 19
      2.2.1 Film model... 21
      2.2.1 Particulate model.. 22
   2.3 System Creation and Equilibration.. 23
      2.3.1 Film model... 23
      2.3.2 Particulate model... 25
   2.4 Calculated Properties 26
      2.4.1 Structural Properties... 26
      2.4.2 Glass-Transition Temperature 27
      2.4.3 Dynamical Properties 28
      2.4.4 Mechanical Properties... 28
   References 30
3 Molecular-dynamics simulations of crosslinked polymer films: equilibrium structure and glass-transition temperature 33
  3.1 Introduction.. 34
  3.2. Models and Methods 35
     3.2.1 Model Description.. 35
     3.2.2 System Preparation and Equilibration.............................. 37

3.3 Results..39
  3.3.1 Effect of Cut-off Radius on the Density-Temperature Profile..........39
  3.3.2 Glass-Transition Temperature 40
  3.3.3 Local Structure and Density 43
3.4 Conclusions...46
References...47
4 A coarse-grained molecular-dynamics study of segmental structure and mobility in capped crosslinked copolymer films 49
4.1 Introduction...50
4.2 Simulated models and methods 53
4.3 Results and Discussion...58
  4.3.1 Glass-transition temperature 58
  4.3.2 Segmental dynamics...59
  4.3.3 Effect of wall structure 65
4.4 Conclusions...70
References...71
5 Filler size effects on reinforcement in elastomer-based nanocomposites: experimental and simulational insights into physical mechanisms.........................75
5.1 Introduction...76
5.2 Experimental Materials and Methods 77
  5.2.1 Model systems...77
  5.2.2 Materials...77
  5.2.3 Rheological measurements 78
5.3 Simulation Models and Methods 78
5.4 Results..83
  5.4.1 Experimental results from UvA 83
  5.4.2 Simulations..87
    5.4.2.1 The simulated reinforcement of the film and particulate models 87

5.4.2.2 Comparison of the reinforcement among the particulate simulation model and the experimental samples 90
5.4.2.3 Microscopic mechanisms of reinforcement 93
5.5 Discussion and Conclusions 96
References 100
6 Molecular Mechanisms of the Payne Effect in Filled Elastomers: Insights from Computer Modeling 103
6.1 Introduction 104
6.2 Models and Methods 106
6.3 Computing moduli using LAOS simulations 108
6.4 Microscopic mechanisms of the strain hardening 113
6.5 Microscopic mechanisms of the Payne effect 119
6.6 Conclusions 122
References 122
7 Conclusions and Outlook 129

Chapter 1

Introduction

Abstract

The aim of the thesis is to study, using molecular-dynamics simulations, the mechanical properties of polymer nanocomposites — materials in which inorganic nanoparticles, commonly referred to as fillers, are added to rubbery polymers so as to increase their rigidity at low strain amplitudes: a phenomenon called "reinforcement." However, the addition of colloidal particles to any polymer matrix leads to the creation of a highly complicated system, and as a result, the precise mechanism of the reinforcement, and in general of the mechanical properties, is still not entirely understood. Although a variety of different interpretations have already been given on the subject, those interpretations are often inconsistent with one another. The main problem to be solved, besides the elucidation of the precise mechanism of the reinforcement, is the so-called Payne effect, exemplified by a loss of the gained rigidity at larger strain amplitudes. This loss of rigidity is the main obstacle that restrains the performance of this family of materials, and consequently, the furthering of their technological applications. The goal is to relate, using dynamic computer modeling, the viscoelastic properties of polymer nanocomposites to the motion of their constituent molecules, and those — in turn — to the molecular-level interactions, the final goal being the development of a method for the design of advanced materials with tailor-made mechanical properties, realized through the manipulation of the molecular interactions. The goal of this Chapter is to present a general overview of the research field, with more detailed descriptions given in Chapters 3-6.

1.1 The technological relevance of polymer nanocomposites

The subject of the thesis concerns the mechanical properties of polymer-based nanocomposites, *i.e.*, materials consisting of a polymer matrix in which solid nanoparticles are added so as to increase the rigidity of the matrix at small deformation amplitudes. Until recently, the most commonly utilized type of filler particles (especially by the tire industry) has been Carbon Black (CB) which is produced from the incomplete combustion of coal tar and ethylene. Its addition to rubbers results in the manufacturing of tires with a smaller rolling resistance. At the moment, the rolling resistance of car tires accounts for about 4% of the worldwide CO_2 emissions from fossil fuels [**1, 2**], and a decrease in the rolling resistance of about 10% is anticipated to decrease their overall fuel consumption by about 2–3% [**3**] — the reason being that a vehicle with tires of a smaller rolling resistance requires less energy to thrust forward. However, a smaller rolling resistance leads to a lower wet grip performance: an undesirable side effect as regards passenger's safety. The problem can be partially solved by adding silica to the tire, instead of CB, which enables manufacturers to produce "green tires" [**4**] that display both improved wet grip properties as well as a smaller rolling resistance [**5**].

Figure 1.1: Carbon black (left) and silica powder (right).

An important difference among CB and silica fillers is that the former is hydrophobic whereas the latter is hydrophilic. In order to increase the compatibility among the silica fillers and the polymer matrix, the fillers are functionalized with coupling agents [**23-25**]. By tuning the interactions among the silica particles and the polymer matrix, nanocomposites with specific properties can be produced. Despite their obvious importance, though, filler-polymer interactions have remained poorly understood, owing to a lack of suitable theoretical and experimental approaches. The key issue that remains unresolved is the exact mechanism of the rubber reinforcement itself and of the so-called Payne effect, both of which will be described forthwith.

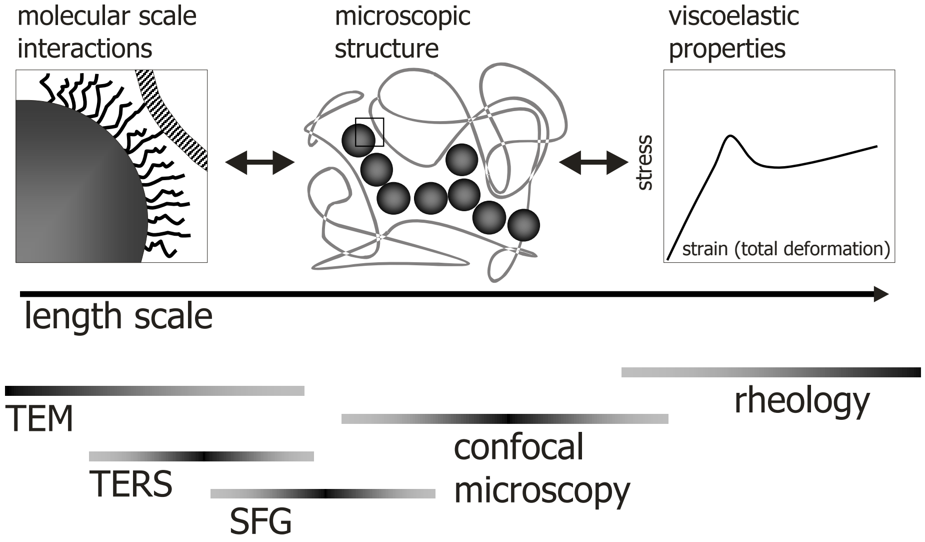
molecular scale interactions
microscopic structure
viscoelastic properties
stress
strain (total deformation)
length scale
TEM
TERS
SFG
confocal microscopy
rheology

Figure 1.2: Schematic representation of the different length-scales involved in the thesis: the aim is to elucidate the relations between the molecular-scale interactions at the nanoparticle surface, the microscopic structure of the composite that results from these interactions, and the resulting viscoelastic properties of the material. Relevant experimental techniques according to the probed length-scales are also denoted in the bottom of the figure (TEM = transmission electron microscopy; TERS = tip-enhanced Raman spectroscopy; SFG = sum frequency generation spectroscopy).

The main question (whose elucidation is of paramount importance for industries developing or utilizing polymer composites) is how to relate the filler-matrix adhesion interactions to the microstructure of the composite, and that to its macroscopic, non-linear elastic behavior (Fig. 1.2). The thesis aims to contribute to that goal by performing molecular-dynamics simulations of polymer nanocomposites in close collaboration with experimental groups performing rheological measurements. Two different simulation models have been used, each representing a different length-scale of the system — namely, we simulated polymers confined between solid walls, and polymers filled with nanoparticles, as depicted in Fig. 1.3.

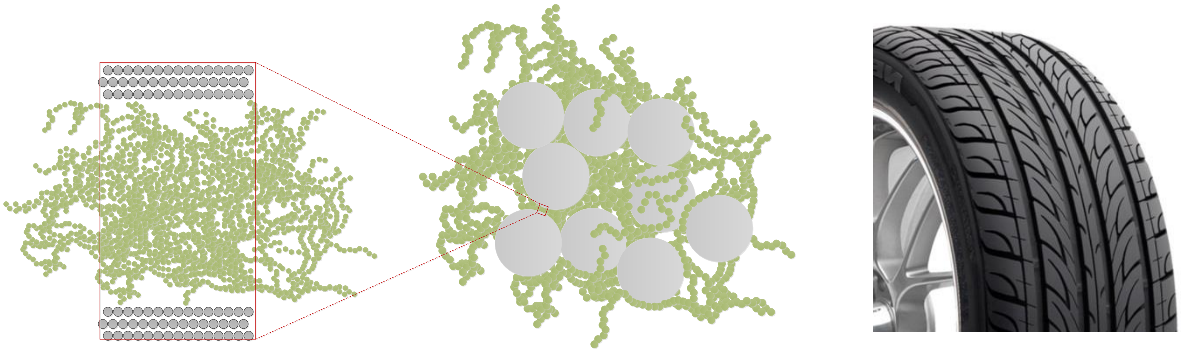

Figure 1.3: Illustration of the different length-scales which are relevant to the study of the mechanical properties in polymer nanocomposites. The figure depicts a car tire, its microstructure, consisting of the grey nanoparticles and the green polymer matrix, and a polymer film representing the volume between two nanoparticles.

1.2 The mechanical properties of polymer nanocomposites

The distinctive characteristics of the mechanical properties of polymer nanocomposites are the so-called *reinforcement* and the *Payne effect*, which are seemingly interlinked to each other, and are discussed in the 2nd Chapter of the thesis. In relation to the mechanical properties of the unfilled polymer, the reinforcement denotes an increase in the rigidity of the material at low strain amplitudes after the addition of the filler particles. Depending on the application, it is a desirable aspect of the nanocomposite. However, when the strain amplitude is further increased, the gained rigidity is abruptly lost; and although it still remains higher than that of the pure polymer, it brings about the consequence that current composites cannot be used in applications where high rigidity at large strain amplitudes is required. The loss of rigidity, in the case of polymer nanocomposites, is colloquially referred to as “the Payne effect” by the name of the scientist who first noticed the phenomenon [**6, 7**].

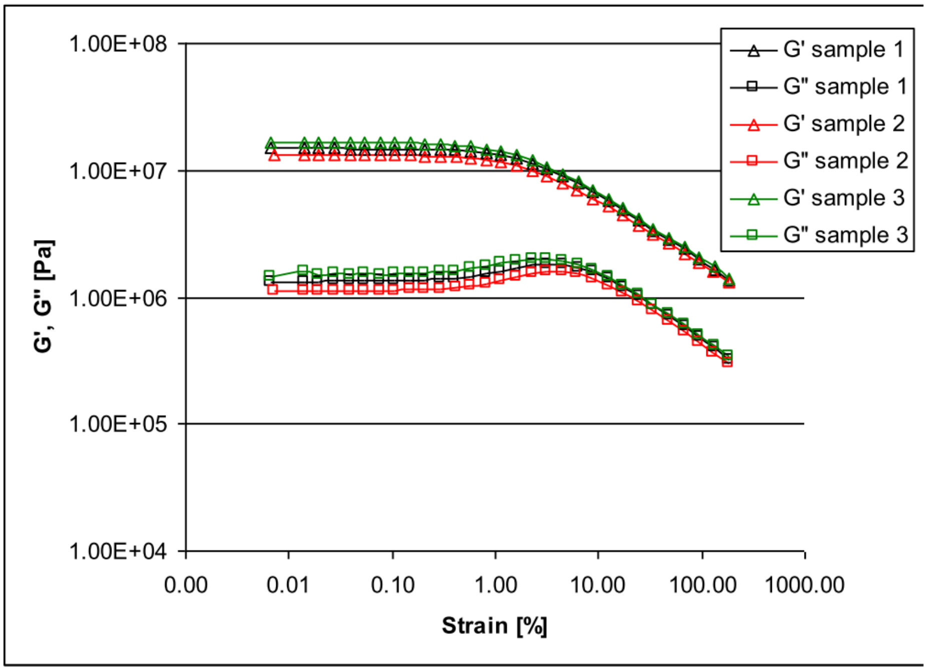

Figure 1.4: Strain-dependence of the storage and viscous moduli obtained by oscillatory strain sweeps of NBR rubber with silica nanoparticles. The data were provided by our experimental partners at SKF.

A great amount of literature has been devoted to the subject [**9-31**]. However — and despite the strenuous effort on behalf of both the experimental and the computational scientific community — a consensus has not yet been established. Overall, there are two distinct opinions regarding the molecular origins of the excess reinforcement, in addition to the reinforcement induced by the mere presence of rigid nanoparticles: one attributes it exclusively to the aggregation of the nanoparticles, whereas the other to the formation of filler-polymer interphases. Seemingly, at high particle loadings, the reinforcement occurs due to particle jamming, whereas at low particle loadings the main contributor seems to be the strong filler-polymer interactions which might lead to the densification of the polymer matrix near the nanoparticles as well as to the formation of a sturdy filler-polymer-filler network with approximately infinite relaxation times [**15-17**]. In order to clarify the relative contribution of those two reinforcing mechanisms, an extensive molecular-dynamics study of amorphous polymers filled with solid nanoparticles was performed, under equilibrium conditions [**18**]. The conclusion of the study was that the experimentally observed mechanical reinforcement may result from either one of the proposed mechanisms (either from particle agglomeration or from a polymer-induced filler network) with their relative contribution depending strongly on the filler-polymer interaction energy and range as well as on the dispersion and volume fraction of the filler particles.

The thesis focuses on the study of the filler-polymer interfaces, rather than of the agglomeration of the filler particles, under both equilibrium and non-equilibrium conditions. In this regard, the study of the glass-transition temperature of the polymer matrix is essential, since it is well known that the mechanical properties of a polymeric material are contingent on its glass-transition temperature, T_g, as well as on the underlining local segmental mobility of the polymer chains. Those properties are, at least locally, altered by the interfaces which are developed after the addition of the filler particles to the polymer matrix.

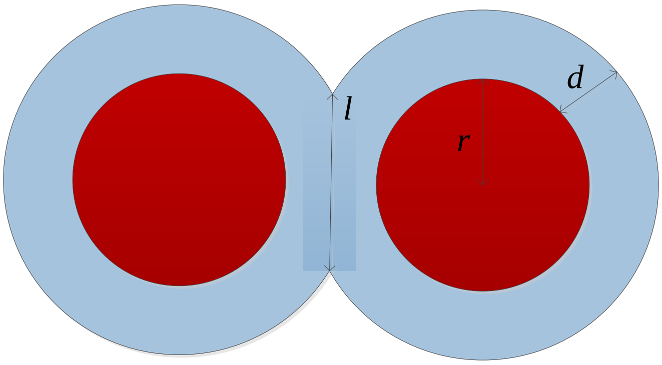

Figure 1.5: Schematic representation of two neighboring particles which are surrounded by a glassy layer of thickness *d*. The particles are connected by a glassy bridge of diameter *l*.

An approach to understand the reinforcement mechanisms in silica-filled model systems, based on the concept of the glass-transition temperature, was taken by Lequeux, Long *et al*. [**12, 13, 19-21**]. In those papers, the authors have proposed the existence of a gradient in the polymer glass-transition temperature near the silica interface, which was successfully related to the temperature- and frequency-dependent mechanical behavior of the composite. Then, the strain-induced softening of the percolating glassy bridges connecting the filler particles was held responsible for the observed nonlinear mechanical behavior (Fig. 1.5). However, the effect of adsorbing and non-adsorbing interfaces and of the confinement on the glass-transition temperature of the polymer matrix is still heavily debated, and no consensus exists about their relevance to the reinforcement [**22, 23**].

Since the focus in industry has been redirected towards the development of “green tires” in which the CB particles are replaced by silica particles, an important issue is related to the compatibility among the silica particles and the polymer matrix. The use of coupling agents [**24-26**], which leads to the well-controlled interaction between the non-polar polymer chains and the polar silica surface, may alleviate the problem. The importance of the filler surface energy has been examined by Gauthier *et al.* [**26**] on silica-filled SBR rubbers, by modifying the silica surface using different silanes. Their results showed that the presence of chemical links at the silica surface reduces the amplitude of the Payne effect. Based on that result, the authors attempted to provide a theoretical explanation of the Payne effect: the polymer chains are initially bound to the filler surface, but under the applied stress, they de-bond, thus causing the nonlinear mechanical behavior. The de-bonding effect has also been used in a recently proposed model for the explanation of the non-linear, large-strain mechanical behavior of nano-filled elastomers [**27**].

The majority of the above-mentioned studies have attempted to explain the Payne effect by focusing on the importance of the polymer-filler interactions and the development of glass bridges between the nanoparticles. Indeed, the behavior of a polymer under conditions of strong confinement is different than that in the bulk of the material. However, the assumed increase of rigidity due to overlapping glassy layers at high filler volume fractions, and its consequent drop under deformation, has not been verified experimentally. The difficulty arises due to the minuscule length-scales that are involved: the approaching surfaces of neighboring filler particles may result in a geometric confinement with a size on the scale of only a few nanometers, which is difficult to probe experimentally. Therefore, in order to provide insight on the nanoscopic mechanisms which might affect the mechanical properties of polymer nanocomposites, it is important to understand the dynamical and mechanical behavior of polymer films [**28**].

1.3 Polymers under Confinement

Various attempts to study the influence of the degree of confinement on the mechanical properties of polymer nanocomposites have deployed a film polymer model, aiming to establish a quantitative equivalence between the thermomechanical properties of the two systems [**312-345**]. Indeed, the properties of both systems are strongly influenced by adhesion interactions and by confinement effects, and, depending on the volume fraction of fillers in the nanocomposite, similarities have been undoubtedly identified. In highly filled polymer nanocomposites (40 wt%), it has been shown [**32**] that the changes in the glass-transition temperature with decreasing inter-particle spacing are *quantitatively* equivalent to the corresponding thin-film data. On the other hand, in materials with low filler concentration (less than 1.0 wt%), only a *qualitative* equivalence has been established [**32,35**].

The glass transition of thin polymer films has been also widely examined experimentally [**36-53**]. The general conclusion thus far is that the glass-transition of a polymer film (and by extension its dynamic response to external perturbations) depends mainly on the degree of confinement, the presence of free interfaces, and the polymer-wall interactions. However, due to the fact that the measured properties seem to be influenced by the employed experimental technique as well as by the preparation procedure of the samples, the reported results have shown disagreement among different laboratories and among different experimental methods [**54-61**]. Dynamic fragility (a measure of the glass transition abruptness of glass-forming materials) has also been employed in order to explain why different polymers, under the same conditions, are subjected to diversified confinement effects. Seemingly, under conditions of varying film thickness, correlations do exist among fragility and the amplitude of the T_g change [**62**].

Alongside the experimental studies, simulations of polymers under confinement have shown that a free interface, or the usage of repulsive interactions among the polymer and the solid walls, induces acceleration in the dynamical response of the polymer [**63-65**], whereas the use of attractive polymer-wall interactions has the opposite effect [**66, 67**]. Essentially, it has been confirmed that the glass-transition temperature in films is significantly different than that of the bulk, and mostly depends on interfacial phenomena [**68, 69**]. On the other hand, despite having closely attended to the effect of the degree of confinement and the adhesion interactions on the glass-transition temperature and the segmental dynamics in thin polymer films, the effect of crosslinks on the properties of confined polymers is much less investigated — especially with molecular-dynamics simulations [**70**].

1.4 Outline of the Thesis

In our effort to understand the mechanisms which give rise to the reinforcement and the Payne effect, in close collaboration with experimental groups, we performed molecular-dynamics simulations of polymer nanocomposites on two different length-scales; namely, we studied polymer films (Chapters 3 and 4) in which the polymer was capped between two solid walls, and particulate polymer systems (Chapters 5 and 6) in which nanoparticles were added to the bulk polymer. Thus, our effort was focused on molecular-level phenomena which are difficult to probe in experiments. The main goal of the thesis is to study the influence of the nanoparticles on the structural, dynamical, and mechanical properties of the polymer matrix. The most important questions the thesis aims to answer are:

- How do confinement and crosslinking effects affect the structural and dynamical properties of the confined polymer?”
- What is the effect of the filler surface structure on the microscopic and elastic properties of the composite?
- To what extent the amount of fillers, the size of the nanoparticles, as well as the interactions among the nanoparticles, affect the reinforcement and the Payne effect in polymer nanocomposites?

The models used for the simulations are presented in Chapter 2. In that chapter we also describe the simulation protocols that were used so as to extract the microscopic properties of the systems that were to be correlated with their macroscopic mechanical properties.

Chapter 3 aims to analyze the equilibrium structure of the polymer films. Specifically we studied how the glass-transition temperature and the polymer density distribution are affected by the degree of confinement and the crosslink density of the confined polymer.

Chapter 4 aims to analyze the equilibrium multi-scale dynamics of the same polymer films presented in the previous chapter. Specifically we studied how the mobility of the polymer segments, on multiple length-scales along the backbone of a polymer chain, is affected by the structure of the solid walls, the degree of confinement, and the polymer crosslink density. In addition, we undertook to correlate those varying parameters to the underlying dynamical heterogeneity as well as the structural inhomogeneity induced to the polymer by the presence of the solid walls.

Chapter 5 aims to analyze the reinforcement in the particulate systems (which consisted of a polymer matrix and dispersed nanoparticles) which were uniaxially and linearly deformed. A comparison with experimental results, performed by our collaborators of the Soft Matter group at the Institute of Physics at the University of Amsterdam, is also included, as well as a comparison with shear-distortion models of the reinforcement which are commonly used in industry for the design of polymer nanocomposites. The volume fraction of the fillers, the radius of the nanoparticles, as well as the interaction strength among the nanoparticles, were varied, and their effect on the reinforcement was compared with experimental results conducted on industrial composites.

Chapter 6 aims to analyze the Payne effect in the particulate systems, by exposing them to large-scale oscillatory shear (LAOS) deformation. Specifically we studied how the Payne effect and the microscopic dynamics are affected by the nature of the direct interactions among the nanoparticles, thus providing a connection among the two. Furthermore, we explained microscopically the strain softening/hardening observed in polymer nanocomposites during LAOS deformations.

Finally, the main results and conclusions of the thesis are given in Chapter 7, along with suggestions of further research.

References

[1] Chu S., A. Majumdar, *Nature* **2012**, *488*, 294–303.

[2] Tullo A. H., *Chem. Eng. News* **2009**, *87*, 10–14.

[3] *The Tire Digest*, Michelin **2002**

[4] Holmberg K., Andersson P., Erdemir A., *Tribol. Int.* **2012**, *47*, 221–234.

[5] Byers J.T., *Rubber Chem. Technol*. **2002** *75*(3), 527-548.

[6] Payne A. R., *J. Appl. Polym. Sci*. **1962**, *6*, 57–63.

[7] Payne A. R., *J. Appl. Polym. Sci*. **1962**, *6*, 368–372.

[8] Wang M. J. Rubber Chem *Technol* **1998**, *71*, 520–89.

[9] Tjong S. C., *Mater. Sci. Eng. R-Rep* **2006**, *53*, 73–197.

[10] Allegra G., Raos G., Vacatello M., *Prog. Polym. Sci*. **2008**, *33*, 683–731.

[11] Ganesan V., Jayaraman A., Soft Matter **2014**, *10*, 13-38.

[12] Berriot J., Montes H., Lequeux F., Long D., Sotta P., *EPL* **2003**, *64*, 50-56.

[13] Montes H., Chaussée T., Papon A., Lequeux F., Guy L., *Eur. Phys. J. E Soft Matter* **2010**, *31*, 263-268.

[14] Papon A., Montes H., Lequeux F., Oberdisse J., Saalwächterc K., Guy L., *Soft Matter*, **2012**, *8*, 4090-4096.

[15] Pryamitsyn V., Ganesan V., *Macromolecules* **2006**, *39*, 844–856.

[16] Salaniwal S., Kumar S. K., Douglas J. F., *Phys. Rev. Lett.* **2002**, *89*, 258301.

[17] Adnan A., Sun C. T., Mahfuz H., *Compos. Sci. Technol*. **2007**, *67*, 348–356.

[18] Sen S., Thomin J. D., Kumar S. K., Keblinski P., *Macromolecules* **2007**, *40*, 4059–4067.

[19] Berriot J., Lequeux F., Monnerie L., Montes H., Long D., Sotta P., *J. Non-Cryst. Solids* **2002**, *307*, 719-724.

[20] Berriot J., Montes H. , Lequeux F., Long D., Sotta P., *Macromolecules* **2002**, *35*, 9756-9762.

[21] Montes H., Lequeux F., Berriot J., *Macromolecules* **2003**, *36*, 8107-8118.

[22] Robertson C. G., Lin C. J., Bogoslovov R. B., Rackaitis M., Sadhukhan P., Quinn J. D., Roland C. M., *Rubber Chem. Technol*. **2011**, *84*, 507-519.

[23] Robertson C. G., Rackaitis M., *Macromolecules* **2011**, *44*, 1177-1181.

[24] ten Brinke J. W., Litvinov V. M., Wijnhoven J. E. G. J., Noordermeer J. W. M., *Macromolecules* **2002**, *35*, 10026–10037.

[25] ten Brinke J. W., Debnath S., Reuvekamp L. A. E. M., Noordermeer J. W. M., *Compos. Sci. Technol.* **2003**, *63*, 1165 – 1174.

[26] Gauthier C., Reynaud E., Vassoille R., Ladouce-Stelandre L., *Polymer* **2004**, *45*, 2761–2771.

[27] Stockelhuber K., Svistkov A., Pelevin A., Heinrich G,. *Macromolecules* **2011**, *44*, 4366–4381.

[28] Rittigstein P., Priestley R. D., Broadbelt L. J., Torkelson J. M., *Nat. Mater*. **2007**, *6*, 278 – 282.

[29] Heinrich G., Klüppel M., Vilgis T.A., *Curr. Opin. Solid State Mater. Sci*. **2002**, *6*, 195-203.

[30] Heinrich G., Klüppel M., in *Filled elastomers drug delivery systems*, Springer: New York, 2002, 1-44.

[31] Klüppel M., in *Filler-Reinforced Elastomers/Sanning Force Microscopy*, Springer: New York, 2003, 1-86.

[32] Rittigstein P., Priestley R. D., Broadbelt L. J., Torkelson J. M., *Nat. Mater*. **2007**, *6,* 278 - 282

[33] Bansal A., Yang H., Li C., Cho K., Benicewicz B. C., Kumar S. K., Schadler L. S., *Nat. Mater*. **2005**, 4, 693-698.

[34] Sen S., Xie Y., Bansal A., Yang H., Cho K., Schadler L. S., Kumar S. K., *Eur. Phys. J. Special Topics* **2007**, *141*, 161-165.

[35] Kropka J. M., Pryamitsyn V., Ganesan V., *Phys. Rev. Lett*. **2008**, *101*, 075702.

[36] Keddie J. L., Jones R. A. L., *Europhys. Lett*. **1994**, *27*, 59–64.

[37] Keddie J. L., Jones R. A. L., Cory R. A., *Faraday Discuss*. **1994**, *98*, 219–230.

[38] Fryer D. S., Nealey P. F., de Pablo J. J., *Macromolecules* **2000**, *33*, 6439–6447.

[39] Lupascu V., Picken S. J., Wubbenhorst M. J., *Non-Cryst. Solids* **2006**, *352*, 5594–5600.

[40] Lupascu V., Huth H., Schick C., Wubbenhorst M., *Thermochim. Acta* **2005**, 432, 222–228.

[41] Hudzinskyy D., Lyulin A. V., Baljon A. R. C., Balabaev N. K., Michels M. A. J., *Macromolecules* **2011**, **44**, 2299–2310.

[42] Forrest J., Dalnoki-Veress K., Dutcher J. R., *J. Phys. Rev. E* **1997**, *56*, 5705.

[43] Serghei A., *Macromol. Chem. Phys*. **2008**, *209*, 1415–1423.

[44] Napolitano S., Wubbenhorst M., *Macromolecules* **2006**, *39*, 5967–5970.

[45] Herd C. R., McDonald G. C., Hess W. M., *Rubber Chem. Technol.* **1991**, *65*, 107.

[46] Herrchen M., Ottinger H. C., *J. Non-Newtonian Fluid Mech.* **1997**, *68*, 17.

[47] Karayiannis N. C., Kröger M., *Int. J. Mol. Sci.* **2009**, *10*, 5054.

[48] Stevens M. J., *Macromolecules* **2001**, *34*, 1411.

[49] Sharp J. S., Forrest J. A., *Phys. Rev. Lett.* **2003**, *91*, 235701.

[50] Bennemann C., Baschnagel J., Paul W., *Eur. Phys. J. B* **1999**, **10,** 323.

[51] Tsoloua G., Harmandaris V. A., Mavrantzas V. G., *J. Non-Newtonian Fluid Mech.* **2008**, *152*, 184.

[52] Glomann T., Hamm A., Allgaier J., Hübner E. G., Radulescu A., Farago B., Schneider G. J., *Soft Matter* **2013**, *9*, 10559.

[53] Arbe A., Colmenero J., Monkenbusch M., Richter D., *Phys. Rev. Lett.* **1998**, *81*, 590.

[54] Fryer D. S., Peters R. D., Kim E. J., Tomaszewski J. E., de Pablo J. J., Nealey P.F., White C.C., Wu W. L., *Macromolecules* **2001**, *34*, 5627.

[55] Kawana S. , Jones R.A.L., *Phys. Rev. E* **2001**, *63*, 021501.

[56] Ellison C. J., Kim S. D., Hall D. B., Torkelson J. M., *Eur. Phys. J. E* **2002**, *8*, 155.

[57] Inoue R., Kanaya T., Nishida K., Tsukushi I., Shibata K., *Phys. Rev. E* **2008**, *77*, 032801.

[58] Inoue R., Kanaya T., Nishida K., Tsukushi I., Telling M. T. F., Gabrys B. J., Tyagi M., Soles C., Wu W. I., *Phys. Rev. E* **2009**, *80*, 031802.

[59] Soles C. L., Douglas J. F., Wu W. L., Dimeo R. M., *Macromolecules* **2003**, *36*, 373.

[60] Soles C. L., Douglas J. F., Wu W. L., *J. Polym. Sci. Part B* **2004**, *42*, 3218.

[61] Soles C. L., Douglas J. F., Wu W. L., Peng H. G., Gidley D.W., *Macromolecules* **2004**, *37*, 2890.

[62] Evans C. M., Deng H., Jager W. F., Torkelson J. M., Macromolecules **2013**, *46*, 6091.

[63] Binder K., Baschnagel J., Paul W., *Prog. Polym. Sci*. **2003**, *28*, 115.

[64] Batistakis C., Lyulin A. V., Michels M. A. J., *Macromolecules* **2012**, *45*, 7282.

[65] Mansfield K. F., Theodorou D. N., *Macromolecules* **1991**, *24*, 6283.

[66] Batistakis C., Michels M. A. J., Lyulin A. V., *Macromolecules* **2014**, *47*, 4690.

[67] Starr F. W., Schrøder T. B., Glotzer S. C., *Phys. Rev. E* **2001**, *64*, 021802.

[68] Hudzinskyy D., Lyulin A. V., Baljon A. R. C., Balabaev N. K., Michels M. A. J., *Macromolecules* **2011**, *44*, 2299.

[69] Baljon A. R. C., Williams S., Balabaev N. K., Paans F., Hudzinskyy D., Lyulin A. V., *J. Polym. Sci. Pol. Phys*. **2010**, *48*, 1160.

[70] Baschnagel J., Binder K., Doruker P., Gusev A. A., Hahn O., Kremer K., Mattice W. L., Müller-Plathe F., Murat M., Paul W., Santos S., Suter U. W., and Tries V., *Adv. Polym. Sci*. **2000**, *152*, 41.

Chapter 2

Models and Methods

Abstract

The current chapter is devoted to the explanation of the computational models and of the simulation methods which were employed so as to study those models. It begins with an elementary review of the molecular-dynamics simulation method, and continues with a detailed description of the models which were simulated so as to calculate specific properties of polymer films and nanocomposites. The chapter concludes with a description of the simulation protocols through which those properties were extracted.

2.1 Molecular-dynamics simulations: basic principles

A simulation may be defined as the representation of the behavior or characteristics of a system through the use of a simpler one — especially of a computational model designed for the purpose. The molecular-dynamics (MD) simulation method, invented in the 1950's [1, 2], makes use of Newton's laws of classical mechanics so as to numerically draw the temporal evolution of molecular systems pertaining to a variety of materials such as liquids, glasses, solids, as well as polymers [3, 5]. The rapid increase of computational power as well as the development of highly efficient algorithms [6, 7] has culminated in the wide usage of the method which, as a result, has become greatly important in the field of materials science. According to the MD simulation method, the simulated system is represented by a collection of interacting particles the trajectories of which are calculated through the numerical solution of Newton's equations of motion, and the forces acting on them through the usage of interatomic potential functions.

The classical Newtonian equations of motion may be written as

$$\boldsymbol{F}_j(t) = m_j \frac{d^2\boldsymbol{r}_j}{dt^2} = -m_j \frac{\partial U_{tot}(\boldsymbol{r})}{\partial \boldsymbol{r}_j} \tag{2.1}$$

where $\boldsymbol{F}_j(t)$ is the force acting on the j^{th} particle at time t, and m_j and $\boldsymbol{r}_j$ are the mass and position of the particle. The acting force $\boldsymbol{F}_j(t)$ is also equal to the gradient of the potential function U_{tot}. In order to calculate the trajectory of a large number of particles, such as the one employed in the present study, Eq. 2.1 should be numerically integrated. The Verlet algorithm is the most frequently used numerical method employed for this purpose [8]. In this thesis we used a variant of the Verlet method, called velocity Verlet, which consists of three steps. First, the coordinates $\boldsymbol{r}_\mathrm{i}$ are calculated at the next time step $t + \delta t$, using Eq. 2.2.

$$\boldsymbol{r}_j(t+\delta t) = \boldsymbol{r}_j(t) + \delta t\, \mathbf{v}_j(t) + \frac{\delta t^2}{2m_j}\boldsymbol{F}_j(t) \tag{2.2}$$

Next the force $\boldsymbol{F}_j(t+\delta t)$ is derived from the gradient of the interaction potential $U_{tot}[\boldsymbol{r}(t+\delta t)]$, as depicted in Eq. 2.1, and finally the velocity $\mathbf{v}_j(t+\delta t)$ is calculated using Eq. 2.3.

$$\mathbf{v}_j(t+\delta t) = \mathbf{v}_j(t) + \frac{\delta t}{2m_j}\left[\boldsymbol{F}_j(t) + \boldsymbol{F}_j(t+\delta t)\right] \tag{2.3}$$

The main ingredient of an MD simulation is the potential function U_{tot} that is used to model the interactions among the constituents of the system. If both non-bonded and covalently bonded interactions are required for the simulation of the chosen system, the chosen potential function may consist of two corresponding parts, as depicted in Eq. 2.4.

$$U_{tot}(\boldsymbol{r}) = U_{nb}(\boldsymbol{r}) + U_b(\boldsymbol{r}) \tag{2.4}$$

The simplest choice for the non-bonded interaction potential U_{nb} would be a summation of pairwise interactions, as depicted in Eq. 2.5.

$$U_{nb}(\boldsymbol{r}) = \sum_j \sum_{k>j} V\left(\left|\boldsymbol{r}_j - \boldsymbol{r}_k\right|\right) \tag{2.5}$$

In this study we used the Lennard-Jones (LJ) 12/6 pair potential function for the modeling of the non-bonded interactions, which is the most commonly applied choice in MD simulations of polymeric systems:

$$V_{LJ}\left(r_{jk}\right) = 4\varepsilon_{jk}\left[\left(\frac{\sigma_{jk}}{r_{jk}}\right)^{12} - \left(\frac{\sigma_{jk}}{r_{jk}}\right)^{6}\right]\ ;\ r_{jk} < r_{cut} \tag{2.6}$$

The term $r_{jk} = \left|\boldsymbol{r}_j - \boldsymbol{r}_k\right|$ is the distance among the interacting particles j and k, ε_{jk} is the minimum interaction energy of the two particles, and σ_{jk} is the characteristic size of the particles, for which $V_{LJ}\left(\sigma_{jk}\right) = 0$. As depicted in Eq. 2.6, the LJ potential function is characterized by a strong repulsive part ($\propto r^{-12}$) and a weak attractive part ($\propto r^{-6}$). Commonly, the LJ potential function is truncated at a specified distance r_{cut} so as to avoid a prohibitively long duration of the simulation. The truncation, though, introduces a discontinuity, which can be remedied by shifting the potential function to higher values so that it will become equal to zero at the truncation point.

For the modelling of covalent bonds, a combination of the attractive Finite Extensible Non-Linear Elastic (FENE) potential and the LJ potential function was used, as depicted in Eq. 2.7 [9].

$$U_b(r) = -0.5k_{FENE}r_{max}^2 \ln\left[1 - \left(\frac{r}{r_{max}}\right)^2\right] + 4\varepsilon\left[\left(\frac{\sigma}{r}\right)^{12} - \left(\frac{\sigma}{r}\right)^{6}\right] + \varepsilon \tag{2.7}$$

Besides the LJ parameters, which have already been defined, the bonded potential function used in this study consisted of the parameters k_{FENE} and $r_{\max}$, which represented, respectively, the stiffness and the maximum elongation of the bond. The FENE bond has the form of a simple harmonic potential for small extensions, and limits the spring extensibility to $r_{\max}$. The superposition of the FENE and LJ potentials, under specific parameter values, yields an anharmonic spring interaction between the connected particles (Fig. 2.1).

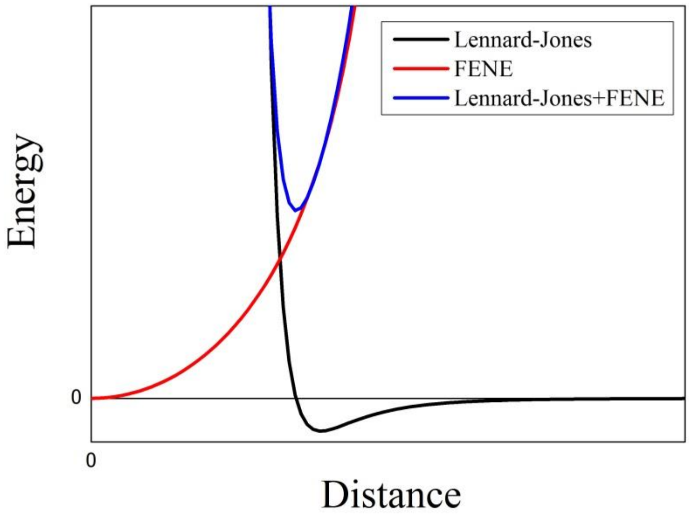

Figure 2.1: Illustration of the potential functions that were used during the simulations so as to model the interactions among the constituents of the systems.

2.1.1 Chosen statistical ensembles

A concept of great importance in the MD simulation method is the concept of the “thermodynamic ensemble” which is drawn from the field of statistical mechanics [10]. The latter sprang from the realization that the macroscopic properties of a system do not depend strongly on the motion of each individual particle but rather on the average motion of all the particles in the system. An ensemble refers to a collection of systems that have the same macroscopic but different microscopic properties, and the method to calculate the required macroscopic properties is through averaging over an ensemble of such systems. The ensembles that are relevant to this study are the microcanonical (NVE) ensemble in which the total energy and the number of particles in the system are each fixed to specific values, the canonical (NVT) ensemble, in which the temperature and the number of particles is fixed, and the isothermal–isobaric (NPT) ensemble, in which the temperature, the pressure and the number of particles are fixed. In an MD simulation the temperature and the pressure can be controlled by the application of a thermostat and a barostat. In this study, the Berendsen and Nose-Hoover thermostats and barostats were used. The Berendsen thermostat and barostat control the temperature and the pressure of the system by rescaling the velocities and the volume of the simulated system at each integration timestep. The Nose-Hoover thermostat and barostat control the temperature and the pressure of the system by adding extra terms in the equations of motion. The extra term introduced by the thermostat acts as a thermal reservoir, whereas the one added by the barostat controls the volume of the system [11-14]. The equations for the additional degrees of freedom are integrated along with Newton’s equations of motion, and as a result the system’s temperature and pressure fluctuates around the specified value, thus yielding the required ensemble.

2.2 Simulated polymer models

All the results that are presented in this study were obtained from coarse-grained (CG) MD simulations so as to overcome the requirement of knowing exhaustively the interaction potentials among the atoms of the simulated systems as well as the corresponding computational power that is stipulated by the utilization of such precise interatomic potentials. The use of CG models (Fig. 2.2), in place of atomistic ones, is justified by the nature of polymeric materials: polymers exhibit a clear time and length scaling of their static [**15**] and dynamic properties [**16**], while polymers with very different structure react universally to modifications in temperature [**17**]. Consequently, chemical details were ignored, and the polymer was represented by bead-spring chains [**18**], in which the chains were reduced to strings of beads, with each bead representing a small number of monomer units. The beads along a polymer chain were connected by a quasiharmonic potential (which herein was the FENE potential), and the repulsive part of the LJ potential was used to reproduce the excluded volume among the monomer beads (Eq. 2.7).

The scope of the simulations herein was to investigate the mechanical properties of filled elastomers. To this aim two different models have been simulated, with each of them representing a different scale of a generalized polymer filled with nanoparticles (Fig. 1.3). Chapters 3 and 4 present results that were obtained from simulations of polymer films capped in between two solid walls (Fig. 2.3), and Chapters 5 and 6 from simulations of systems composed by a polymer matrix and a number of nanoparticles, henceforth denoted as the particulate model (Fig. 2.5).

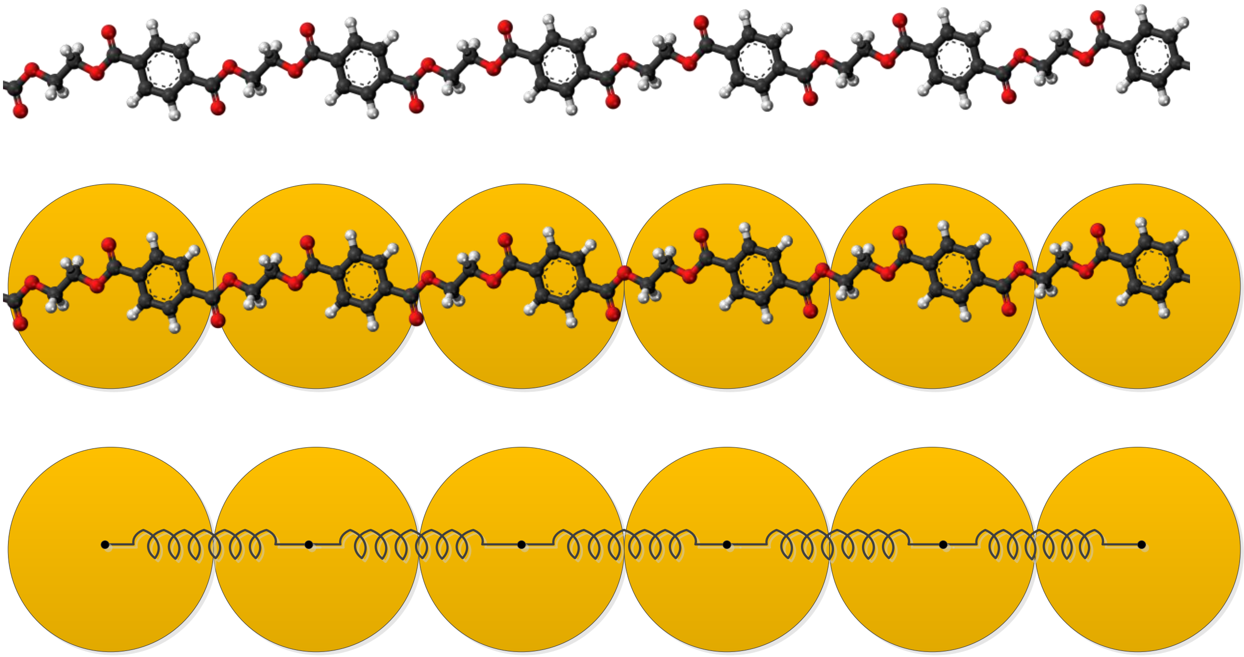

Figure 2.2: Schematic illustration of a coarse-grained procedure. The repetitive atomistic portions of the molecule are coarse-grained into larger beads which are connected by springs.

The film model was used so as to probe the structural and dynamical properties of the polymer matrix when it is confined between two nanoparticles whose size is orders of magnitude larger than the size of the polymer chains, while disregarding additional complexities arising from the presence of the filler network (such as its structure as well the size of the nanoparticles). The particulate model was studied so as to draw parallels among simulational and experimental results in regards to the reinforcement and the Payne effect, since its parameters are the same as those of the experimental protocols that are commonly used to study the mechanical properties of polymer nanocomposites, such as the volume fraction of fillers and the radius of the nanoparticles.

2.2.1 Film model

Concerning the film model (Fig. 2.3), each wall may be assumed to represent the surface of a nanoparticle, which, at the nanometer scale of the simulations, may be considered as flat. Since a larger volume fraction of fillers, or a smaller particle size, generally results in a shorter distance between neighboring nanoparticles, the effect of different filler volume fractions, or different particle sizes, at the nanometer scale of the film model has been studied by simulating three films of different thickness (henceforth referred to as thick, thin, and ultrathin film). The polymer chains had different compositions — *i.e.*, they were composed of two different types of monomer beads with different size — and this choice was made so as to mimic as faithfully as possible the different components of the random copolymers most commonly used in industrial applications of filled elastomers, *i.e.*, styrene-butadiene (SBR), which is mainly used in the manufacturing of car tires, and the nitrile-butadiene (NBR) rubber, which is mostly used in sealing applications [**19**].

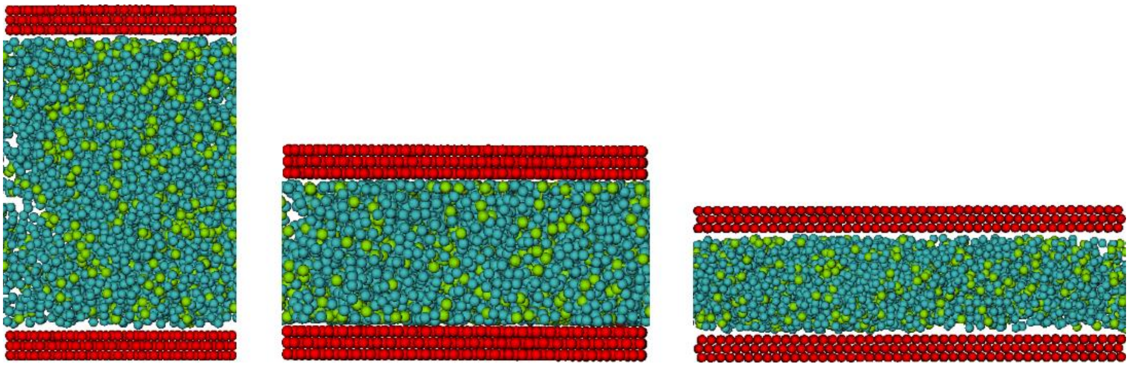

Figure 2.3: Typical snapshots of the simulated trajectory of the film model. The simulated films consisted of polymer chains confined between two solid walls (crystalline or rough). Three different values of the film thickness were used in the simulations herein. For thinner films larger lateral dimensions were used so as to retain the same statistical accuracy of the simulations in all the three different films.

We used the film model to study the effect of the film thickness and of the number of crosslink bonds among the monomers on the structural and dynamical properties of the confined polymer. Furthermore, simulations of films with different wall structure were also performed, so as to study the effects of the surface roughness on the structural, dynamical, and mechanical properties of the confined polymer. Three types of walls were used, which had a crystalline, rough, and amorphous structure, as illustrated in Fig. 2.4.

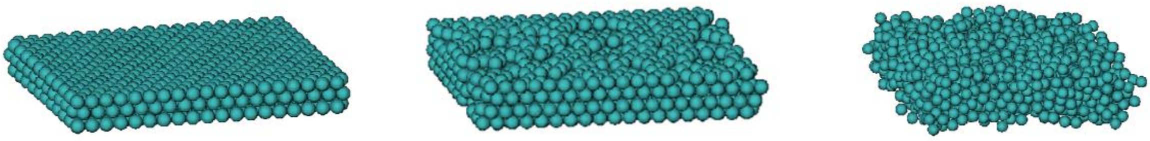

Figure 2.4: Illustration of the three types of walls that were used in this study. From left to right: crystalline, rough, and amorphous walls.

2.2.1 Particulate model

Concerning the particulate model (Fig. 2.5), each nanoparticle consisted of a specified number of beads which were randomly packed inside a sphere of a given radius. Due to the random packing of the filler beads, though, each nanoparticle was only approximately spherical. The polymer matrix was composed of homopolymer chains with the same length as those in the film model. The varying parameters in the simulations of the particulate model were the filler volume fraction and the radius of the nanoparticles.

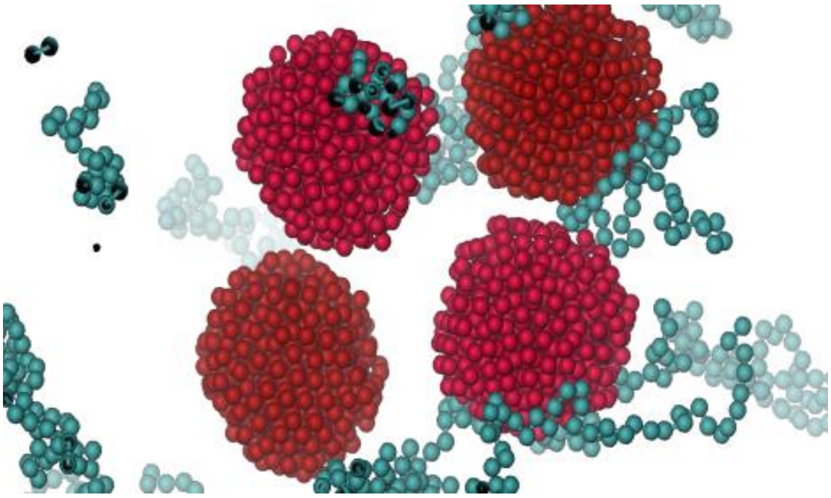

Figure 2.5: The particulate model of the nanocomposite. The filler beads are shown in red, and the polymer chains in green. Four nanoparticles, each consisting of 250 filler beads, of average

diameter about 10 times the diameter of the monomer beads are shown. For clarity, only a fraction of the polymer chains is shown.

2.3 System Creation and Equilibration

Unless stated otherwise, all quantities presented in this thesis are expressed in LJ units, *i.e.*, m, the mass of the smallest monomer bead in the polymer chains, was used as the unit of mass, ε, the minimum interaction energy between two monomer beads of mass m, was used as the unit of energy, σ, the diameter of a monomer bead of mass m, was used as the unit of length, and $\tau = \sigma\sqrt{m/\varepsilon}$ was the unit of time. The stiffness and maximum elongation of the FENE bonds were, then, set equal to $k_{\mathrm{FENE}} = 30\ \varepsilon/\sigma^2$ and $r_{\max} = 1.5\sigma$ respectively. Newton's equations of motion were integrated using the velocity-Verlet algorithm with a time step of $\delta t = 0.001\tau$.

2.3.1 Film model

The initial dimensions of the simulation box were calculated according to the chosen polymer mass density of $\rho_{\mathrm{film}} = 1.0\ m/\sigma^3$. We studied three films of different thickness, *i.e.*, at $T = 1.5\ \varepsilon/k_{\mathrm{B}}$, the thickness of the films were $D = 22.5\sigma$ (thick film), $D = 12.0\sigma$ (thin film), and $D = 5.1\sigma$ (ultrathin film), which correspond approximately to 6.2, 3.3, and 1.4 times the radius of gyration of the chains in the bulk, respectively. Films of different thickness had different lateral dimensions so that the simulation results would possess the same statistical accuracy by retaining at constant value the number of monomer beads regardless of the thickness of the film. Due to the crystallinity of the walls, the lateral dimensions of the box were only approximately equal, but in all cases the difference was kept smaller than 0.5σ.

The crosslinking procedure was based on the equilibrated uncured system. Crosslinks were created between monomers belonging to different chains, until the number of crosslinks had reached the desired value.

The initial configuration of the chains was created using a simple random walk algorithm. No overlap checking was done, so the initial structures displayed a finite number of overlaps. The first step was to refold all chains that were completely outside the periodic box. This was done in order to increase the number of beads whose distance was smaller than the specified crosslinking radius. The next step was to identify all candidate monomer pairs whose distance was smaller than the crosslinking cut-off radius. Crosslink bonds were then created between a randomly chosen candidate pair of monomers until the desired value of the crosslinking number density was reached. Using this method, crosslinked clusters were created with only a small fraction of free (non-crosslinked) chains. The spatial distribution of crosslinks along the direction perpendicular to the substrates was approximately uniform for all systems except for the ultra-thin film where a higher concentration of crosslinks was produced near the substrates rather than in the middle of the film.

For the equilibration runs, we used the default LAMMPS values for the applied thermostat and barostat [**7**]. During the equilibration, the two phases of the system (polymer and walls) displayed a tendency to move laterally. To prevent this, the center-of-mass linear velocity of the wall and polymer phases were set individually equal to zero, at each timestep. In order to minimize the wall-polymer interactions during the first stages of the equilibration, we set their interaction cut-off radius equal to the collision diameter between a wall- and monomer-bead (the distance for which their interaction energy was zero). In this way, monomer- and wall-beads repelled each other only when they collided.

To diminish the initial overlaps among the monomers, a short MD run was performed, for about 100-500τ in the microcanonical (NVE) ensemble while a limit was imposed on the maximum distance a bead can move in one timestep. After the pressure had stabilized, the substrate and monomer beads were assigned random velocities drawn from a Gaussian distribution. The velocities were set such that each subsystem had an initial high temperature of 1.5 ε/k_B so as to speed up the equilibration of the system.

Next, we performed constant density-temperature (NVT) simulations using the Berendsen thermostat, initially with repulsive wall-polymer interactions for about 30,000τ, depending on the film thickness, and afterwards using the full LJ potential (Eq. 2.6) for another 30,000τ. The combination of a single thermostat with repulsive wall-polymer interactions resulted in a considerable amount of heat transfer taking place from the substrates to the polymer, while the average temperature of the whole system remained constant and equal to the target value. To overcome this problem, we used two separate thermostats for the walls and the polymer while the wall-polymer interactions were repulsive. During the final equilibration NPT stage, we allowed the system to relax in an unstressed state for about 30,000τ, using the Nose-Hoover thermostat and barostat, and setting the normal components of the external pressure tensor equal to $P_{ii} = 0\ \varepsilon/\sigma^3$, where $i = \{x, y, z\}$.

One of the simulation variables was the number of crosslink bonds of the polymer. The crosslinking procedure was based on the equilibrated uncured system, during which FENE bonds were being created between monomer beads that belonged to different chains until the system had reached the desired crosslinking number density

$$\rho_{\mathrm{cl}} = \frac{\text{total number of crosslinks}}{\text{number of chains}} \tag{2.8}$$

The equilibration procedure of the crosslinked systems involved only the last NPT stage. All systems (as regards both to the film and to the particulate models) were assumed to be fully equilibrated once the autocorrelation function of the end-to-end vectors of the polymer chains

$$\varphi_{\mathrm{ee}}(t) = \frac{\langle\, \boldsymbol{R}_{\mathrm{ee}}(t_0)\ \cdot \boldsymbol{R}_{\mathrm{ee}}(t_0 + t)\, \rangle - \langle \boldsymbol{R}_{\mathrm{ee}} \rangle^2}{\langle \boldsymbol{R}_{\mathrm{ee}}^2 \rangle - \langle \boldsymbol{R}_{\mathrm{ee}} \rangle^2} \tag{2.9}$$

had decayed to zero [**20**], where $\boldsymbol{R}_{\mathrm{ee}}$ is the end-to-end vector of a chain. In practice, we allowed each system to equilibrate for a longer time than the relaxation time of φ_{ee}, so as to ensure that a thoroughly equilibrated configuration was attained.

2.3.2 Particulate model

To create the particulate systems, the box containing the equilibrated pure polymer was expanded so that the density would be low enough in order for the nanoparticles not to overlap with the polymer chains. Each nanoparticle consisted of a specified number of beads, which were placed randomly inside a sphere of predefined radius. Three different filler volume fractions were employed: 9%, 16.7%, and 28.5%, and the average filler particle radius extended from 3.25 to 6.5σ (with σ denoting the diameter of a monomer bead). We allowed the systems to equilibrate under NPT conditions. During the equilibration simulations we used the values recommended in the LAMMPS manual for the thermostat and barostat parameters, *i.e.*, the temperature and the pressure were allowed to relax to the specified average value over a time interval of 0.5τ and 5.0τ, respectively [**7**].

2.4 Calculated Properties

2.4.1 Structural Properties

In scattering experiments, the structure of a material at intermediate and large length-scales can be characterized by the static structure factor $S(\boldsymbol{q})$. From the static structure factor we can derive the radial distribution function $G(r)$, which characterizes the local structure of the material, and expresses the probability of the distance $r = |\boldsymbol{r}| = |\boldsymbol{r}_{jk}| = |\boldsymbol{r}_k - \boldsymbol{r}_j|$ between two particles of the system. It is commonly normalized by the average density, so as to converge to unity at very long distances. Values larger than unity indicate that the probability of finding a neighbouring particle at that distance is larger than what it would be if the particles were distributed randomly.

$$G_{ab}(r) = \frac{N}{\rho N_a N_b} \sum_{j=1}^{N_a} \sum_{k=1}^{N_b} \langle \, \delta\left(r - r_{jk}\right) \rangle \tag{2.10}$$

The term N represents the total number of particles in the system, N_a is the number of particles of type a, and ρ is the density of the system. Experimentally the radial distribution function of small colloidal systems can be measured by confocal microscopy experiments.

The static structure factor is derived from the Fourier transform of the radial distribution function, and it is the quantity that is actually measured in scattering experiments.

$$S_{ab}(\boldsymbol{q}) = \frac{f_{ab}}{N} \sum_{j=1}^{N_a} \sum_{k=1}^{N_b} \langle \, \exp\left(-i\boldsymbol{q} \cdot \boldsymbol{r}_{jk}\right) \rangle \tag{2.11}$$

In Eq. 2.11 $f_{ab} = 1$ for $a = b$ and $f_{ab} = 1/2$ for $a \neq b$. The static structure factor is measured in neutron and X-ray scattering experiments, since it is proportional to the scattering intensity of the “particles” that have been scattered by a wave-vector $\boldsymbol{q} = \boldsymbol{q}_{inital} - \boldsymbol{q}_{final}$.

2.4.2 Glass-Transition Temperature

If a crystal-forming fluid is cooled at its melting temperature, it will become solid. However, glass-forming liquids do not undergo the transition from liquid to crystalline solid when they are cooled further below their melting temperature. Instead of crystallizing, they become supercooled, retaining their liquidity, until they become glassy at the glass-transition temperature.

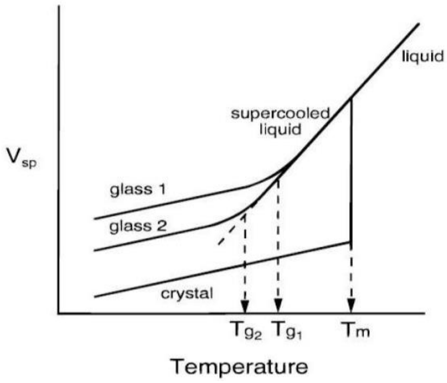

Figure 2.6: Volume as a function of temperature during a cooling simulation under constant pressure.

In general, while the temperature is decreased, the specific volume[1] of a liquid also decreases (Fig. 2.6). For a glass-forming liquid, as the temperature is decreased towards the glass-transition temperature, $T_g < T < T_m$, the specific volume V_{sp} decreases at a rate which is typical for a liquid. As a result, particle movement slows down, thus causing an increase in the viscosity, as well as in the relaxation time of the particles. If the cooling rate is high enough, the material falls out of equilibrium and the volume-temperature dependence deviates from the expected value. The temperature where this deviation occurs is referred to as the glass-transition temperature, T_g.

It follows from the above that the disordered structure of liquids and glasses is not noticeably different. Hence, at the glass-transition temperature there is no large structural change that may be used to predict the large difference in viscosity between a liquid and a glass. Still, liquids and glasses differ significantly in their dynamical response. A widely accepted explanation for the dramatic decrease in the dynamical response of glass forming materials is the Adam-Gibbs hypothesis [**21-23**]. It suggests that when the temperature decreases, the density increases but not homogeneously;

---

[1] Specific volume: volume per unit of mass.

hence the particles' motion becomes co-operative — *i.e.*, particles rearrange in groups rather than individually. The increase in the relaxation time is, then, a direct consequence of the growing rearranging regions of cooperative motion. Overall, the different dynamic response of each region causes heterogeneous dynamics in the whole system. This dynamic heterogeneity is connected to the so-called dynamic fragility of glass-forming materials [**24**]. The narrower is the glass-transition temperature range, the more dynamically fragile the material is considered to be (*e.g.*, at Fig.2.6, glass is more dynamically fragile than glass 2).

2.4.3 Dynamical Properties

To study the relaxation of single 'particle' motions, we calculated the incoherent intermediate scattering function

$$S_{inc}(\boldsymbol{q},t) = \frac{1}{N}\left\langle \sum_{j=1}^{N} \exp\{-i\boldsymbol{q} \cdot [\boldsymbol{r}_j(t) - \boldsymbol{r}_j(0)]\} \right\rangle \tag{2.12}$$

which is measured in neutron-scattering experiments so as to probe the various relaxation modes in macromolecular systems [**25**]. In Eq. 2.12, the term N denotes the total number of monomers in the system (which, in our simulations, were individual bead segments), $\boldsymbol{r}_j(t)$ is the position of the j^{th} monomer at time t, and $\boldsymbol{q}$ is the scattering vector that defines the length scale $l_q = 2\pi/q$ with the dominant contributions to the relaxation process. Thus, relaxation times on different length scales can be calculated by varying the magnitude q of the scattering vector [**26**]. $S_{\text{inc}}(q,t)$ for a given magnitude q was computed by calculating the average value of three wave vectors $\boldsymbol{q}$ with the same magnitude but different directions along the primary Cartesian axes. In Chapter 4 we present our simulation results of the incoherent relaxation in the region between $q = 7.0\ \sigma^{-1}$, which corresponded approximately to the first peak in the overall static structure factor [**27**], and $q = 1.0\ \sigma^{-1}$, which corresponded to a length scale between the end-to-end distance and the gyration radius of the chains.

2.4.4 Mechanical Properties

In order to extract the mechanical properties of the simulated composites, and study their non-linear response (in particular, the Payne effect) we performed dynamic oscillatory shear simulations, by subjecting the systems to a sinusoidal deformation and measuring the resulting mechanical response as a function of time. Oscillatory shear tests can be divided into two regimes. One regime induces a linear viscoelastic response (small amplitude oscillatory shear, SAOS), whereas in the other regime the material response becomes non-linear (large amplitude oscillatory shear, LAOS). LAOS tests are useful for a broad class of complex fluids and soft matter because strain amplitude and frequency can be varied independently allowing a broad spectrum of conditions to be attained [**28**]. Our model composites were specifically subjected to LAOS simulations so that we could extract their non-linear response and thus correlate the Payne effect with the volume fraction and the radius of the filler nanoparticles, as well as with the microstructure and the microscopic dynamics of the simulated systems. As the strain amplitude is increased under a fixed frequency, a transition between the linear and nonlinear regimes can appear. Fig. 2.7 illustrates the elastic and viscous moduli obtained from an oscillatory strain-sweep test in which the frequency was fixed and the applied strain amplitude was varied. In Fig. 2.7 the viscoelastic response is quantified by two properties, namely the elastic (storage) modulus *G*’ and the viscous (loss) modulus *G*’’.

In the linear regime the strain amplitude is sufficiently small so that both viscoelastic moduli are independent of it, and the oscillatory stress response is sinusoidal. The strain amplitudes used in linear oscillatory shear tests are generally very small, often on the order of $\gamma_{\max} \approx 10^{-2}$ to 10^{-1} for homopolymer melts, or even smaller ($\gamma_{\max} < 10^{-2}$) for many dispersed systems [**29**].

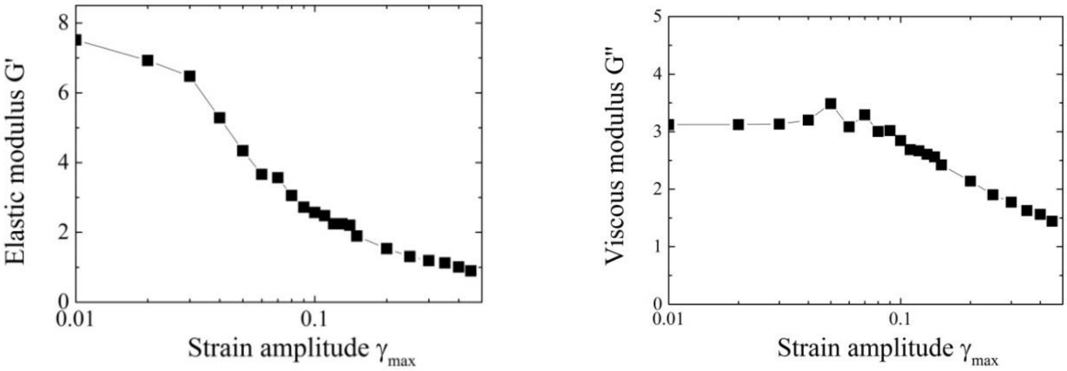

Figure 2.7: Schematic illustration of the stress-strain behavior of an elastomer-based nanocomposite, during a strain sweep test at a fixed frequency. A specific behavior of the elastic and the viscous modulus is shown, the Payne effect, which is distinguished by a

high *G*' at low strain amplitudes with a subsequent drop, and by the presence of a maximum in the *G*''. The depicted data were retrieved from one of our simulations.

In the nonlinear regime, though, the moduli are a function of the strain amplitude, and the resulting periodic stress waveform becomes distorted, and deviates from the sinusoidal waveform. At such large strain values — when the stress is no longer perfectly sinusoidal — the storage and the loss modulus lose their precise physical meaning, their calculation is not unique, and different methods result in different values of the moduli [**29]**. The different methods of calculating the moduli in the non-linear regime of the stress response, as well as the precise deformation protocol used in the simulations, are described with details in Chapter 6.

References

[1] Alder B. J., Wainwright T. E., *J. Chem. Phys.* **1957**, *27*, 1208–1209.

[2] Alder B. J., Wainwright T. E., *J. Chem. Phys.* **1959**, *31*, 459–466.

[3] Barrat J.L., Klein M. L., *Annu. Rev. Phys. Chem*. **1991**, *42*, 23–53.

[4] Baschnagel J., Varnik F. *J., Phys. Condens. Matter* **2005**, *17*, R851–R953.

[5] Redondo A., LeSar R., *Annu. Rev. Mater Res.* **2004**, *34*, 279–314.

[6] van der Spoel D., Lindahl E., Hess B., van Buuren A. R., Apol E., Meulenhoff P. J., Tieleman D. P., Sijbers A. L. T. M., Feenstra K. A., van Drunen R., Berendsen H. J. C., *Gromacs User Manual version 4.5*, www.gromacs.org, 2010.

[7] Plimpton S., *J. Comput. Phys.* **1995**, *117*, 1–19.

[8] Verlet L., *Phys. Rev.* **1967**, *159*, 98–103.

[9] Kremer K., Grest G.S. *J. Chem. Phys.* **1990**, *92*, 5057.

[10] Gibbs J.W., *Elementary Principles in Statistical Mechanics*, Charles Scribner's Sons: New York, 1902.

[11] Parrinello M., Rahman A., *J. Appl. Phys.* **1981**, *52*, 7182.

[12] Martyna G.J., Tobias D.J., Klein M.L., *J. Chem. Phys.* **1994**, *101*, 4177.

[13] Dullweber A., Leimkuhler B., McLachlan R., *J. Chem. Phys.* **1997**, *107*, 5840.

[14] Shinoda W., Shiga M., Mikami M., *Phys. Rev. B* **2004**, *69*, 134103.

[15] de Gennes P. G., *Scaling concepts in polymer physics*. New York: Cornell University Press, 1979.

[16] Doi M., Edwards S. F., *The theory of polymer dynamics*, Clarendon Press: Oxford, 1989.

[17] Bulacu M., Van der Giessen E., *J Chem Phys* **2005**, *123*(11), 114901.

[18] Bishop M., Kalos M. H., Frisch, H. L., *J Chem Phys* **1979**, *70*(3), 1299–1304.

[19] Mark J. E., Erman B., Eirich F. R., *Science and Technology of Rubber*, Elsevier: Amsterdam 2006.

[20] Mulder T., *Equilibration and deformation of glass-forming polymers : molecular simulation via connectivity-altering Monte Carlo and scale-jumping methods*, PhD Thesis, Technische Universiteit Eindhoven: Eindhoven, 2008.

[21] Debenedetti P. G,. *Metastable liquids: concepts and principles*. Princeton University Press: Princeton, 1996.

[22] Adam G., Gibbs J. H. J., *Chem. Phys*. **1965**, *43*, 139–146.

[23] Binder K., Kob W., *Glassy Materials and Disordered Solids: An Introduction to Their Statistical Mechanics* (Revised Edition). World Scientific, 2011.

[24] Evans C. M., Deng, H. Jager W. F., Torkelson J. M., *Macromolecules* **2013**, 46, 6091.

[25] Bennemann C., Baschnagel J., Paul W., *Eur. Phys. J. B* **1999**, *10*, 323-334.

[26] Tsoloua G., Harmandaris V. A., Mavrantzas V. G., *J. Non-Newton. Fluid Mech*. **2008**, *152*, 184-194.

[27] Davris T., Lyulin A. V., *Polym. Compos*. **2015**, *36*, 979–1175.

[28] Hyun K., Nam J. G., Wilhelm M., Ahn K. H., Lee S. *J., Rheol Acta* **2006**, *45*, 239–249.

[29] Klein O. C., Spiess H. W., Calin A., Balan C., Wilhelm M., *Macromolecules* **2007**, *40*, 4250–4259.

Chapter 3

Molecular-dynamics simulations of crosslinked polymer films: equilibrium structure and glass-transition temperature

Abstract

In this chapter we present our results from constant temperature-pressure (NPT) molecular dynamics (MD) simulations of a bead-spring copolymer model, in which the polymer was confined between two crystalline walls. Our goal was to study the combined effect of the polymer crosslink density and of the degree of confinement on the glass-transition temperature and the equilibrium structure of the films. The simulations showed that, in the direction perpendicular to the walls, the polymer chains were ordered in layers of increasing density towards the walls for all values of the crosslink density and degree of confinement. On the other hand, in the direction parallel to the walls, the confined polymer displayed an amorphous structure similar to that of the bulk polymer. Lastly, the glass-transition temperature increased with both confinement and crosslink density, with the former having had a large effect in comparison to the latter. *

∗The contents of this chapter have been published in: *Polym. Composite.*, **2015**, *36*, 1012–1019.

3.1 Introduction

Filled elastomers, realized by mixing pure rubber with filler particles of sub-micron or nanometer size, are a class of materials of high technological importance, being used in car tires, sealing solutions for bearing applications, and other types of plastic and rubber. The addition of particles to the polymer matrix results in a composite material that exhibits much higher stiffness and extreme resistance to both fracture and abrasion while remaining highly elastic (the so-called reinforcement of rubber) [**1**]. At a fundamental level, rubber-reinforcement is a complex function of the interfacial interactions, the interfacial area, and the distribution of inter-filler distances [**1,2**]. The latter two factors depend on the nano-filler dispersion, making it difficult to develop a fundamental understanding of their effects on the properties of the nanocomposite.

Various attempts to study the influence of the degree of confinement on the mechanical properties of polymer nanocomposites have deployed a film polymer model, where the authors have tried to establish a quantitative equivalence between the thermomechanical properties of the two systems [**2-5**]. The main argument is that the properties of both systems are strongly influenced by polymer-surface interactions and by confinement effects, and that a connection exists in cases where the average diameter of the filler particles is orders of magnitude larger than the size of the chains.

Bansal et al. [**2**] have shown that the experimental thermo-mechanical properties of highly filled (40 wt%) polymer nanocomposites are quantitatively equivalent to the well documented case of planar polymer films. They quantified this equivalence by drawing a direct analogy between film thickness and inter-particle spacing. They showed that the changes in the glass-transition temperature with decreasing inter-particle spacing for two filler surfaces are quantitatively equivalent to the corresponding thin-film data.

Similar experiments with materials of a lower filler concentration (less than 1.0 wt%) showed only a qualitative equivalence between nanocomposites and thin films [**2,5**]. Kropka and coworkers examined the changes in the glass-transition temperature of polymer nanocomposites and their equivalence to those of thin films, in terms of a percolation model. While the qualitative behavior of both systems was similar, clear quantitative differences were discerned. However, a phenomenological model was suggested that could use results from thin film simulations to quantitatively predict the properties of polymer nanocomposites.

Other authors have used the film model as a representative system in order to study structural, dynamical, and mechanical properties of polymer nanocomposites [**6-10**]. Batistakis and coworkers [**6,7**] studied the confinement-induced creation of glassy layers in capped polymer films, employing a model similar to ours. Here, we have extended these studies by modeling the structural changes which are induced by the combination of confinement effects and the crosslink density of the polymer.

A number of simulation data are already present in the literature concerning the effect of crosslinking on the structural, dynamical, and mechanical properties of polymer systems [**11-15**]. Liu et al [**11**] performed molecular dynamics (MD) simulations to study the effect of the crosslink density on the structural and dynamical properties of a bead-spring bulk homopolymer system. They observed that the radial distribution function of the monomer segments was not affected by the presence of the crosslink bonds. However, the glass-transition temperature displayed a positive linear variation with the crosslink density, whereas the self-diffusion coefficient displayed a stronger (exponential) negative dependence.

The glass transition in thin polymer films has also been widely examined experimentally. The reported results have shown disagreement among different laboratories and among different experimental methods as regards the T_g of polymer films in relation to that of the bulk. The generally accepted opinion is that the behavior of T_g in films depends on the polymer-wall interactions and, in addition, it is particularly affected when the thickness of the film becomes smaller than a specified length scale [**15**, **16**].

This chapter deals with how the structural properties and the glass-transition temperature of the polymer are influenced when the chains are crosslinked and confined between two solid walls. Besides identifying the transition using only a single number T_g, we have also determined the differences in thermal expansivities between the rubbery and glassy states.

3.2. Models and Methods

3.2.1 Model Description

We performed molecular-dynamics simulations of polymer chains confined between two crystalline walls using the LAMMPS software package [**17**]. We used a coarse-grained representation of a polymer film consisting of 100 linear copolymer chains with a fixed size of 50 monomer segments per chain [**18**]. Eighty percent of the monomers of each chain were of type A, and we denote the rest as type B monomers. We use the letter W to denote the wall segments, all of which were of the same type. Moreover, we compared the film data with results produced by simulations performed in the bulk polymer. Note also that we assume the polymer chains were non-entangled, because the microscopic topological constraints we identified, were short-lived and thus unable to sustain stress [**19**].

We placed the system in a three-dimensional periodic box. Each wall was composed of three lateral layers of equally sized non-bonded beads arranged in a hexagonal closed packed (HCP) regular lattice. They were periodically infinite along the lateral dimensions, and they confined the polymer along the perpendicular direction, as depicted in Fig. 3.1. When we chose the thickness of the walls, we made sure not to violate the minimum image criterion, also taking into account their periodic images along the perpendicular direction.

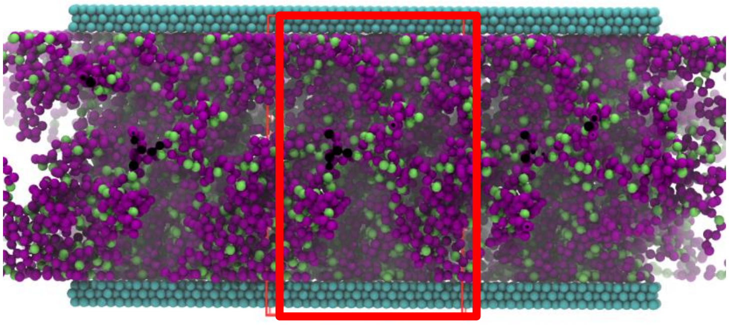

Figure 3.1: A snapshot of the simulated copolymer that is confined between two crystalline substrates. Different colors are used to represent different bead types. The red rectangle depicts the periodic simulation box. We created the illustration using the molecular visualization software VMD [**20**].

The non-bonded interactions were modelled using the Lennard-Jones (LJ) 12-6 potential, which included a switching function, $S_f(r)$, that ramped the energy and the force smoothly to zero between $r_{cut}^{in} = 3.25\sigma$ and $r_{cut}^{out} = 3.50\sigma$ [**21**].

$$U_{nb}(r) = 4\varepsilon\left[\left(\frac{\sigma}{r}\right)^{12} - \left(\frac{\sigma}{r}\right)^{6}\right] + S_{f(r)} \quad (r < r_{cut}^{out}) \tag{3.1}$$

The Lennard-Jones (LJ) units of measurements are used throughout the chapter, i.e. m is the unit of mass, ε is the unit of energy, σ is the unit of length and τ is the unit of time, where $\tau = \sigma\sqrt{m/\varepsilon}$. We have chosen the following values for the LJ parameters: $\sigma_{\mathrm{AA}} = \sigma$, $\varepsilon_{\mathrm{AA}} = \varepsilon$, $m_{\mathrm{A}} = m$, $\sigma_{\mathrm{BB}} = 1.2\sigma$, $m_{\mathrm{B}} = (\sigma_{\mathrm{B}})^3 m$, $\varepsilon_{\mathrm{BB}} = \varepsilon$, $\sigma_{\mathrm{WW}} = 0.85\sigma$, and $\varepsilon_{\mathrm{WW}} >> \varepsilon$. The LJ parameters between beads of different types were calculated according to the Lorentz-Berthelot rule, $\sigma_{ij} = (\sigma_{ii} + \sigma_{jj})/2$, but the energy parameters were fixed and predefined, *i.e.*, $\varepsilon_{\mathrm{AB}} = \varepsilon_{\mathrm{AW}} = \varepsilon_{\mathrm{BW}} = \varepsilon$. The interaction strength between the wall beads, $\varepsilon_{\mathrm{WW}}$, was chosen high enough so as to ensure that the crystallinity of the walls was never broken. The size of the wall beads, $\sigma_{\mathrm{WW},}$ was chosen smaller than the smallest monomer type so as to avoid the adsorption of monomers on the internal surface of the substrates, due to geometric constraints [**6**]. We did not account for electrostatic Coulomb interactions or for long-range energy corrections.

Covalently bonded beads interacted through a combination of an attractive Finite-Extensible-Nonlinear-Elastic (FENE) potential and a repulsive and truncated LJ 12-6 potential (Chapter 2, 2.7) [**22**]. The stiffness and the maximum elongation of the spring were set equal to $k_{\mathrm{FENE}} = 30\ \varepsilon/\sigma^2$ and $r_{\max} = 1.5\ \sigma$. The LJ parameters ε and σ had the same values with their non-bonded counterparts. This particular choice of bonded and non-bonded interactions has been shown to prevent chain crossing [**18**] and crystallization [**22-24**]. An additional consequence of this model is that chains do not become stiffer with decreasing temperature. Newton's equations of motion were integrated by the velocity Verlet algorithm, using a time step of $\delta t = 0.001\tau$.

3.2.2 System Preparation and Equilibration

The initial dimensions of the simulation box were calculated according to the chosen polymer mass density of $\rho_{film} = 1.0\ m/\sigma^3$. We studied three films of different thickness, *i.e.*, at $T = 1.5\ \varepsilon/k_{\mathrm{B}}$, the thickness of the films were $D = 22.5\sigma$ (thick film), $D = 12.0\sigma$ (thin film), and $D = 5.1\sigma$ (ultrathin film), which corresponded approximately to 6.2, 3.3, and 1.4 times the average radius of gyration of the chains in the bulk, respectively. Films of different thickness had different lateral dimensions, so that the mass density would be the same in all of them under constant number of monomer beads, so as to retain the same statistical quality in all our simulations. Due to the crystallinity of the walls, the lateral dimensions of the box were only approximately equal, but in all cases the difference was kept smaller than 0.5σ.

The initial configuration of the chains was created using a simple random walk algorithm. No overlap checking was conducted, and as a consequence, the initial structures displayed a finite number of overlaps. The crosslinking procedure was based on the equilibrated uncured systems. Crosslinks were created between monomers belonging to different chains until the system had reached the desired crosslinking number density (Chapter 2, Eq. 2.8). The first step was to refold all chains that were completely outside the periodic box. This was done in order to increase the number of beads whose distance was smaller than the specified crosslink radius. The next step was to identify all candidate monomer-pairs whose distance was smaller than the crosslink cut-off radius. Crosslink bonds were, then, created between a randomly chosen candidate pair of monomers, until the desired value of the crosslink number density was reached. Using this method, crosslinked clusters were created with only a small fraction of free (non-crosslinked) chains. The spatial distribution of crosslinks along the direction perpendicular to the walls was approximately uniform for all systems except for the ultra-thin film where a higher concentration of crosslinks was produced near the substrates rather than in the middle of the film.

For both equilibration and production runs, we used the default LAMMPS values for the applied thermostat and barostat [**17**]. During the equilibration, the two phases of the system (polymer and walls) displayed a tendency to move laterally. To prevent this, the center-of-mass linear velocity of the wall- and polymer-phases were set individually, at each timestep, equal to zero. In order to minimize the wall-polymer interactions during the first stages of the equilibration, we set their interaction cut-off radius equal to the collision diameter (the distance for which the interaction energy is zero) between a wall and a polymer bead. In this way, monomer- and wall-beads repelled each other only when they collided.

To diminish the initial overlaps among the monomers, a short MD run was performed, for about 100-500τ in the microcanonical (NVE) ensemble, while a limit was imposed on the maximum distance a bead could move in a single timestep. After the pressure had stabilized, the wall- and monomer-beads were assigned random velocities which were drawn from a Gaussian distribution. The velocities were set such that each subsystem had an initial high temperature of 1.5 ε/k_B, so as to accelerate the equilibration of the system.

Next, we performed constant density-temperature simulations, using the Berendsen thermostat, initially with repulsive adhesion interactions, for about 30,000τ (depending on the film thickness), and afterwards, using the full LJ potential (Eq. 1) for another 30,000τ. The combination of a single thermostat with repulsive adhesion interactions resulted in a considerable amount of heat transfer taking place from the walls to the polymer, while the average temperature of the whole system remained constant and equal to the target value. To overcome this problem, we used two separate thermostats for the walls and for the polymer, during the equilibration stages when the wall-polymer interactions were repulsive. During the final equilibration step, we allowed the system to relax in an unstressed state for about 30,000 τ, using the Nose-Hoover thermostat and barostat and by setting the normal components of the external pressure tensor equal to $P_{ii} = 0\ \varepsilon/\sigma^3$, where $i = \{x, y, z\}$.

The equilibration procedure of the crosslinked systems involved only the last NPT stage. All crosslink bonds were unbreakable. We regarded the systems as fully equilibrated after the autocorrelation function of the end-to-end vectors (Chapter 2, Eq. 2.9) had decayed to zero [**25**]. In practice, we allowed the systems to equilibrate for longer times than the relaxation time of φ_{ee}, to ensure a thoroughly equilibrated configuration.

3.3 Results

3.3.1 Effect of Cut-off Radius on the Density-Temperature Profile

We studied the effect of the LJ cut-off radius on the mass density - temperature profiles of the non-crosslinked systems [**21**]. We compared two different cut-off schemes: in the first case, the potential was abruptly truncated and shifted,

$$U_{(r)} = 4\varepsilon\left[\left(\frac{\sigma}{r}\right)^{12} - \left(\frac{\sigma}{r}\right)^{6}\right] - U_{(r_{cut})} \qquad (r < r_{cut}) \tag{3.2}$$

whereas in the second case, a switched truncation was used (Eq. 3.1). For the abrupt truncation (AT), we tested two different cut-off radii of 2.5σ and 3.5σ, and for the switched truncation (ST), we used an inner and outer cut-off radius of 2.25σ and 2.5σ, respectively.

The equilibration procedure consisted of two stages. First, we performed NVT simulations at constant temperature T = 1.5 ε/k_B and mass density ρ_m = 1.0 m/σ^3. Second, we performed NPT simulations in which the pressure component perpendicular to the walls was set equal to 1.0 ε/σ^3. We did not keep track of the lateral components of the pressure tensor. During the production stage of the simulations, we decreased the temperature step-wise, from 1.5 to 0.05 ε/k_B, with a cooling rate of 0.0003 $(\varepsilon/k_B)/\tau$. The results are presented in Fig. 3.2.

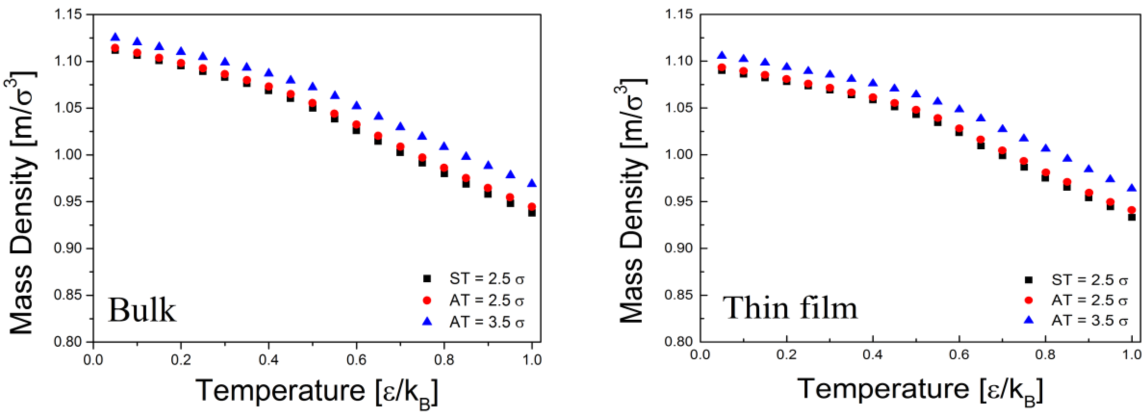

Figure 3.2: Effect of the cut-off radius on the polymer mass density (ρ_m) – temperature (T) profile for the bulk (a) and thin film (b). Using a larger cut-off radius results in a higher mass density.

Apparently, the cut-off scheme, i.e., AT vs. ST, did not have a noticable impact on the density-temperature profile. However, that was not the case with the magnitide of the cut-off radius: a larger cut-off radius results in a positive vertical shift of the density curve. Finally, we decided to use a ST potential with a cutoff distance of 3.5σ for the subsequent simulations. We decided not to use a longer cut-off distance, aiming to avoid additional computational costs, and because a larger cut-off radius could interfere with the minimum image criterion during the simulations of the ultrathin films.

3.3.2 Glass-Transition Temperature

We allowed the systems to relax at T = 0.8 ε/k_B and P = 0.0 ε/σ^3, until φ_{ee} had decayed to zero. We performed the simulations for the calculation of the glass-transition temperature in the NPT ensemble, lowering the temperature of the system by 0.2 ε/k_B per 10^2 τ in a step-wise fashion from 0.8 to 0.1 ε/k_B. This procedure resulted in a cooling rate of $0.2 \cdot 10^{-7}$ (ε/k_B)/τ. The glass-transition temperature was determined from the change in the slope of the polymer mass density with the temperature, above and below the transition region [**6**]. It is evident from Fig. 3.3, that the slope change within the transition region (i.e., the difference in the thermal expansivity below and above the T_g), was larger in the films than in the bulk polymer.

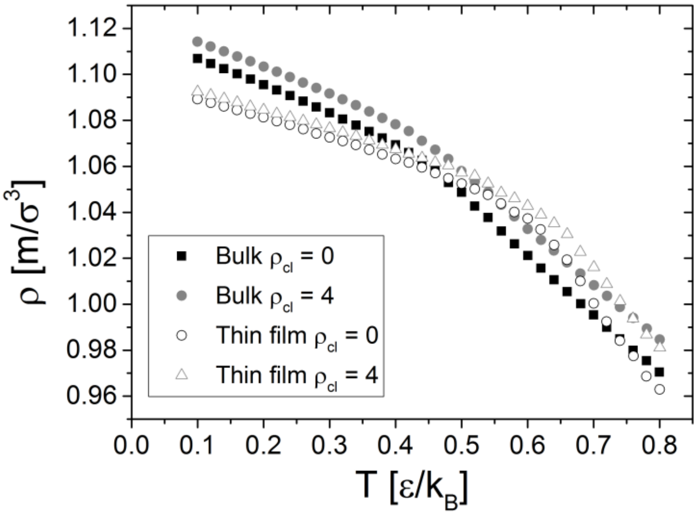

Figure 3.3: Density – temperature dependence for the bulk and the ultrathin film. Two different crosslinking densities (ρ_{cl}) are displayed. The average pressure was held constant and equal to zero for all systems.

This difference is also apparent in Fig 3.4, in which the thermal expansion coefficient is shown for temperatures above and below the glass-transition temperature. The thermal expansion coefficient (CTE) is defined as

$$\alpha_T = \frac{1}{\rho_0}\left(\frac{d\rho}{dT}\right)_P \tag{3.3}$$

where ρ_0 is the mass density of the polymer at $T = 0.8$ ε/k_B.

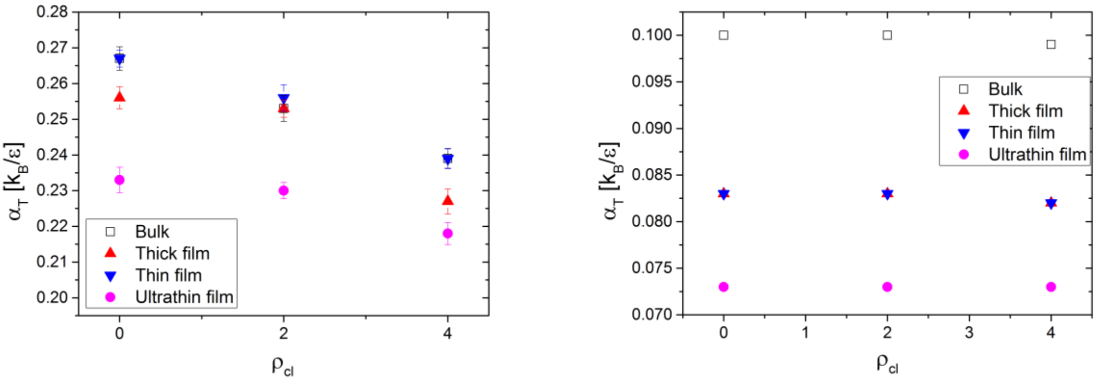

Figure 3.4: Thermal expansion coefficients as a function of the polymer crosslinking density (see Eq. 3.3). Left: Above the T_g (rubber). Right: Below the T_g (glass).

Fig. 3.4 shows that the CTE of the films in the rubbery state was weakly dependent on the degree of confinement for the two thickest films, whereas it was slightly smaller in the ultrathin film. This could indicate that the degree of confinement affected the CTE only when the average film thickness approached the bulk radius of gyration of the chains. In the glassy state, the CTE decreased when the polymer was confined and, while it was independent on the degree of confinement for the thick and thin films, it displayed a strong decrease in the ultrathin film where the film thickness was very close to the gyration radius of the chains in the bulk polymer.

Apparently, the crosslinks inhibited any volume expansion in response to any temperature increase, for $T > T_g$. We attribute this decrease in CTE to the decreased chain flexibility in systems with a higher number of crosslinks. As can be seen in Fig. 3.3, the calculated CTE above the T_g decreased with increasing crosslink density, whereas it remained approximately constant for temperatures lower than the T_g. The low values of CTE below the T_g were due to a higher polymer density, and due to the reduced molecular mobility which decreases the volumetric response of the material to temperature changes.

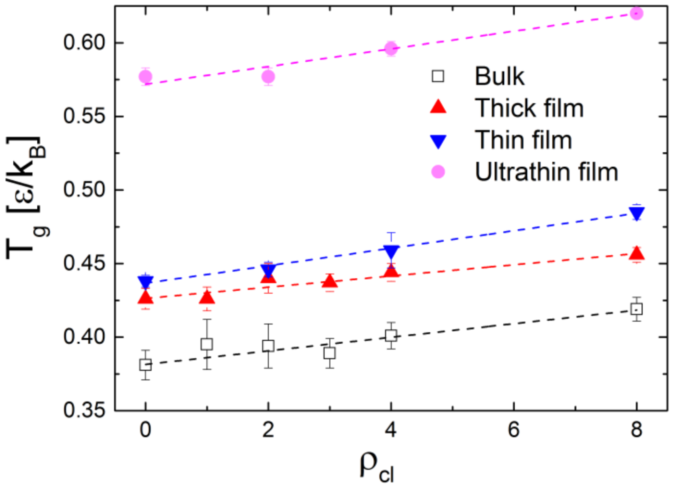

Figure 3.5: Glass-transition temperature as a function of crosslinking density and film thickness. The average pressure is constant and equal to zero for all systems.

The dependence of the glass-transition temperature on the crosslink density, and on the degree of confinement, is displayed in Fig. 3.5. It is evident that the T_g was only weakly affected by the crosslink density, increasing linearly with increasing ρ_{cl}, whereas it was strongly affected by the degree of confinement: a higher degree of confinement resulted in a higher glass-transition temperature.

3.3.3 Local Structure and Density

The spatial density profiles of the crosslinked and non-crosslinked systems in the direction perpendicular to the substrates were similar (Fig. 3.6), and therefore, we conclude that the adopted crosslinking method did not affect the conformation of the chains.

Confining the polymer between two crystalline walls created layers of different densities whose relative size was independent of the degree of confinement. The polymer density displayed a maximum value near the walls, and decreased towards the middle of the film, where it became equal to the density of the bulk polymer. This result is in agreement with similar simulation results found in the literature [**6**]. In addition, the density layers became increasingly more homogeneous as we increased the temperature (not shown).

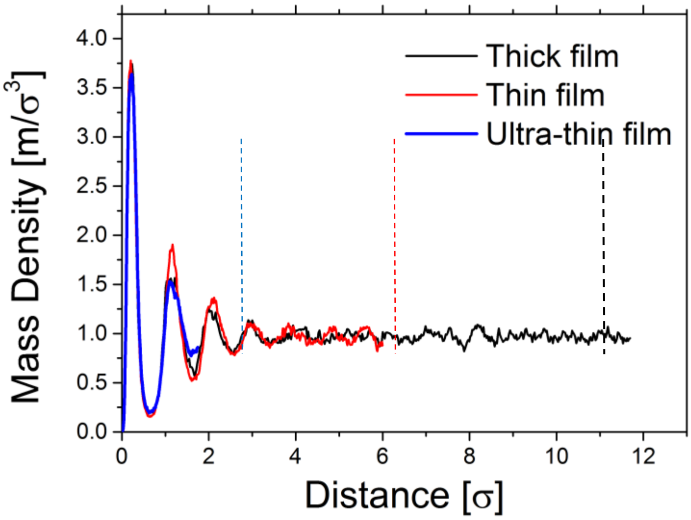

Figure 3.6: Spatial mass density profile of the monomer segments for the three films at T = 0.8 ε/k_B. In all films, the density oscillates around the bulk average value. Since the profiles are symmetric with respect to the middle of the film, only half of the film thickness is shown. The vertical dashed lines indicate the middle of each film along the direction perpendicular to the substrates.

Despite the strong structuration of the polymer in the direction perpendicular to the walls, neither the degree of confinement nor the crosslink density perturbed the lateral structure of the polymer [**11**]. As shown in Fig. 3.7, the overall static structure factor displayed a sequence of peaks whose amplitude rapidly decreases toward unity. This is an indication of the short-range order of the monomers, which is typically observed in amorphous materials.

The location of the first sharp diffraction peak was found approximately at q = 7.0 σ^{-1}. The overall static structure factor of the crosslinked systems displayed a local maximum at low magnitudes of the wavevector $\boldsymbol{q}$, which is indicative of the existence of large-scale correlations (this correlation length is probably associated with the average distance between the crosslink junctions).

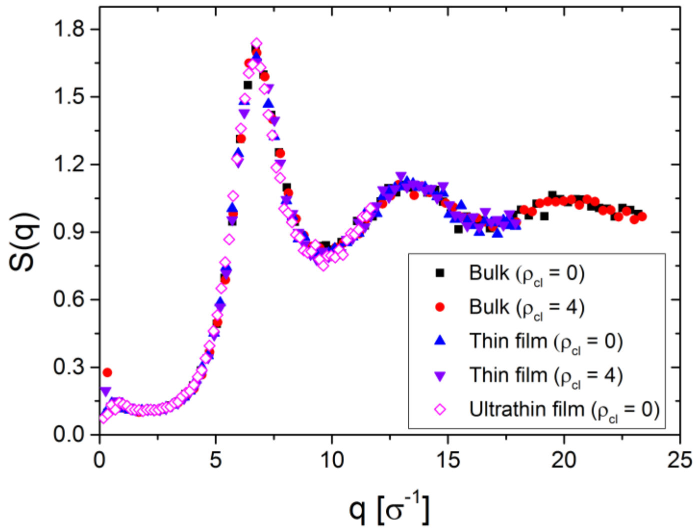

Figure 3.7: Overall static structure factor for various systems, at $T = 1.2$ ε/k$_B$. For the film data, we have used wavevectors **q** parallel to the substrates.

In Fig. 3.8, we compare the form factor for systems with different crosslinking density and degree of confinement:

$$S^{sc}(q) = \frac{1}{N_c}\left\langle \sum_{j=1}^{N_{mc}} \sum_{\mathrm{k}=1}^{N_{mc}} \exp\{i\boldsymbol{q}\cdot(\boldsymbol{r}_j^c - \boldsymbol{r}_{\mathrm{k}}^c)\} \right\rangle \tag{3.4}$$

where N_{c} is the number of polymer chains, N_{mc} is the number of monomers per chain, and $\boldsymbol{r}_j^c$ is the position of the j^{th} monomer of the c^{th} chain. The solid line within the figure represents the Debye formula for Gaussian coils [**26**]:

$$S^{sc}_{\mathrm{Debye}}(t) = \frac{2\,N_{mc}}{(qR_{\mathrm{g}})^4}\left\{\exp\left[-(qR_{\mathrm{g}})^2\right] + (qR_{\mathrm{g}})^2 - 1\right\} \tag{3.5}$$

where the radius of gyration of the chains, R_{g}, was calculated from the simulations. It is evident that the form factor in all of the systems agreed well with the Debye function, which implies a Gaussian conformation of the chains on all length scales.

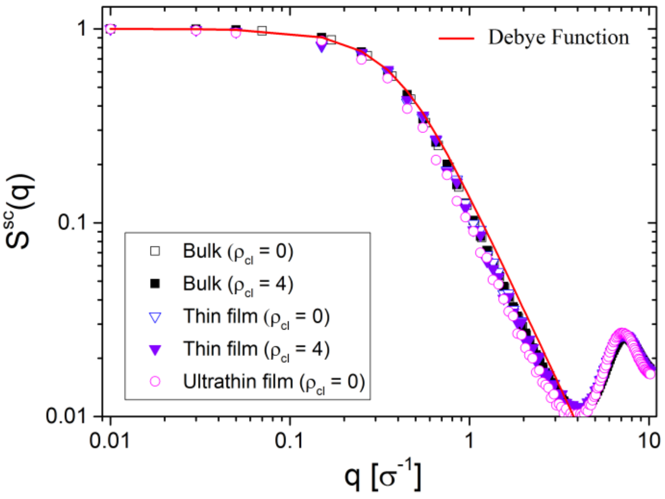

Figure 3.8: Form factor for various systems, at $T = 1.2\ \varepsilon/k_B$. For the film data, we have used wavevectors $\boldsymbol{q}$ parallel to the substrates. The slope in the scaling regime was calculated equal to -2 and -1.9 for the bulk and films, respectively, which indicates that the chains adopt random coil conformations. The Debye function is also plotted (Eq. 3.8).

3.4 Conclusions

We employed a coarse-grained copolymer model to study the thermal-volumetric and structural properties of capped polymer films. We calculated the dependence of the mentioned properties on the polymer crosslink density and on the degree of confinement (film thickness), using molecular-dynamics simulations. We characterized the thermal and volumetric properties by computing the density, the thermal expansion coefficient, as well as the glass-transition temperature.

We computed the structural properties of the mentioned systems by calculating the overall static structure factor of the monomers, and the form factor of the polymer chains. We saw that the degree of confinement did not influence the equilibrium structure of the polymer along the direction parallel to the walls. In this direction, the chains adopted Gaussian conformations, and the structure resembled that of an amorphous liquid. However, confining the polymer between the two walls led to the development of density layers along the perpendicular direction.

Last, we found that the glass-transition temperature increased linearly with an increase in the crosslink density, while it displayed a stronger dependence on the degree of confinement (increasing with a decreasing film thickness). We attribute this increase in T_g to the decreased mobility of the monomer segments when both the crosslinking density and the degree of confinement were increased. To assert this assumption, we analyzed the dynamic response of the systems in Chapter 4 of the present thesis.

References

[1] Allegra G., Raos G., Vacatello M., *Prog. Polym. Sci.* **2008**, *33*, 683-731.

[2] Rittigstein P., Priestley R. D., Broadbelt L. J., Torkelson J. M., *Nat. Mater.* **2007**, *6*, 278 - 282.

[3] Bansal A., Yang H., Li C., Cho K., Benicewicz B. C., Kumar S. K., Schadler L. S., *Nat. Mater.* **2005**, *4,* 693-698.

[4] Sen S., Xie Y., Bansal A., Yang H., Cho K., Schadler L. S., Kumar S. K., *Eur. Phys. J. Special Topics* **2007**, *141*, 161-165.

[5] Kropka J. M., Pryamitsyn V., Ganesan V., *Phys. Rev. Lett.* **2008**, *101*, 075702, 2008.

[6] Batistakis C., Lyulin A. V., Michels M. A. J., *Macromolecules* **2012**, *45,* 17.

[7] Batistakis C., Michels M. A. J., Lyulin A. V., *AIP Conf. Proc.* **2014**, *1599*, 62.

[8] Batistakis C., Michels M. A. J., Lyulin A. V., *J. Chem. Phys*. **2013**, *139,* 024906.

[9] Guseva D. V., Komarov, P. V., Lyulin A. V., *J. Chem. Phys*. **2014**, *140,* 114903.

[10] Hudzinskyy D., Lyulin A. V., Baljon A. R. C., Balabaev N. K., Michels M. A. J., *Macromolecules* **2011**, *44*, 7, 2299-2310.

[11] Liu J., Cao D., Zhang L., *J. Chem. Phys*. **2009**, *131*, 034903.

[12] Soni N.J., Lin PH, Khare R., *Polymer* **2012**, *53*, 1015-1019.

[13] Sirka T. W., Khareb K. S., Karimb M., Lenharta J. L., Andzelma J. W., McKennab G. B., Khare R., *Polymer* **2013**, *54*, 26.

[14] Shokuhfar A., Arab B., *J. Mol. Model.* **2013**, *19*, 9.

[15] Liu J., Cao D., Zhang L., *J. Chem. Phys*. **2009**, *131*, 034903.

[16] Tress M., Erber M., Mapesa E. U., Huth H., Müller J., Serghei A., Schick C., Eichhorn KJ., Voit B., Kremer F., *Macromolecules* **2010**, *43*, 23.

[17] Plimpton S., *J. Comp. Phys.* **1995**, *117*, 1.

[18] Kremer K., Grest G. S., *J. Chem. Phys.* **1990**, *92*, 5057.

[19] Tzoumanekas C., Lahmar F., Rousseau B., Theodorou D. N., *Macromolecules* **2009**, *42*, 19.

[20] Humphrey W., Dalke A., Schulten K. J., *J. Mol. Graphics* **1996**, *14*, 1.

[21] Batistakis C., Lyulin A.V., *Comp. Phys. Comm.* **2014**, *185*, 4.

[22] Kob W., Andersen H. C., *Phys. Rev. Lett.* **1994**, *73*, 1376.

[23] Kob W., Andersen H. C., *Phys. Rev. E* **1995**, *51*, 4626.

[24] Aichele M., Baschnagel J., *Eur. Phys. J. E* **2001**, *5*, 2.

[25] Mulder T., *Equilibration and deformation of glass-forming polymers: molecular simulation via connectivity-altering Monte Carlo and scale-jumping methods*, PhD Thesis, Technische Universiteit Eindhoven, 2008.

[26] Doi M., Edwards S. F., *The Theory of Polymer Dynamics*, Oxford University Press: Oxford, 1990.

Chapter 4

A coarse-grained molecular-dynamics study of segmental structure and mobility in capped crosslinked copolymer films

Abstract

In this chapter we present results from molecular-dynamics simulations of a generic bead-spring model of copolymer chains confined between solid walls and report on the segmental dynamics as a function of film thickness and mesh size (the end-to-end distance of the subchains in the crosslinked polymer networks). Apparently, the glass-transition temperature displayed a steep increase for mesh-size values much smaller than the radius of gyration of the bulk chains; otherwise it remained invariant to mesh-size variations. The rise in the glass-transition temperature with decreasing mesh size and film thickness was accompanied by a monotonic slowing-down of segmental dynamics on all studied length scales. This observation is attributed to the correspondingly decreased width of the bulk density layer that was obtained in films whose thickness was larger than the end-to-end distance of the bulk polymer chains. To test this hypothesis additional simulations were performed in which the crystalline walls were replaced with amorphous or rough walls. In the amorphous case, the high polymer density close to the walls vanished, but the dynamic response of the film was not affected. The rough walls, on the other hand, only slightly decreased the density close to the walls, and led to a minor slowing-down in the dynamics at large length-scales.

∗The contents of this chapter have been published in: *J. Chem. Phys.* **2015**, *143*, 074906.

4.1 Introduction

It is well established that polymer properties change when the material is supported on a substrate or confined between walls whose distance approaches nanoscopic length scales. Thin polymer films are important for the microelectronics industry [**1,2**], and confined polymers in general have been frequently used as a simplified model of composite materials in which confinement effects play an important role in affecting macromechanics, friction, and wear resistance [**3-6**].

Polymer nanocomposites, especially, comprise a family of materials with abundant industrial applications, e.g., in the manufacturing of car tires. The mechanical properties of elastomer-based nanocomposites, consisting of inorganic nanoparticles dispersed in the polymer matrix, depend drastically on the interactions between the polymer matrix and the nanofillers [**7,8**]. Different dynamic moduli can be obtained by tuning these interactions, which leads to the desired increase of mechanical reinforcement at low strain magnitudes. However, a significant loss of the composite's rigidity appears at higher strain magnitudes. This loss of rigidity is colloquially called the 'Payne effect' [**9**]. It is believed [**10**] that the Payne effect arises from the interrelation of the material's viscoelastic properties with its microstructure, the polymer's segmental mobility (especially in the interfacial layers), and the chemistry-specific polymer-filler interactions [**11**]. Rigorous control of molecular-scale phenomena may therefore lead to the design of improved nanocomposites with tailor-made mechanical properties. Contemporary computer simulations, complementary to experimental investigations, constitute an exemplary approach for providing additional insight into the essential physical mechanisms that are responsible for the modified mechanics of filled elastomers in relation to the mechanical properties of bulk polymers. In such composite materials additional interfaces are created once the filler volume fraction is increased, which may result in a situation where the polymer chains will be effectively confined among the filler particles [**12,13**].

To study these confinement effects we performed molecular-dynamics (MD) simulations of bead-spring polymer films confined between two solid (crystalline and amorphous) walls. Simulations of the corresponding bulk polymer were also performed to provide with necessary comparisons. In Chapter 3 [**13**] we discussed the influence of confinement and crosslink density on the structural properties of the polymer melt, whereas presently we focused our attention on segmental dynamics. The influence of the walls' structure on the density distribution and mobility of the confined polymer is also discussed. Note that we did not intend to provide a thorough review of the research efforts devoted to confinement effects, which is a formidable task in itself, but instead mentioned below only a few, and from our point of view, important studies.

The dynamics in thin polymer films have been studied extensively with a variety of experimental methods [**14-22**]. The consensus is that the dynamic response of a polymer film is highly dependent on the degree of confinement, the presence of free interfaces, and the polymer-wall interactions. The results, though, seem rather influenced by the employed experimental technique and the preparation procedure of the samples, as contradictory results have often been reported. For instance, a number of ellipsometry [**23,24**] and fluorescence [**25**] results indicate a large suppression in the T_g, whereas incoherent neutron scattering experiments suggest both enhancement and suppression in the T_g, as inferred by mobility measurements [**26 – 30**]. The effect of the polymer-wall interactions becomes important when the thickness of the film becomes smaller than a specified length scale [**22,31**]. Dynamic fragility, a measure of the glass transition abruptness of glass-forming materials, has been employed to explain why certain polymers display different confinement effects from others. For example, recent results of Evans et al. [**32**], obtained by differential scanning calorimetry experiments with single-layered polymer films supported on silicon substrates (systems with no substantial polymer-substrate interactions), showed a one-to-one correlation between higher fragility and the amplitude of the T_g shift upon changing the film thickness.

Simulations of polymer chains confined between structureless, attractive walls, have shown an acceleration in the dynamics compared to the bulk polymer [**33**]. A similar behavior has been observed in films with structured walls and high polymer density[**12**], whereas the opposite has been reported in films of lower density [**34**]. Binder et al. [**33**] performed molecular-dynamics and Monte Carlo simulations of short polymer chains confined between structureless walls, and reported an acceleration of the overall segmental dynamics upon increasing the degree of confinement. A higher segmental mobility in the interfacial layers than in the middle layers of the films was observed as well. The authors argued in favor of the lubricating effect of the walls: presumably the smooth surface did not exert any friction on nearby monomers and therefore caused an overall acceleration of the segmental relaxation process. Simulations of freely-standing atactic-polypropylene films, performed by Mansfield and Theodorou [**35**], suggested that the role played by a free interface is to increase the mobility of the nearest polymer segments, and therefore to reduce the overall glass-transition temperature of the films. Essentially, it has been confirmed that the glass-transition temperature in films is significantly different than that of the bulk, depending on the strength of the wall-polymer interactions [**36,37**]. In addition, molecular-dynamics simulations of a filler particle surrounded by polymer chains showed that for attractive polymer-filler interactions the glass-transition temperature was higher than in the pure polymer melt, whereas the opposite was observed when unfavorable adhesion interactions were employed [**38**].

Despite the high attention that has been given to the effect of confinement and adhesion interactions on the glass-transition temperature and segmental dynamics in thin polymer films, the combined effect of crosslinking and confinement is much less investigated, especially with molecular-dynamics simulations [**39**]. Lin and Khare [**40**] used a single-step polymerization algorithm to generate a crosslinked epoxy-based composite and concluded that the incorporation of filler particles (which essentially confined the polymer matrix in between) decreased the volumetric thermal-expansion coefficient but did not change the glass-transition temperature. Liu et al. [**41,42**] performed molecular-dynamics simulations of model elastomers to study the effect of temperature, pressure, and crosslink density variations on structure and dynamics. They reported an increased glass-transition temperature T_g with increased pressure or degree of crosslinking, and showed that the *time-pressure* superposition principle was valid at the chain length scale but failed at smaller scales, seemingly due to the increased heterogeneity in the relaxation of the incoherent scattering function, whereas the opposite was observed for the *time-temperatrure* superposition. Fan and Yuen [**43**] simulated the glass-transition temperature, the linear thermal-expansion coefficients, and Young’s modulus of cured epoxies, and showed that the simulated thermomechanical properties were in close agreement with experimental results. Bandyopadhyay et al. [**44,45**] studied the distribution of crosslinks in epoxy polymers and found that the coefficient of thermal expansion (CTE) decreased with increasing the degree of crosslinking, and attributed their observations to the (crosslink induced) inhibition of the polymer-network volume expansion upon heating. Yang et al. [**46**] employed

MD simulations to calculate a collection of thermomechanical properties in crosslinked epoxy networks: upon crosslinking the T_g increased whereas the CTE in the rubbery state decreased. They also showed that the CTE in the glassy state did not depend on the curing degree, in good agreement with existing simulations.

The purpose of the present study is to provide with rather general insights on the effects that the surface structure (crystalline vs amorphous), crosslink density ρ_{cl} and film thickness L_{film} may exert on the glass-transition temperature and segmental relaxation of the bead-spring copolymer model. Further, we aim to produce a basis for future studies which will attempt to connect the macroscopic mechanical properties to the microscopic dynamics that are observed in similarly confined polymer models. Therefore, no effort was made to provide a one-to-one correspondence with experimental results since we are interested in the generalized “universal” behavior of confined polymers and not in properties that may depend on chemical details. Implications concerning the development of heterogeneous dynamics in polymer films are also discussed.

The employed model is described in Section 4.2. In Section 4.3 we present our findings on the influence of variations in crosslink density and confinement on the glass-transition temperature in films with crystalline walls. Subsequently, we consider the segmental relaxation by means of the incoherent intermediate scattering function, which can be probed by neutron scattering experiments and allows the examination of the dynamic response of the films on different length scales. This section culminates in a discussion concerning the influence that was exerted by the geometrical properties of the walls on the structure and dynamics of the confined polymer, which was modeled by means of the spatial distribution of monomers upon replacing the crystalline walls with amorphous ones. The Chapter is finalized in Section 4.4 with conclusions.

4.2 Simulated models and methods

We performed molecular-dynamics constant temperature – constant pressure (NPT) simulations of coarse-grained, amorphous polymer systems consisting of non-entangled polymer chains, confined between two crystalline or amorphous walls. The simulations were performed using the LAMMPS MD software package [**47**]. Newton’s equations of motion were integrated using the velocity-Verlet algorithm with a time step of δt = 0.001τ. Periodic boundary conditions were implemented in all three dimensions of the simulation box. The polymer melt consisted of 100 linear random copolymer chains of 50 monomers per chain. 40 of the monomer units in each chain (type A) were of different type than the rest (type B). Each crystalline wall was composed of three lateral layers of equally sized non-bonded beads arranged in a hexagonal closed packed regular lattice. They were periodically infinite along the lateral dimensions and confined the polymer melt along the perpendicular direction (Chapter 2, Fig. 2.1). We used three layers, which along with their periodic images amounted to six layers for each of the two walls, to avoid interactions among the polymer chains and their periodic images. The thickness of the six crystalline wall layers was calculated equal to 4.64σ regardless of temperature or pressure (for the units of measurement, refer to Chapter 2.3).

Non-bonded interactions were modelled with a modified Lennard-Jones (LJ) 12-6 potential,

$$U_{nb}(r) = 4\varepsilon\left[\left(\frac{\sigma}{r}\right)^{12} - \left(\frac{\sigma}{r}\right)^{6}\right] + S_{f(r)} \;\; (r < r_{cut}^{out}) \qquad (4.1)$$

In Eq. 4.1, $S_{f(r)}$ denotes a switching function that ramped the energy (and force) smoothly to zero between $r_{cut}^{in} = 3.25\sigma$ and $r_{cut}^{out} = 3.50\sigma$ [**23**].The LJ parameters for the monomer units were $\sigma_{\mathrm{AA}} = \sigma$, $\varepsilon_{\mathrm{AA}} = \varepsilon$, $m_{\mathrm{A}} = m$, $\sigma_{\mathrm{BB}} = 1.2\sigma$, $m_{\mathrm{B}} = (\sigma_{\mathrm{B}})^3 m$, $\varepsilon_{\mathrm{BB}} = \varepsilon$, and for the beads of the crystalline walls $\sigma_{\mathrm{SS}} = 0.85\sigma$ and $\varepsilon_{\mathrm{SS}} = 100\varepsilon$. The LJ parameters between beads of different types were calculated according to Lorentz-Berthelot rule, $\sigma_{ij} = \left(\sigma_{ii} + \sigma_{jj}\right)/2$, but the LJ energy parameters were predefined, *i.e.*, $\varepsilon_{\mathrm{AB}} = \varepsilon_{\mathrm{AW}} = \varepsilon_{\mathrm{BW}} = \varepsilon$. The interaction strength between wall beads, $\varepsilon_{\mathrm{WW}}$, was chosen high enough to ensure the crystallinity of the walls was never broken. This high value of $\varepsilon_{\mathrm{WW}}$ was the reason of the relatively small timestep magnitude that was chosen. The size of the wall beads, $\sigma_{\mathrm{WW},}$ was smaller than the smallest monomer type to avoid the adsorption of the monomer units on the internal wall layers [**14**]. The chosen parameters were based on previous studies of similar model systems [**12**]. The amorphous walls were created by increasing the diameter of a random number of wall-beads from its original value of 0.85σ to 1.10σ whereupon the whole system was relaxed to a new state of equilibrium.

Covalently bonded beads interacted through a combination of an attractive Finite-Extensible-Nonlinear-Elastic (FENE) potential and a repulsive and truncated LJ 12-6 potential (Chapter 2, 2.7) [**15**]. The stiffness and maximum elongation of the bonded potential were set equal to $k_{\mathrm{FENE}} = 30\ \varepsilon/\sigma^2$ and $r_{\max} = 1.5\sigma$ respectively. The LJ parameters ε and σ had the same values as their non-bonded counterparts. This particular choice of bonded and non-bonded interactions prevents chain crossings [**16**] and full crystallization [**17,18,43**], and allows the system to undergo a transition to a supercooled state, allowing thus the study of the glass-transition temperature in a generalized context (i.e., disregarding material-specific properties). Further, bead-spring polymer chains do not become stiffer with decreasing temperature. The effect of these characteristics of the employed model on the conformational behavior of the chains, especially at low temperatures, was not included in the present investigation. Last, we note that the smaller length scale accessible to these kinds of models is related to the typical Kuhn-length values of rubbers (about $1nm$) [**48**].

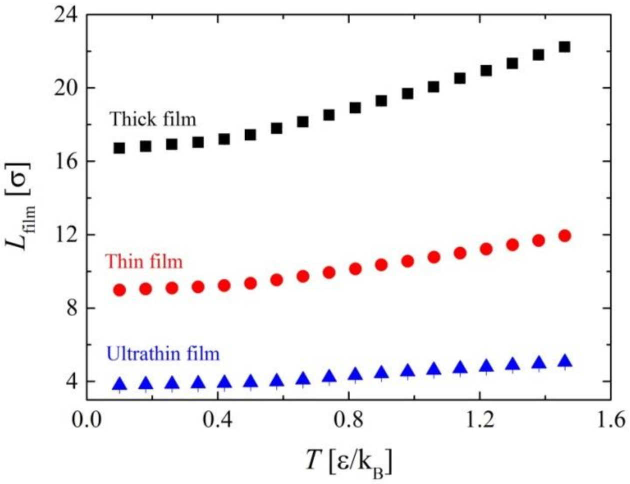

Figure 4.1: Simulated film thickness as a function of temperature in the films with crystalline walls. The thickness of the film was decreasing with decreasing temperature, while the average lateral dimensions of the periodic box remained constant owing to the crystallinity of the walls. In each case, an average isotropic pressure $P = 0\varepsilon/\sigma^3$ was imposed on the whole system. The error bars were smaller than the size of the data points.

Three polymer films with different thickness were simulated. At fixed temperature $T = 0.8\ \varepsilon/k_{\mathrm{B}}$ and isotropic pressure $P = 0\ \varepsilon/\sigma^3$ the thicknesses of the films with crystalline walls were 18.8σ (thick film), 10.1σ (thin film), and 4.3σ (ultrathin film), which approximately corresponded to 5.2, 2.8, and 1.2 times, respectively, larger than the average radius of gyration of the chains in the non-crosslinked bulk. Films with different thickness had different lateral dimensions so that, under constant number of monomer beads, they would have the same film-averaged mass density at fixed temperature and pressure, thus retaining the same statistical quality of the simulation results. Due to the crystallinity of the walls the lateral dimensions of each film were only approximately equal, but in all cases the difference was smaller than 0.5σ. The thickness of the films decreased with decreasing temperature, with a larger absolute decrease observed in thicker films (Fig. 4.1).

During both the equilibration and production runs we used the values recommended in the LAMMPS manual for the thermostat and barostat parameters, *i.e.*, the temperature and pressure were allowed to relax to the specified value over a time-span of 0.1τ and 1.0τ, respectively [**47**]. We regarded the simulated systems as equilibrated after the autocorrelation function $\varphi_{\mathrm{ee}}(t)$ of the end-to-end vector $\boldsymbol{R}_{\mathrm{ee}}$ of the chains (Chapter 2, Eq. 2.8) had decayed to zero. In reality, we allowed the systems to equilibrate for longer times ($\Delta t \approx 90{,}000\tau$) than the relaxation time of φ_{ee} to ensure that a thorough equilibration was established. The equilibration procedure was described in more detail in Chapter 3 [**13**].

We simulated both crosslinked and non crosslinked polymer systems, using a static method of crosslinking to produce the polymer networks. Namely, the last snapshot of the equilibration trajectory of each system was used to create crosslink bonds between randomly chosen pairs of monomer units (regardless of their type) until the desired value of the crosslink (number) density (Chapter 2, Eq. 2.8) was achieved. The following crosslinking protocol was employed: First, all the monomer pairs belonging to different polymer chains lying at a distance shorter than 1.4σ (smaller than the maximum elongation length of the FENE springs) were identified. Subsequently, the order of the chosen pairs was “shuffled” using a pseudo random number generator. Last, a number of those pairs were linked by the same FENE springs, starting from the first one in the shuffled sequence, until the target crosslink density was reached. Using this method, crosslinked clusters were created with only a small fraction of free (non-crosslinked) chains. We used the following crosslink density values of $\rho_{cl} = \{1, 2, 3, 4, 8\}$ crosslinks per chain, which corresponded to a variable mesh size (the end-to-end distance of the subchains) $L_{\text{mesh}} = \{4.7, 3.0, 2.3, 2.2, 1.7\}\sigma$. The L_{mesh} values were calculated directly from the simulation trajectories. The standard deviation of the average mesh-size values was approximately $0.8 - 1.7\sigma$ (higher average value of the mesh size corresponded to a higher standard deviation). Thus, the polydisperisty of the end-to-end distance of the sub-chains of the crosslinked mesh was rather high, since the standard deviation was comparable to the average mesh size value. We also note, that a number of free chains was always present in the crosslinked systems.

The end-to-end distance of the polymer chains was calculated equal to $R_{ee} = 8.9 \pm 0.1\sigma$, by averaging over all studied systems at T = 0.8 ε/k_B including all different crosslink densities and degrees of confinement, and the radius of gyration was $R_g = 3.6 \pm 0.1\sigma$. The latter was found not much different than the radius of gyration of the bulk polymer chains at the same temperature, $R_g^0 = 3.7 \pm 0.1\sigma$. The spatial distribution of crosslinks along the direction perpendicular to the walls displayed some deviations from uniformity, as a higher concentration of crosslinks was produced closer to the walls. This was probably due to a higher polymer density in the polymer-wall interfacial layers than in the middle of the films [**13**].

The effect of film thickness and mesh-size on segmental mobility was studied at temperatures above $T_g(L_{\text{film}}, L_{\text{mesh}})$, *i.e.*, above the glass-transition temperature of a specific film of thickness L_{film} and mesh size L_{mesh}. All simulated systems can be safely regarded as well-equilibrated in this high-temperature range. To further study the relaxation of single ‘particle’ motions we calculated the incoherent intermediate scattering function $S_{\text{inc}}(q,t)$ (Chapter 2, Eq. 2.10), which is measured in neutron-scattering experiments to probe the various relaxation modes in macromolecular systems on different length scales [**19, 20**]. In Section 4.3 we present our simulation results of the incoherent relaxation in the region between q = 7.0 σ^{-1}, which corresponded approximately to the first peak in the overall static structure factor [**13**], and q = 1.0 σ^{-1}, which corresponded to a length scale between the end-to-end distance and the gyration radius of the chains. The $S_{\text{inc}}(q,t)$ for a given q was computed by calculating the average value of three wave vectors $\boldsymbol{q}$ with the same magnitude but different directions along the primary Cartesian axes, unless otherwise stated.

4.3 Results and Discussion

4.3.1 Glass-transition temperature

Simulations of coarse-grained polymers can only access dynamical processes on scales larger than the effective bead size; local (intra-monomer) scale dynamics are inaccessible. Nevertheless, these large scale dynamics are those which are mainly responsible for controlling the rheological properties of a glass-forming material [**49**]. These properties depend considerably on how larger or smaller is the working temperature from the T_g, and therefore we devoted a part of our research for the computation of the glass-transition temperature of the studied films.

We followed a volumetric method to calculate the T_g (Fig. 4.1), which is similar to the experimental determination of the T_g using ellipsometry. The procedure was the same as the one followed in Chapter 3. Namely, after the simulated systems were equilibrated at $T = 1.5\ \varepsilon/k_B$ and $P = 0\ \varepsilon/\sigma^3$, we performed *NPT* simulations during which we kept lowering the temperature by $0.02\varepsilon/k_B$ per $10^3\,\tau$ in a stepwise fashion from $1.5\ \varepsilon/k_B$ to $0.1\varepsilon/k_B$. The T_g was determined from the change in slope of the film-averaged density-temperature curves above and below the glass-transition region [**13, 14**].

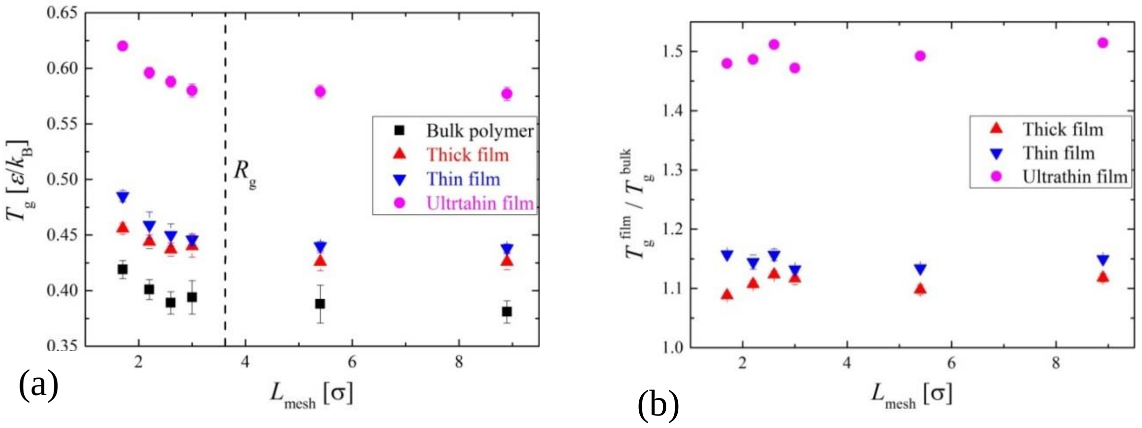

(a) (b)

Figure 4.2: The dependence of the glass-transition temperature (a) and the ratio of the glass-transition temperatures among the films and the bulk polymer (b) on the mesh size, for films of different thickness.

The simulations showed that the T_g values were affected by variations in both crosslink density (or equivalently, the mesh size L_{mesh}) and film thickness, but to a different extent. The calculated T_g in the films was higher than the T_g in the bulk under the same constant mesh size value (Fig. 4.2). A smaller film thickness resulted in a higher T_g. The size of the crosslinked mesh was found to affect the T_g only when $L_{mesh} \ll R_g$, where R_g is the radius of gyration of the non-crosslinked chains. Confinement led to a strong increase of the glass-transition temperature compared to the corresponding bulk values. The T_g^{film} / T_g^{bulk} ratio, however, was not affected by the mesh size, and was equal to 1.1, 1.15, and 1.5, for the thick, thin, and ultrathin film, respectively (Fig. 4.2b). A gradual alignment of the intra-chain bonds parallel to the crystalline walls was observed near the polymer-wall interface as the temperature was approaching the glass-transition value (not shown).

4.3.2 Segmental dynamics

Overall, a smaller film thickness or a smaller mesh size resulted in a slower relaxation of single-bead motions. It should be noted, though, that these two parameters were not decoupled: a change in the mesh size induced also a small change in the film thickness. The change in thickness among the non-crosslinked and the highest crosslinked films (L_mesh = 1.7σ) was 3%, 2%, and 4% for the thick, thin and ultrathin films, respectively, at T = 0.8 ε/k_B. At the same temperature, the large-scale long-time decay of the film-averaged $S_{inc}(q,t)$ culminated in non-zero plateaus whose magnitude depended on q, when large-scales motion were probed [**21**].

Since no plateaus were detected in the relaxation of the film averaged $S_\mathrm{inc}(q,t)$ in the non-crosslinked polymer bulk, their appearance in the non-crosslinked films can be reasonably attributed to the confinement effect of the walls, *i.e.*, to the induced maximum attainable displacement of the polymer segments along the direction perpendicular to the walls. In those systems, plateaus were observed on large length-scales, *i.e.*, length-scales comparable to the size of the polymer chains, Figure 4a. As the film thickness decreased, and larger length-scales were probed, the magnitude of the plateaus increased. In the thick ($L_\mathrm{film} \approx 18.8\sigma$) and thin ($L_\mathrm{film} \approx 10.1\sigma$) films, at T = 0.8 ε/k_B, the film averaged relaxation displayed a pronounced plateau only at $q = 1.0\sigma^{-1}$ ($l_1 = 6.3\sigma$) and, presumably, at larger length-scales. In the ultrathin film, however, we observed plateaus already for $q < 3.0\sigma^{-1}$, *i.e.*, for scattering lengths $l_\mathrm{q} > 2.1\sigma$. The film thickness in this case, $L_\mathrm{film} \approx 4.3\sigma$, was smaller than the largest probed length-scale, $l_1 = 6.3\sigma$. In contrast, the relaxation of $S_{\text{inc}}^{||}(q_{xy}, t)$, when only dimensions parallel to the walls were taken into account, always decayed to zero, Figure 4b. In general, at T = 0.8 ε/k_{B}, plateaus in the relaxation of the film averaged $S_{\text{inc}}(q, t)$ were observed on length-scales that were at least half the film thickness.

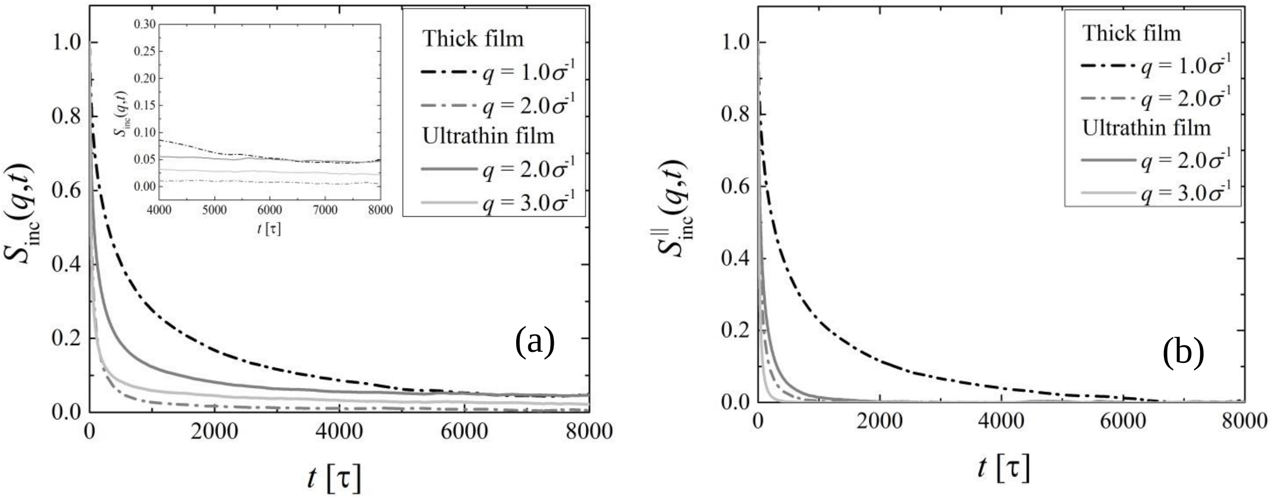

Figure 4.3: Relaxation of $S_{\text{inc}}(q, t)$ in the non crosslinked thick and ultrathin film at $T = 0.8\ \varepsilon/k_{\text{B}}$ and $P = 0.0\ \varepsilon/\sigma^3$. Only large scale relaxations are shown, *i.e.*, $q = \{1, 2, 3\}\sigma^{-1}$ or $l_{\text{q}} = \{6.3, 3.1, 2.1\}\sigma$. The values of q were calculated by averaging over $\boldsymbol{q}$ vectors with the same magnitude q along the three principal Cartesian axes (a) and the two Cartesian axes parallel to the walls (b).

The appearance of non-zero plateaus in the relaxation of $S_{\text{inc}}(q, t)$ was more noticeable in the crosslinked systems, which indicates the extra hindrance to large-scale flow upon crosslinking (Fig. 4.4). The influence of the mesh size on the magnitude of the plateaus was stronger than the influence of the film thickness. The decay of $S_{\text{inc}}(q, t)$ at q = 1.0σ^{-1} was significantly slower in the strongly crosslinked systems, due to the considerable constraints that were imposed by the crosslinks on large scale motions. On the other hand, on shorter scales, where the mesh size was comparable or even larger than the probed length scale of relaxation l_{q}, the mesh size had a much weaker effect on the decay of $S_{\text{inc}}(q, t)$. For instance, the mesh size in the highest crosslinked systems, $L_{mesh} = 1.7\sigma$, was noticeably larger than the shortest length scale of relaxation, $l_7 = 0.9\sigma$, and therefore could not have affected the mobility of such small segments.

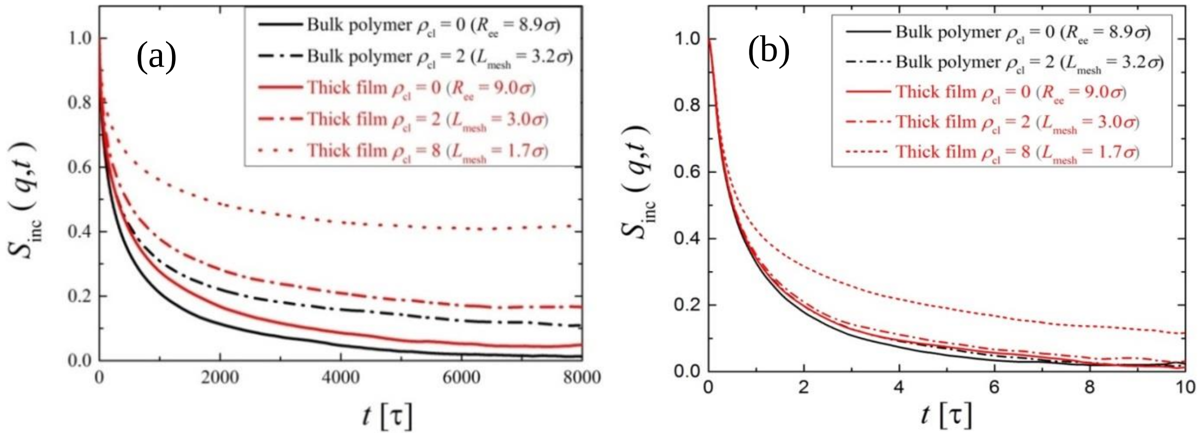

Figure 4.4: Decay of $S_{inc}(q,t)$ at (a) the chain scale defined by $q = 1.0\sigma^{-1}$ and (b) the monomer scale defined by $q = 7.0\sigma^{-1}$. For illustrative purposes, only the relaxation in the thick film and the bulk polymer are shown. The decay of $S_{inc}(q,t)$ in the rest of the films was qualitatively similar. The temperature was $T = 0.8\ \varepsilon/k_B$, and the average pressure was held equal to zero. Results are shown for non-crosslinked systems and for $\rho_{cl} = 2$, 8 crosslinks per chain.

To account for the non-zero plateau values in the decay of $S_{inc}(q,t)$ we extracted the relaxation times of $S_{inc}(q,t)$ by fitting it with a modified form of the KWW stretched exponential function [**43**],

$$S_{inc}(q,t) = (1-\alpha)\exp\left[-\left({}^{t}/_{\tau_q}\right)^{\beta}\right] + \alpha \tag{4.2}$$

In Eq. 4.2, α is the magnitude of the plateau, and τ_q is the characteristic time of relaxation on a length scale defined by the magnitude q. The exponent β is used to quantify the deviation from the exponential decay. Values of β that are smaller than unity can be attributed either to the development of heterogeneous dynamics or to a single homogeneous (but non exponential) relaxation mechanism [**43**].

The obtained characteristic relaxation times displayed a dependence on film thickness and mesh size that was similar to the dependence of the glass-transition temperature on the same parameters (compare Figures 4.2 and 4.5).

The $\tau_q^{film}/\tau_q^{bulk}$ ratio displayed a similar behavior, whereas (as we have already mentioned) the T_g^{film}/T_g^{bulk} ratio was not affected by the size of the crosslinked mesh. The Kuhn-length of the polymer chains was calculated equal to $L_K = 1.55\sigma$, based on the end-to-end distance of the chains, averaged over all the simulated systems. The onset of the increase in the relaxation times can be distinguished at a length-scale in-between the radius of gyration and the Kuhn-length of the polymer chains, which may indicate the characteristic alpha-relaxation scale.

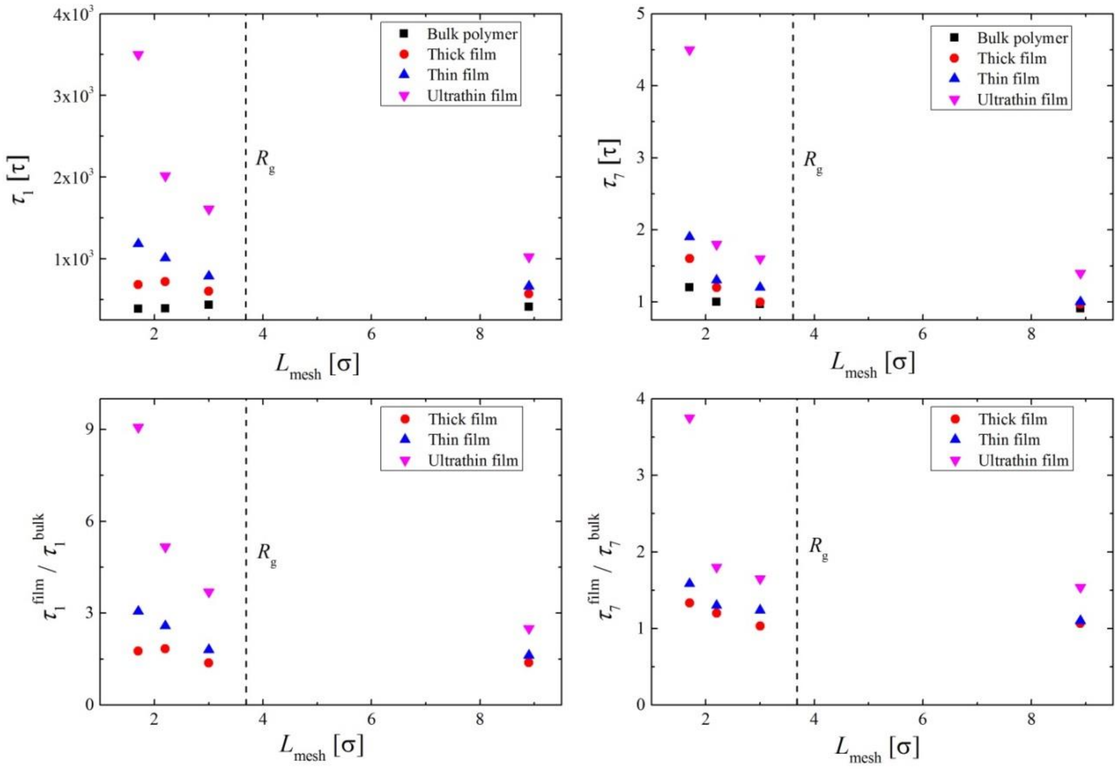

Figure 4.5: Evolution of characteristic relaxation times τ_q with mesh size for different values of the film thickness. Results are shown at two different length-scales: the chain scale, defined by $q = 1.0\sigma^{-1}$ (left panel), and the segmental scale, defined by $q = 7.0\sigma^{-1}$ (right panel).

For Rouse segmental dynamics [**50**], the dependence of the relaxation time τ_q on the probed length scale is expected to follow the power law $\tau_q \sim q^{-4}$, though in polymer melts approaching the glass-transition, a crossover to a time scaling of $\tau_q \sim q^{-2}$ can be observed, signifying a departure from dynamic homogeneity[51]. In any case, in thin polymer films a departure from homogeneity should be anticipated even when temperature is larger than T_g.

To examine the power law scaling $\tau_q \sim q^{-m}$, we fitted the calculated relaxation times at $T = 0.8\, \varepsilon/k_B$ in the interval $q \in [1.0, 7.0]\sigma^{-1}$ (Fig. 4.6a) [**13**]. The value of the scaling exponent m displayed a non-monotonic dependence on confinement. Concerning its dependence on the mesh-size, m values were fluctuating around 3.2 in the non- and weakly-crosslinked systems, depending on film thickness (Fig. 4.6b). For mesh-size values smaller than the radius of gyration of the bulk polymer chains, the value of m decreased rapidly. This decrease might have been induced by increased heterogeneity caused by the presence of the crystalline walls.

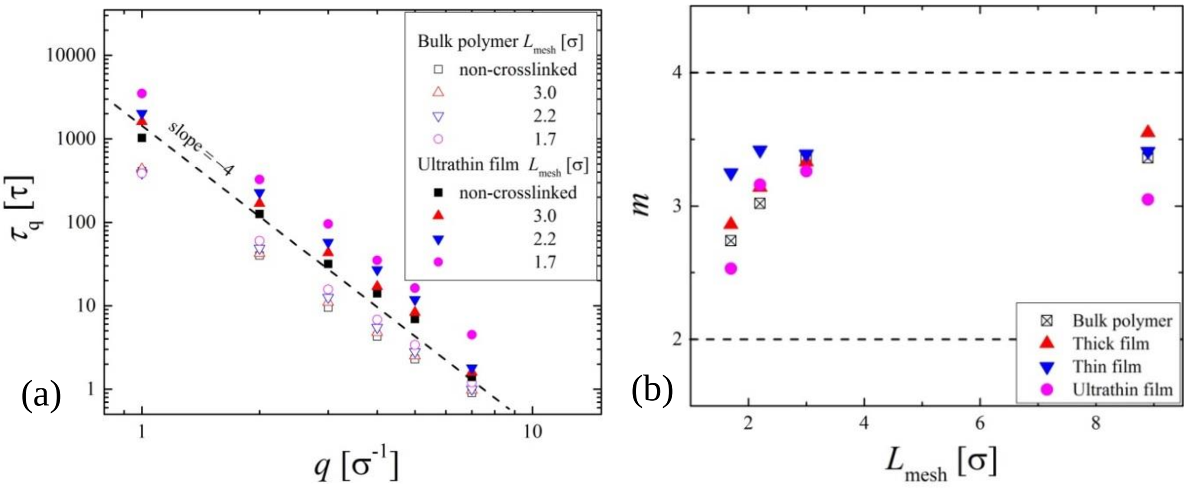

Figure 4.6: (a) Dependence of the characteristic relaxation times τ_q on the magnitude of the scattering vector q for the bulk polymer and the ultrathin film at different values of the crosslinked mesh size. The temperature is $T = 0.8\ \varepsilon/k_B$. (b) Dependence of the scaling exponent m on the mesh size.

Higher dynamic heterogeneity in thinner films with higher crosslink density was also implied by the KWW β exponent, which displayed a similar qualitative behavior upon changing the film thickness or mesh size, as smaller values of β imply a broader distribution of relaxation times which is in turn related to the higher dynamic fragility of glass-forming polymer melts [**43**]. The exponent β decreased linearly with a decreasing mesh size for $L_{\mathrm{mesh}} > R_g$, after which a rather steep decrease was observed for mesh-size values smaller than R_g (Fig. 4.7).

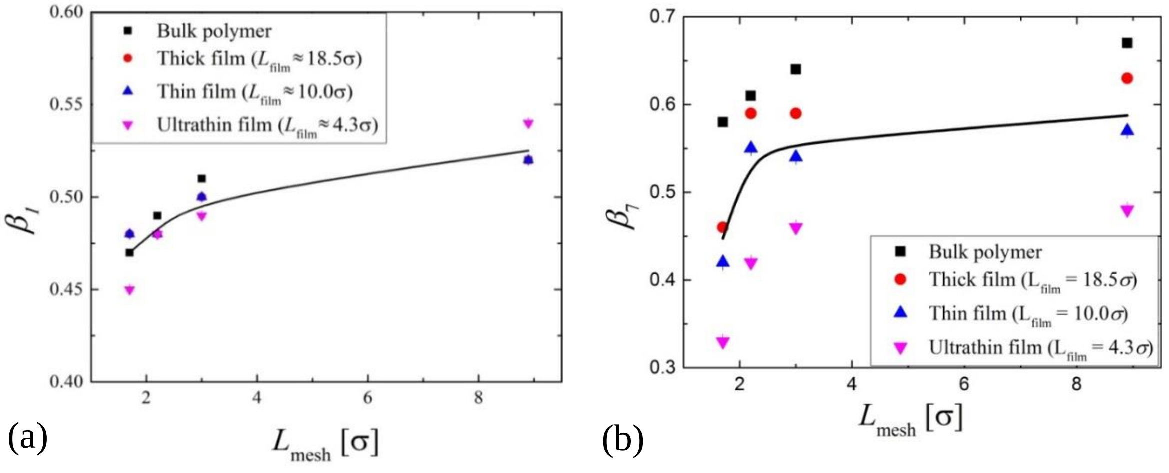

(a) (b)

Figure 4.7: The KWW β coefficient at $q = 1.0\sigma^{-1}$ and $q = 7.0\sigma^{-1}$as a function of the mesh size for different values of film thickness at temperature T = 0.8 ε/k_B. Smaller values of β imply a broader distribution of relaxation times. Evidently, shortening the mesh size resulted in a similarly weak decreasing of β on all studied length-scales, whereas the effect of film thickness was more significant on smaller length-scales rather than larger ones. The solid line represents the mean value of the data points averaged over all values of the film thickness.

This behaviour was detected for all simulated length scales (0.9σ to 6.3σ). On the other hand, the effect of confinement on β was more pronounced when small size segments were probed, *i.e.*, $l_q < 2.1\sigma$, whereas it was gradually damped on larger length-scales. On these scales, thinner films displayed lower β values. This is illustrated in Fig. 4.8 where a higher deviation from the Arrhenius temperature dependence of the characteristic relaxation time can be seen in more crosslinked and thinner films. The monotonic decrease of the β coefficient with decreasing mesh size is in agreement with previously published simulation results [**43**], while similar results have also been obtained experimentally in bulk polymer networks [**52–54**]. We assume the spatial distribution of crosslink bonds deviated from the homogeneous case, and since the mobility of a monomer bead depends on the mobility of its neighboring beads, distinct monomer beads were exposed to different dynamic environments.

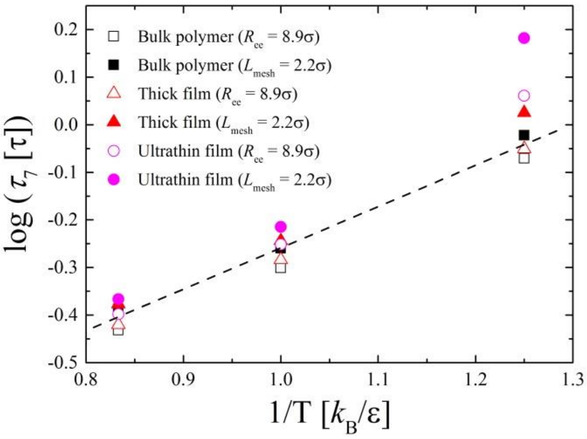

Figure 4.8: Temperature dependence of local (segmental) relaxation times. A larger deviation from the Arrhenius dependence was observed upon decreasing the mesh size or the film thickness. The dashed line illustrates the Arrhenius dependence.

4.3.3 Effect of wall structure

Thinner films, as well as any film in relation to the bulk polymer, displayed a larger deviation from the Rouse dynamics, lower values of the film averaged KWW β exponent, and a larger deviation from the Arrhenius temperature dependence of the characteristic relaxation times. These results may be attributed to the increased number of oscillations in the density distribution of the monomer beads along the direction perpendicular to the walls [**13**]. At a distance $z < 4\sigma$ from the walls the monomer units were distributed in oscillating density layers of gradually decreasing amplitude (Fig. 4.9), which has already been reported by previous simulation results in films [**12**], as well as in nanocomposites [**55**]. The average density farther away from the walls in the thick and thin films was constant and equal to the bulk value, whereas in the ultrathin film $(L_{\text{film}} < R_{\text{g}})$ no bulk density layer was observed. Overall, the bulk density layer was smaller in thinner films. The density distribution along the direction perpendicular to the walls was therefore more inhomogeneous in thinner films, which might have induced the development of distinct dynamic environments, thus leading to a wider spectrum of relaxation processes.

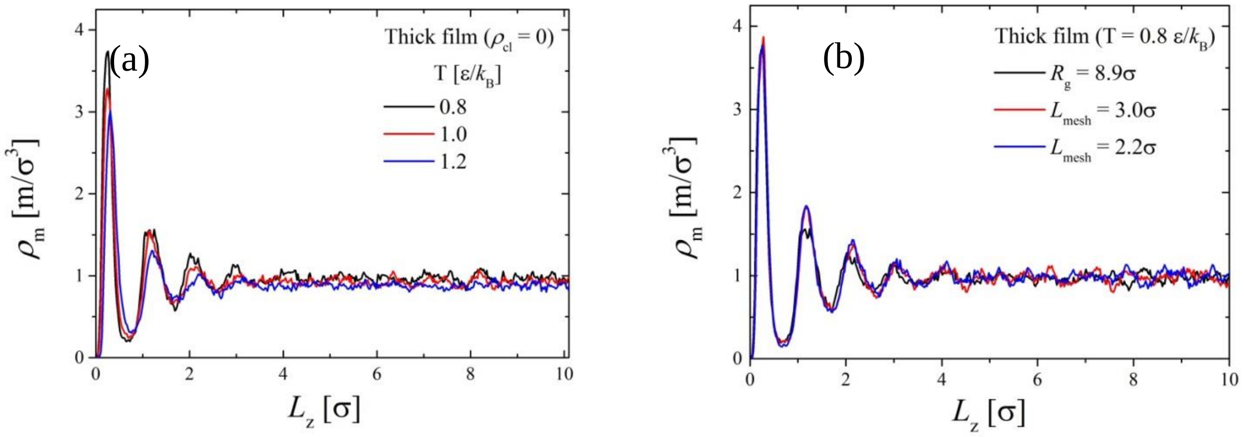

Figure 4.9: Spatial distribution of the polymer mass density as a function of the distance from the crystalline walls along the perpendicular direction (in the thick film). Only half of the film is shown. (a): Density distribution in the thick film at different temperatures. (b): Density distribution in the thick film with different mesh size values at $T = 0.8\ \varepsilon/k_{\mathrm{B}}$. The width and position of the density layers were not affected by either mesh size or temperature.

The structure of the films perpendicular to the walls was not affected noticeably by the mesh size (Fig. 4.9b), whereas a higher temperature resulted in a decreased amplitude of peaks in the density profile (Fig. 4.10a). This effect was damped for the density layers farther away. This observation is attributed to entropic effects resulting in a less ordered packing of the monomer units at higher temperatures, which led to a decreased film-averaged polymer density. Note also that although the film-averaged density was smaller at lower temperatures, the density layers appeared at the exact same distance from the wall. The fact that the positions of the oscillating density layers fell on top of each other in the three films implies a constant thickness of the wall-polymer interphase independent of the thickness of the film.

Note that the calculated density distributions were identical regardless of whether we performed the simulations under the NPT or NP$_z$T ensemble (not shown), during the latter of which we only allowed the pressure component perpendicular to the walls to fluctuate around $P_{zz} = 0\varepsilon/\sigma^3$ while keeping the lateral pressure components constant.

To affirm whether the observed ordering of the monomer beads close to the walls was induced by the latter's crystalline structure, we performed additional simulations, first, of the thick film at $T = 1.5\ \varepsilon/k_B$, in which the crystalline walls were replaced with amorphous walls, and second, of all the films (thick, thin, and ultrathin), at $T = 0.8\,\varepsilon/k_B$, in which we replaced the crystalline with rough walls (Chapter 2, Fig. 2.2).

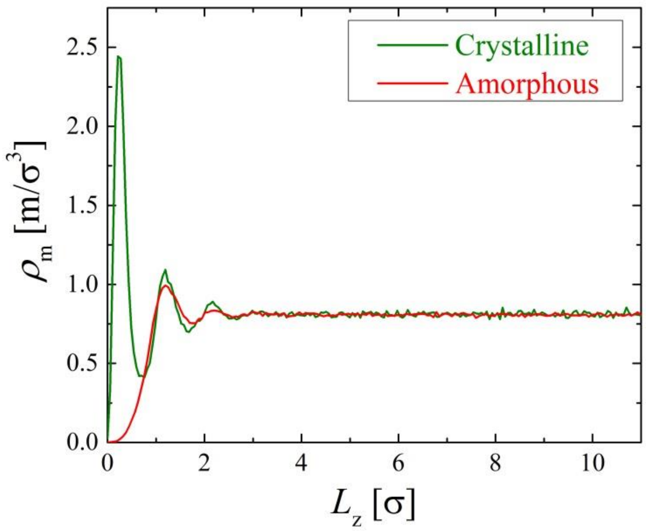

Figure 4.10: Spatial distribution of the polymer mass density in the non-crosslinked thick film as a function of the distance from a wall, calculated from an *NPT* simulation at isotropic pressure $P = 0.0\,\varepsilon/\sigma^3$and $T = 1.5\,\varepsilon/k_B$. Only half of the film is shown.

The amorphous walls were created by increasing the diameter of half of the wall beads from their original value of 0.85σ to 1.10σ whereupon we let the whole system equilibrate at the same temperature under *NPT* conditions. We subsequently subjected the thick film to *NPT* simulations, at temperature $T = 1.5\,\varepsilon/k_B$ and isotropic pressure $P = 0.0\,\varepsilon/\sigma^3$, for $\Delta t = 20{,}000\tau$. During the simulations the volume of the simulation box increased from $V_{box} = 7357\sigma^3$, which was obtained during the *NPT* simulation of the thick film with crystalline walls at the same operating conditions, to $V_{box} = 7741\sigma^3$. The calculated density profiles (Fig. 4.10), indicate that the pronounced density layer, which was observed close to the crystalline walls, disappeared when amorphous walls were used. At the same time the density profile throughout the rest of the film was not affected by the structure of the walls.

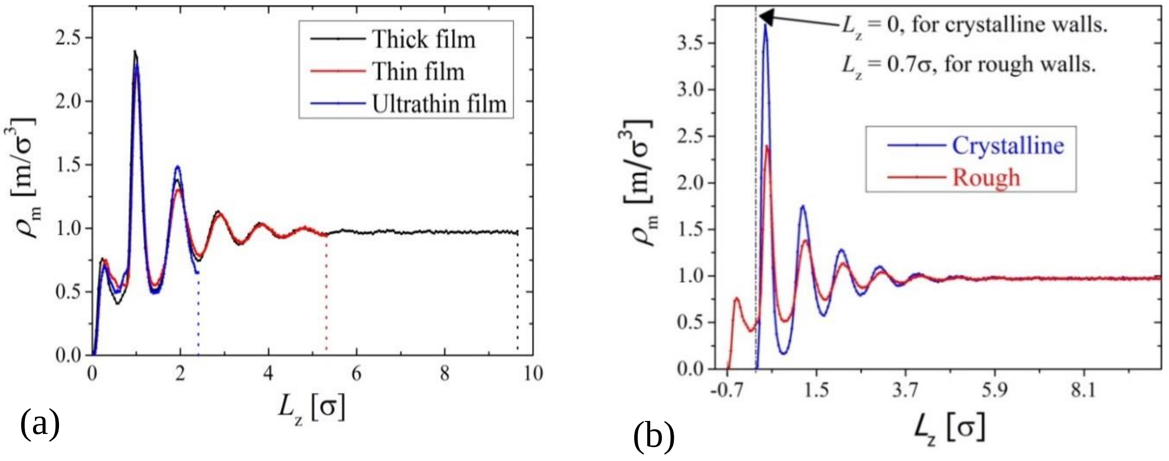

Figure 4.11: Spatial distribution of the polymer mass density in the non-crosslinked films as a function of the distance from one of the walls. Only the half part of the films is shown, which is denoted by the dashed vertical lines. The density profiles were calculated from NPT simulations at isotropic pressure $P = 0.0\,\varepsilon/\sigma^3$ and $T = 0.8\,\varepsilon/k_B$. (a) A comparison of the three films with rough walls. (b) Density distribution in the thick film with crystalline and rough walls.

To create the rough walls, we deleted half of the beads in the two internal surfaces (that were in contact with the polymer). Since the distance between two vertical layers in an HCP crystalline solid is $l_z = \sigma_{ss}\sqrt{6}/3$, the removal of the beads resulted in a roughness width of 0.7σ (the diameter of the spheres comprising the walls were $\sigma_{ss} = 0.85\sigma$). This can be clearly seen in Fig. 4.10b. We subsequently performed NPT simulations at constant isotropic pressure $P = 0.0\,\varepsilon/\sigma^3$, and $T = 0.8\,\varepsilon/k_B$.

According to the simulation results the thickness of all three films (thick, thin, and ultrathin) attained immediately a smaller value than the thickness of the corresponding films with crystalline walls, though presumably the free volume available to the polymer chains remained constant in all cases. The decrease in film thickness was close to 1.5% for the thick film, and smaller for the rest of the films. Additionally, when rough walls were used, the density profiles overlapped for all studied values of the film thickness. Thus, only the width of the bulk-density layer was affected by the value of the film thickness. The same observation was also made in films with crystalline walls [**6**]. The density profiles for films with rough walls are illustrated in Fig. 4.11a which illustrates clearly that the bulk-density layer, which was present in the middle of the thin film with crystalline walls [**13**], disappeared when rough walls were used; thus, it was present only in the thick film. The average thickness of the thin film was $L_{\mathrm{z}} = 10.1\sigma$ for crystalline walls, and $L_{\mathrm{z}} = 9.6\sigma$ for rough walls, with L_{z} denoting the minimum distance between the internal surfaces of the two walls. The average end-to-end distance of the chains in the bulk polymer was $R_{ee} = 8.95 \pm 0.08\sigma$, which indicates that the bulk-density layer may already disappear even when the thickness of the film is larger than the end-to-end distance of the bulk polymer chains. In Fig. 4.11b, a comparison is offered between the thick film with either crystalline or rough walls at $T = 0.8\ \varepsilon/k_B$. After the replacement of crystalline with rough walls, the percentage of the bulk-density increased from 35.6% to 41.2% of the film thickness. An increased number of peaks was also observed.

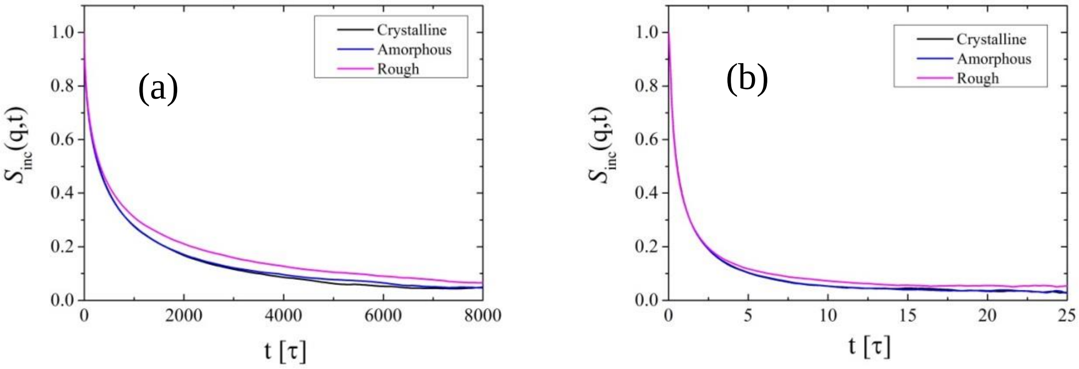

Figure 4.12: Comparison of the decay of $S_{\mathrm{inc}}(q,t)$ in the thick film with crystalline, amorphous, and rough walls at the chain (a) and segmental (b) length scales. Data were obtained at $T = 0.8\ \varepsilon/k_B$.

Turning our attention to the effect of wall structure on the dynamics, we report the following observations. Intuitively, we would expect that the combined effects induced by the replacement of the crystalline with amorphous walls (i.e., a 5% increase in the volume of the simulation box, and increased homogeneity of the density distribution) to induce faster dynamics when amorphous instead of crystalline walls were used. However, that was not the case, as the decay of $S_{\mathrm{inc}}(q,t)$ in the thick film was identical on all studied length scales (Fig. 4.12). This observation is attributed to the enhanced friction exerted on the monomers by the amorphous walls. Similarly, the introduction of wall roughness resulted in only a slight decrease in the rate of relaxation (Fig. 4.12). Lastly, the β-exponent increased by about 10% when the crystalline walls were replaced by rough ones, under constant film thickness, which implies that the use of rough walls decrease the dynamic heterogeneity of the confined polymer.

4.4 Conclusions

In this chapter we presented molecular-dynamics results concerning the glass-transition temperature and segmental dynamics as a function of film thickness and mesh size (the end-to-end distance of the subchains in the crosslinked polymer networks) of a generic bead-spring model of copolymer chains confined between solid walls.

The glass-transition temperature displayed a steep increase once the mesh size became smaller than the radius of gyration of the bulk chains; otherwise it remained invariant to mesh-size variations. The rise in the glass-transition temperature with decreasing mesh size and film thickness was accompanied by a monotonic slowing-down of segmental dynamics on all studied length-scales, as quantified by the decay of the incoherent scattering function. These observations are attributed to the constraints imposed by the presence of the walls on the maximum attainable displacement of the monomer units and to the decreased width of the bulk density layer that was obtained in thinner films. Only films whose thickness was larger than the end-to-end distance of the bulk polymer chains displayed a middle layer of bulk density.

Confinement and crosslink effects prevented certain length-scale dependent relaxation processes from relaxing fully. Higher dynamic fragility (as measured by means of the β coefficient, and the deviation from the Arrhenius dependence of the relaxation times on temperature) was observed when smaller values of film thickness and mesh size were used. More fragile glass-forming films displayed larger T_g values. The ratios of relaxation times in the films against those in the bulk displayed a steep dependence on the size of the crosslinked mesh at length-scales smaller than the bulk radius of gyration, reminiscent of the T_g dependence. The threshold from which on this behavior was observed, was independent of the film thickness. Longer chains should be used in order to elucidate on this observation.

The high polymer density that was observed close to the crystalline walls vanished when we replaced the crystalline with amorphous walls, whereas the density throughout the rest of the film remained invariant. The introduction of rough walls resulted in a higher number of oscillations in the density profile of the films, and a smaller magnitude of the oscillations in the wall-polymer interface due to a fraction of monomers becoming adsorbed inside the walls. By comparing the dynamic response amongst films with different wall structure, we reported that the wall structure affected the large-scale dynamics, only to a small degree. A higher degree of roughness could lead to slower dynamic response, though additional simulations are required to affirm this.

The next chapter deals with how the film thickness and the roughness of the walls affect the reinforcement of the films. A connection among those results and the results presented in this chapter is included in Chapter 7 of the thesis.

References

[1] Lawrence C. J., *Phys. Fluids* **1988**, *31*, 2786.

[2] Frank C. W., Rao V., Despotopoulou M. M., Pease R. F. W., Hinsberg W. D., Miller R. D., Rabolt J. F., *Science* **1996**, *273*, 912.

[3] Rittigstein P., Priestley R. D., Broadbelt L. J., Torkelson J. M., *Nat. Mater*. **2007**, *6*, 278.

[4] Bansal A., Yang H., Li C., Cho K., Benicewicz B. C., Kumar S. K., Schadler L. S., *Nat. Mater*. **2005**, *4*, 693.

[5] Sen S., Xie Y., Bansal A., Yang H., Cho K., Schadler L. S., Kumar S. K., *Eur. Phys. J. Special Topics* **2007**, *141*, 161.

[6] Kropka J. M., Pryamitsyn V., Ganesan V., *Phys. Rev. Lett*. **2008**, *101*, 075702.

[7] Saeed F., Ansarifar A., Ellis R. J., Haile-Meskel Y., Irfan M. S., *J. Appl. Polym. Sci*. **2012**, *123*, 1518.

[8] Stckelhuber K. W., Svistkov A. S., Pelevin A. G., Heinrich G., *Macromolecules* **2011**, *44*, 4366.

[9] Wang M. J., *Rubber Chem. Technol*. **1998**, *71*, 520.

[10] Allegra G., Raos G., Vacatello M., *Prog. Polym. Sci* **2008**, *33*, 683.

[11] de Castro J. G., *Understanding the viscoelastic behavior of silica filled rubber*, PhD Thesis, Universiteit van Amsterdam: Amsterdam, 2014.

[12] Batistakis C., Lyulin A. V., Michels M. A. J., *Macromolecules* **2012**, *45*, 7282.

[13] Davris T. Lyulin A. V., *Polym. Compos*. **2015**, 36, 1012–1019.

[14] Herd C. R., McDonald G. C., Hess W. M., *Rubber Chem. Technol*. **1991**, *65*, 107.

[15] Herrchen M., Ottinger H. C., *J. Non-Newtonian Fluid Mech*. **1997**, *68*, 17.

[16] Karayiannis N. C., Kröger M., *Int. J. Mol. Sci*. **2009**, *10*, 5054.

[17] Stevens M. J., *Macromolecules* **2001**, *34*, 1411.

[18] Sharp J. S., Forrest J. A., *Phys. Rev. Lett.* **2003**, *91*, 235701.

[19] Bennemann C., Baschnagel J., Paul W., *Eur. Phys. J. B* **1999**, *10*, 323.

[20] Tsoloua G., Harmandaris V. A., Mavrantzas V. G., *J. Non-Newtonian Fluid Mech*. **2008**, *152*, 184.

[21] Glomann T., Hamm A., Allgaier J., Hübner E. G., Radulescu A., Farago B., Schneider G. J., *Soft Matter* **2013**, *9*, 10559.

[22] Arbe A., Colmenero J., Monkenbusch M., Richter D., *Phys. Rev. Lett*. **1998**, *81*, 590.

[23] Fryer D. S., Peters R. D., Kim E. J., Tomaszewski J. E., de Pablo J. J., Nealey P. F., White C. C., Wu W. L., *Macromolecules* **2001**, *34*, 5627.

[24] Kawana S., Jones R. A. L., *Phys. Rev. E* **2001**, *63*, 021501.

[25] Ellison C. J., Kim S. D., Hall D. B., Torkelson J. M., *Eur. Phys. J. E* **2002**, *8*, 155.

[26] Inoue R., Kanaya T., Nishida K., Tsukushi I., Shibata K., *Phys. Rev. E* **2008**, *77*, 032801.

[27] Inoue R., Kanaya T., Nishida K., Tsukushi I., Telling M. T. F., Gabrys B. J., Tyagi M., Soles C., Wu W. I., *Phys. Rev. E* **2009**, *80*, 031802.

[28] Soles C. L., Douglas J. F., Wu W. L., Dimeo R. M., *Macromolecules* **2003**, *36*, 373.

[29] Soles C. L., Douglas J. F., Wu W. L., *J. Polym. Sci. Part B* **2004**, *42*, 3218.

[30] Soles C. L., Douglas J. F., Wu W. L., Peng H. G., Gidley D. W., *Macromolecules* **2004**, *37*, 2890.

[31] Baljon A. R. C., Van Weert M. H. M., DeGraaff R. B., Khare R., *Macromolecules* **2005**, *38*, 2391.

[32] Evans C. M., Deng, H. Jager W. F., Torkelson J. M., *Macromolecules* **2013**, *46*, 6091.

[33] Binder K., Baschnagel J., Paul, W. *Prog. Polym. Sci*. 2003, **28**, 115.

[34] Batistakis C., Michels M. A. J., Lyulin A. V., *Macromolecules* **2014**, *47*, 4690.

[35] Mansfield K. F., Theodorou D. N., *Macromolecules* **1991**, *24*, 6283.

[36] Hudzinskyy D., Lyulin A. V., Baljon A. R. C., Balabaev N. K., Michels M. A. J., *Macromolecules* **2011**, *44*, 2299.

[37] Baljon A. R. C., Williams S., Balabaev N. K., Paans F., Hudzinskyy D., Lyulin A. V., *J. Polym. Sci. Pol. Phys.* **2010**, *48*, 1160.

[38] Starr F. W., Schrøder T. B., Glotzer, S. C. *Phys. Rev. E* **2001**, *64*, 021802.

[39] Baschnagel J., Binder K., Doruker P., Gusev A. A., Hahn O., Kremer K., Mattice W. L., Müller-Plathe F., Murat M., Paul W., Santos S., Suter U. W., Tries V., *Adv. Polym. Sci*. **2000**, *152*, 41.

[40] Lin P. H., Khare R., *Macromolecules* **2009**, *42*, 4319.

[41] Liu J., Wu S., Cao D., Zhang L., *J. Chem. Phys*. **2008**, *129*, 154905.

[42] Liu J., Cao D., Zhang L., *J. Chem. Phys*. **2009**, *131*, 034903.

[43] Fan H. B., Yuen M. M. F., *Polymer* **2007**, *48*, 2174.

[44] Bandyopadhyay A., Odegard, G. M. *J. Appl. Polym. Sci*. **2013**, *128*, 660.

[45] Bandyopadhyay A., Odegard G. M., *Model. Simul. Mater. Sci. Eng*. **2012**, *20*, 045018.

[46] Yang S., Qu J., *Polymer* **2012**, *53*, 4806.

[47] Plimpton S., *J. Comp. Phys*. **1995**, *117*, 1.

[48] Mark J. E., *Physical Properties of Polymers Handbook*, 2nd ed., Springer: New York, 2007.

[49] Colmenero J., Arbe A., *J. Polym. Sci. B Polym. Phys*. **2013**, *51*, 87.

[50] Doi M., Edwards, S. F. *The Theory of Polymer Dynamics*, Clarendon Press: Oxford, 1988.

[51] Adam G., Gibbs J. H., *J. Chem. Phys*. **1965**, *43*, 139.

[52] Prochazka F., Durand, D., Nicolai T., *J. Rheol.* **1999**, *43*, 1511.

[53] Glatzreichenbach J. K. W., Sorriero L. J., Fitzgerald J. J., *Macromolecules* **1994**, *27*, 1338.

[54] Kramarenko V. Y., Ezquerra T. A., Sics I., Balta-Calleja F. J., Privalko V. P., *J. Chem. Phys.* **2000**, *113*, 447.

[55] Gao Y., Liu J., Shen J., Wu Y., Zhang L., *Phys. Chem. Chem. Phys*. **2014**, *16*, 21372.

Chapter 5

Filler size effects on reinforcement in elastomer-based nanocomposites: experimental and simulational insights into physical mechanisms

Abstract

Nanocomposites consisting of polymers reinforced with filler particles are important for a wide variety of industries and processes, but although they exhibit unique viscoelastic properties and as such are widely applied in e.g. tires, the precise mechanism of their reinforcement is at best incompletely understood at present. In order to understand it at a fundamental level, and ultimately control it in practice, it is essential to determine the impact of interactions between filler particles and polymer matrix on the nanocomposite microstructure and its macroscopic dynamic mechanical properties. To this end, our collaborators at the University of Amsterdam performed experiments on two model systems, and we performed molecular-dynamics simulations, aiming to determine to what extent widely used shear-distortion models of the reinforcement are applicable, as well as the role played by molecular interactions on the enhancement of the mechanical properties. In both experiments and simulations a linear dependence of the reinforcement on the inverse radius of the nanoparticles was obtained. Deformation simulations of a linearly increasing strain showed an overall increase of 50% in the linear modulus when fillers were added to the polymer matrix, regardless of the use of direct interactions among the nanoparticles. Furthermore, the use of attractive nanoparticle interactions resulted in a higher matrix densification at the interfaces and to a sharp increase in the reinforcement.*

∗The contents of this chapter have been published in: *Macromolecules*, **2016**, *49* (18), 7077–7087.

5.1 Introduction

Adding fillers such as silica or carbon black particles to a polymeric matrix leads to a nanocomposite material with improved but also complex behavior drastically different from that of the pure polymer material. Rigid particles can act as stress concentrators owing to their elastic properties differing from those of the polymer matrix [**1**]. As a consequence, the linear storage modulus at low strain amplitudes can be greatly increased by the addition of a volume fraction of fillers φ_f. This is the so-called reinforcement [**2-9**], defined as $R = G(\varphi_f)/G(0) - 1$, with G being the shear modulus. On the other hand, at a higher (though still a relatively low) strain magnitude, the filled material displays a drop in the elastic modulus by about one order of magnitude; this is the so-called Payne effect [**10-17**]. In this study we focus our attention on the reinforcement mechanisms, by performing computer simulations as well as experiments, both of which are detailed below.

The reinforcement is not a new issue, and has been already extensively tested experimentally, analytically, and computationally [**18-20**]. The microstructure of the material, the polymer's segmental mobility [**21, 22**], as well as the chemistry-specific polymer-filler interactions, are all considered to be key factors affecting the reinforcement. The first mechanical model of reinforcement was proposed by Einstein and Smallwood [**23**]. Their model is valid in the dilute regime where particles do not interact with each other. The volume fraction of fillers, φ_f, continued to be the only parameter of the mechanical models created subsequently, such as the Mori-Tanaka model [**23, 24**] or the Christensen-Lo model [**25-27**]. However, a recent experimental study [**2**] demonstrated that the reinforcement cannot be accounted for only by the filler volume fraction when the particles interact through the matrix. In this study, the filler particle radius was introduced as another key parameter for the reinforcement of composite materials. Another recent experimental study [**28**] revealed how the interaction of polyethylene-glycol matrices with particles depends on the choice of the end groups of the polymer. It was also concluded that mean-field approaches are not sufficient to describe the systems.

Beyond the sole effect of the filler volume fraction, a wide range of experimental, theoretical, and simulation studies have thus far yielded two different opinions in regards to the molecular origins of the mechanical reinforcement in polymer nanocomposites: one attributes the excess reinforcement exclusively to nanoparticle aggregation or clustering, whereas the other attributes it to the formation of an interphase between the nanoparticles (NPs) and the bulk polymer. Seemingly, at high particle loadings reinforcement occurs due to particle jamming, whereas at low particle loadings it is the filler-polymer reinforcing network that mainly contributes to the reinforcement [**29**]. An extensive molecular-dynamics (MD) study of amorphous polymers filled with solid NPs [**30**] led to the conclusion that the balance of these two contributions depends strongly on the filler-polymer interaction energy and range, as well as the dispersion and volume fraction of the filler particles.

With the present study we aim to offer evidence of the shortcomings of the standard mechanical models used for predicting the reinforcement of polymer nanocomposites. In addition to the experiments, performed by our collaborators of the University of Amsterdam (UvA), we perform coarse-grained molecular-dynamics simulations of filled polymers, aiming to unravel the microscopic causes of the experimental observations.

5.2 Experimental Materials and Methods

5.2.1 Model systems

Rheological measurements on two types of systems were performed by our collaborators at UvA. They have been included in the present chapter so as to better illustrate similarities and differences among the experimental and simulation results. The first was Styrene Butadiene Rubber (SBR), an industrial rubber filled with NPs of precipitated silica, similar to what is used for tires. The second model system was a polyvinyl alcohol (PVA) gel filled with micron-sized glass beads. Contrary to filled rubbers, which have a very complicated microstructure [**1**], this model PVA-gel system was filled with monodisperse glass beads that do not aggregate.

5.2.2 Materials

The SBR, provided by Michelin ® (Molecular weight M_w=140 kDa vulcanized), was non-vulcanized and filled with nanoparticles of precipitated silica (Zeosil 1165 MP, Rhodia®) with an average aggregate radius of 15nm, which formed agglomerates of radius 34μm – 140μm. For the polymer gel, PVA was provided as a powder by Acros Organics (hydrolyzed at 99-100% and a molecular weight of 86 kDa). The powder was dissolved (4% wt.) in distilled water by mixing with a stirring bar at a temperature of 95°C for 3 hours. The borate was obtained by dissolving sodium tetraborate (provided by Sigma Aldrich) in distilled water using the same procedure of dissolving as with PVA. The gel was finally formed by mixing 2g of solution of borate with 8g of solution of PVA. The glass beads were provided by Swarco and had average radii of 34, 75 and 140 microns. With the rheometer gap being 2.5mm, the radius-to-gap ratio was approximately 75 for the smallest particles and 20 for the largest particles.

5.2.3 Rheological measurements

Oscillatory measurements were carried out with an Anton Paar Physica MCR 300 rheometer mounted with a plate/plate geometry. For the filled rubber system the diameter of the geometry was 5mm and the samples were disks with a thickness about 2.5mm stuck on each side with a Loctite glue [**31**]. For the experiments with the model PVA system the geometry was also plate-plate but a diameter of 25mm was used, and both of the surfaces were rough so as to avoid any wall slip.

5.3 Simulation Models and Methods

We performed constant temperature – constant pressure (NPT) coarse-grained molecular-dynamics simulations of non-entangled polymer chains. The representation of real polymer molecules by the bead–spring chain model used in this study is justified on nanometer length scales where different polymer molecules have been shown to behave similarly [**32**]. Two different simulation models were used. The first type of simulations was performed on a particulate model of nanocomposites in which the polymer matrix was filled with nanoparticles (NPs) of a size comparable to that of the polymer chains (Chapter 2, Fig. 2.5) in which each NP consisted of a specific number of beads.

For the second type of simulations, we note that due to restrictions in computational power, the size of the NPs in the simulations of the particulate systems was modest in comparison to the size of the filler agglomerates of the experimental samples [**2**]. Therefore, the large size of the experimental agglomerates was approximated in the simulations by using a film model in which the polymer matrix was confined between two solid walls (Chapter 2, Fig. 2.3). Each solid wall was used as a representation of the surface of an agglomerate with a radius that was orders of magnitude larger than the size of the polymer chains (see the Experimental data above). Indeed, it has been demonstrated that the thermophysical properties of polymer nanocomposites are quantitatively equivalent to the well-documented case of planar polymer films [**1**]. Notably, the change in the glass-transition temperature with decreasing inter-particle spacing for the nanocomposites was found quantitatively equivalent to the corresponding thin film data. Therefore, polymer films confined between solid walls may, in specific cases, be employed as simplified models of particulate systems, for they allow the study of one of the reinforcement mechanisms in isolation (since confinement effects are the single cause of the reinforcement). Previous studies [**2-4**] have shown that, in films capped between two attractive solid surfaces, with decreasing film thickness the dynamics of the confined polymer become slower in comparison to the dynamics of the pure polymer.

All simulations were performed using the LAMMPS MD software package [**34**]. The polymer phase was identical in both models and consisted of 100 linear polymer chains of 50 monomers each. Periodic boundary conditions were always implemented on all three dimensions of the simulation box. As a consequence of the coarse-grained nature of the models, only length scales larger than the typical Kuhn length values of polymer chains could be probed; in general a value close to 1 nm or larger may be assumed [**35**].

The Lennard-Jones (LJ) units of measurement are used throughout the text, *i.e.*, m is the unit of mass, ε is the unit of energy, σ is the unit of length, and $\tau = \sigma\sqrt{m/\varepsilon}$ is the unit of time. Newton's equations of motion were integrated using the velocity-Verlet algorithm with a time step of $\delta t = 0.005\tau$. The values of the LJ parameters were chosen in accordance to previous studies of similar model systems [**37**]. Interactions between non-bonded beads were modeled with a modified LJ 12-6 potential.

$$U_{nb}(r) = 4\varepsilon\left[\left(\frac{\sigma}{r}\right)^{12} - \left(\frac{\sigma}{r}\right)^{6}\right] + S_f(r)\ ;\ r < r_{cut}^{out} \tag{5.1}$$

The term $S_f(r)$ is a switching function that smoothly ramps the energy to zero from $r_{cut}^{in} = 2.5\sigma$ to $r_{cut}^{out} = 3.5\sigma$ [**37**]. The walls and the NPs consisted of smaller beads that were bound together by strongly attractive LJ interactions. The LJ parameters for the monomer beads were $\sigma_{\mathrm{m}} = \sigma$, $\varepsilon_{\mathrm{mm}} = \varepsilon$, $m_{\mathrm{m}} = m$, for both the film and the particulate models. In the films, the LJ parameters for the beads comprising the walls were $\sigma_{\mathrm{ww}} = 0.85\sigma$ and $\varepsilon_{\mathrm{ww}} = 50\varepsilon$. The LJ parameter ε between monomer- and wall-beads was set equal to $\varepsilon_{\mathrm{wm}} = 2\varepsilon$. In the particulate systems, the diameter of the filler beads comprising the NPs was equal to the diameter of the monomer beads, $\sigma_{\mathrm{ff}} = \sigma_{\mathrm{mm}}$. The LJ parameters for the filler beads belonging to the same NP were set equal to $\varepsilon_{\mathrm{ff}} = 50\varepsilon$ so as the NP to retain its consistency during the simulations. For the interaction among different NPs, we distinguished two cases by performing the same set of simulations with attractive NP-NP interactions (setting $\varepsilon_{\mathrm{NP\text{-}NP}} = \varepsilon$) as well as with short-range repulsive NP-NP interactions (using only the repulsive part of the LJ potential function). Our reasoning for the latter case was that, since the thickness of each film was larger than r_{cut}^{out} , the walls were not interacting directly with each other. This absence of *direct* interactions among the two walls of the films was reproduced in the particulate systems by using only the repulsive part of the LJ potential for the interactions among NPs. The aggregation of the NPs in the particulate systems was avoided by setting the interaction strength among filler beads and monomer beads equal to $\varepsilon_{fm} = 2\varepsilon$, which was the same value as the one used in the simulations of the film model for the interaction among monomer beads and wall beads. The parameters of the potential function for each system are presented in Table 5.1.

Table 5.1: Energy parameter values of the LJ potential function among the various types of beads comprising the simulated systems.

Parameter [ε]	**Description**	**Film model**	**Particulate model**
$\varepsilon_{\mathrm{mm}}$	monomer – monomer	1	1
$\varepsilon_{\mathrm{wm}}$	wall – monomer	2	-
$\varepsilon_{\mathrm{fm}}$	filler – filler (same NP)	-	50
$\varepsilon_{\mathrm{NP\text{-}NP}}$	filler – filler (distinct NP)	-	{0, 2}

Covalently bonded beads interacted through a combination of an attractive Finite-Extensible-Nonlinear-Elastic (FENE) potential, and a repulsive and truncated LJ 12-6 potential [**34**]:

$$U_{bn}(r) = -0.5k_{\mathrm{FENE}}r_{max}^{2}\ln\left[1-\left(\frac{r}{r_{max}}\right)^{2}\right] + 4\varepsilon\left[\left(\frac{\sigma}{r}\right)^{12} - \left(\frac{\sigma}{r}\right)^{6}\right] + \varepsilon \quad (5.2)$$

The parameters k_{FENE} and $r_{\max}$ denote the stiffness and the maximum elongation of the spring, respectively; ε is the LJ energy parameter, and σ the collision diameter of the interacting pair of beads. The stiffness and maximum elongation of the bonded potential were set equal to $k_{\mathrm{FENE}} = 30\ \varepsilon/\sigma^2$ and $r_{\max} = 1.5\sigma$ respectively. The LJ parameters ε and σ had the same values as their non-bonded counterparts (this particular choice of bonded and non-bonded interactions has been shown to prevent unphysical chain crossings [**38**]).

Two types of wall structures were used in the film model: crystalline and rough [**2**]. Each crystalline wall consisted of three layers of equally sized non-bonded beads arranged in a hexagonal closed packed (HCP) regular lattice. The walls were periodically infinite along their lateral dimensions, and confined the polymer along the perpendicular direction. We used three layers — which along with their periodic images amounted to six layers for each of the two walls — to avoid spurious interactions among the polymer chains and their periodic images. The thickness of the six crystalline layers of each wall was about 4.64σ, and did not change upon deformation. To create the rough walls, we deleted half of the beads in the two internal surfaces (those that were in contact with the polymer). The removal of the beads resulted in a roughness of 0.7σ, since the diameter of the spheres comprising the walls was $\sigma_{ss} = 0.85\sigma$ and the distance between two vertical layers in an HCP crystalline solid $l_z = \sigma_{ss}\sqrt{6}/3$. Three different values of film thickness were employed: as shown in Figure 2, at a fixed temperature of $T = 0.6\ \varepsilon/k_{\mathrm{B}}$ and isotropic pressure $P = 0\ \varepsilon/\sigma^3$, the thickness of each film with crystalline walls was approximately 18.0σ (designated as 'thick film'), 9.8σ ('thin film'), and 4.0σ ('ultrathin film'), which respectively corresponded to 5.2, 2.8, and 1.2 times larger than the average radius of gyration of the chains in the pure polymer matrix. Films with a different thickness had different lateral dimensions so that they would have the same film-averaged density at the same fixed temperature and pressure. Due to the crystallinity of the walls the lateral dimensions of each film were only approximately equal, though in all cases the difference was smaller than 0.5σ.

Table 5.2: Number of filler beads comprising the nanoparticles, and their equivalent radius.[a]

System	Number of beads in NP	Radius of NP
1	1000	6.5
2	500	5
3	250	4
4	125	3.25

[a] The gyration radius of the polymer chains was $R_g = 3.6\sigma$ and their end-to-end distance $R_{ee} = 8.9\sigma$.

To create the particulate systems, the box containing the equilibrated pure polymer was expanded so that the density would be low enough so that the NPs would not overlap with the polymer chains after their placement inside the simulation box. Each NP consisted of a specified number of beads, which were placed randomly inside a sphere of predefined radius. Three different filler volume fractions were employed: 9%, 16.7%, and 28.5%, and their average diameter extended from 6.5 to 13σ, with σ denoting the diameter of a monomer bead. For a detailed explanation of the composition of each simulated particulate system, please refer to Table 5.2 and 5.3.

Table 5.3: Number and radius of the NPs for each simulated particulate system.

Filler volume fraction (%)	Number of NPs	Radius of NP [σ]
9.00	1 2 4	5 4 3.25
16.7	1 2 4 8	6.5 5 4 3.25
28.5	2 4 8 16	6.5 5 4 3.25

We allowed the systems to equilibrate under NPT conditions at $T = 0.6\varepsilon/k_B$ and $P = 0\varepsilon/\sigma^3$. At these specific conditions all simulated systems were above their glass-transition temperature [**33**]. The glass-transition temperature of the films with crystalline walls is displayed in table 5.4 (for a graphical representation of the calculated values of the T_g, please refer to Chapter 4).

Previous simulations [**34**] have shown that the segmental dynamics of polymer films with rough walls are not noticeably different from those in films with crystalline walls. Consequently, we expect the glass-transition temperature to not be noticeably affected by the structure of the walls since the glass-transition temperature and the segmental dynamics are strongly correlated [**33**]. During both the equilibration and production runs we used the values recommended in the LAMMPS manual for the thermostat and barostat parameters, *i.e.*, temperature and pressure were allowed to relax to the specified average value over a time interval of 0.5τ and 5.0τ, respectively [**34**].

Table 5.4: Glass-transition temperature (T_g) of the films with crystalline walls [**33**].

System	Thickness [σ]	T_g [ε/k_B]
Bulk polymer	-	0.381
Thick film	18.8	0.426
Thin film	10.1	0.438
Ultrathin film	4.3	0.577

5.4 Results

5.4.1 Experimental results from UvA

Rheological oscillatory measurements were performed by our collaborators at the UvA so as to provide insightful connections among the reinforcement measured in experiments and the one calculated from simulations.

For a given volume fraction of fillers φ_f the reinforcement is defined as the ratio of the modulus G of the filled material at low strain amplitude and the modulus of the bare material:

$$R = \frac{G(\varphi_f)}{G(\varphi_f = 0)} - 1 \tag{5.3}$$

The radius of the silica aggregates contained in the SBR rubber, as quantified using TEM measurements, was found to be independent of the volume fraction of fillers.

To account for the dependence of the reinforcement on the filler volume fraction, three different shear-distortion models were considered, which are commonly used for the calculation of $R(\varphi_f)$ in composite materials [**18**]:

$$R = \begin{cases} 2.5\varphi_f & Einstein-Smallwood \\ 2.5\varphi_f + 14.1\varphi_f^2 & Guth \\ \left[1 + 1.25\varphi_f/\left(1 - 1.35\varphi_f\right)\right]^2 - 1 & Eilers \end{cases} \tag{5.4}$$

The Einstein-Smallwood formula [**5**] is applicable to materials with a low volume fraction of fillers, in which the reinforcement originates from a linear superposition of the individual particle contributions (the ‘dilute regime’). Guth’s model [**8**] additionally takes into account contributions from the interactions among neighboring particles. The Eilers equation was derived from the Einstein-Smallwood formula, and takes into account the large increase in the reinforcement that is commonly detected in composites with a very high volume fraction of fillers (for which the filler particles attain a close-packed structure).

Fig. 5.3 shows the dependence of the reinforcement on the volume fraction of fillers for two systems: the PVA filled with glass beads, and the non-vulcanized filled SBR (see Experimental Materials and Methods section). For small volume fractions $\left(\varphi_f < 0.25\right)$ the reinforcement of the filled PVA followed the Einstein-Smallwood equation, which indicates that the system was highly diluted. However, for $\varphi_f > 0.2$ (Figure 3a, inset) the reinforcement became dependent on the radius of the nanoparticles and deviated from the Einstein-Smallwood equation. For $0.2 < \varphi_f < 0.25$, a transitory regime was observed in which the Guth and Eilers models could be fitted to the data but were unable to describe the dependence of the reinforcement on the filler radius. For $\varphi_f > 0.25$, none of the formulas was able to accurately predict the reinforcement of the model system.

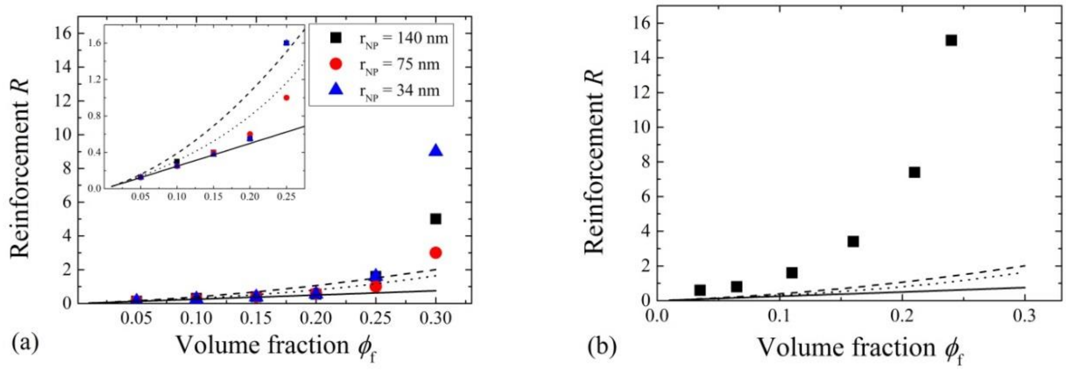

Figure 5.3: Reinforcement versus volume fraction for (a) the model system (PVA filled with glass beads of three different average radii r_{NP}), and (b) the non-vulcanized filled rubber (SBR filled with nanoparticles of precipitated silica of an average radius of 15nm), obtained from rheological experiments. The solid, dotted, and dashed lines correspond to the predictions of Einstein-Smallwood, Eilers, and Guth models, Eq. 5.4, respectively.

The dilute regime observed in the model system was not observed in the filled SBR rubber, in which the shear-distortion models could not predict the reinforcement even at very low values of the volume fraction of fillers (Fig. 5.3b). It is evident that the reinforcement of the filled rubber cannot be reliably predicted by taking into account only the filler volume fraction, even when the latter is very small. This conclusion holds even if we use a mean field approximation in which the particles are surrounded by occluded polymer layers, which leads to a larger effective volume fraction of the filler particles [**2**]. Our hypothesis is that since the rubber matrix was three orders of magnitude harder as compared to the PVA gel, interactions among fillers in the former material become effective at lower volume fractions, and therefore should not be neglected.

Clearly, a model for composite reinforcement that accounts not only for the filler volume fraction but also for the size of the NPs, as well as their interactions, is therefore needed. Recently, Mermet-Guyennet *et al.* [**10**] demonstrated experimentally that the reinforcement cannot be accounted for by the sole consideration of the filler volume fraction (as shown in Figure 3a) or the surface per unit volume of the fillers ($3\varphi_f / r_{NP}$, where r_{NP} is the radius of the filler particles), as shown in Fig. 5.4. Instead, the scaling law

$$R = 2.5\varphi_f + \frac{a}{r_{NP}} = 2.5\varphi_f + \frac{C\varphi_f^3}{r_{NP}} \tag{5.5}$$

should be employed, in which the nonlinear term represents the matrix-mediated filler interactions. The length scale C corresponds to the maximum distance among the center-of-mass of the NPs before the vanishing of the interaction term, and depends on the ratio of the moduli of the filler versus that of the polymer matrix [**2**].

Figure 5.4a illustrates the dependence of the reinforcement on the glassy beads radius r_{NP} of the model system for a given volume fraction of fillers. Evidently, under constant filler volume fraction the reinforcement exhibited a linear dependence on the inverse radius of the glassy beads. Further, a higher reinforcement was obtained with the usage of smaller beads or a higher filler volume fraction. The obtained data for $R - 2.5\varphi_f$ were plotted as a function of φ_f^3/r_{NP} and were linearly fitted, resulting in the value $C = 30mm$ (Fig. 5.4b).

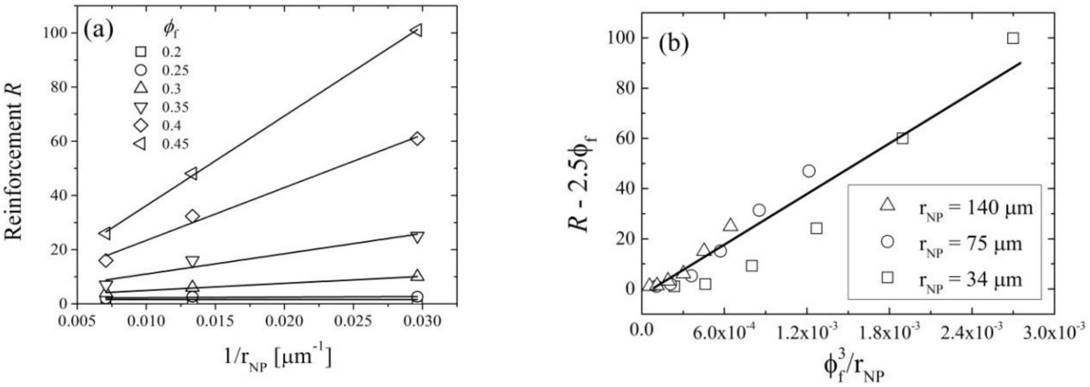

Figure 5.4: Dependence of the reinforcement of the PVA model system on the filler radius and volume fraction: (a) Reinforcement versus the inverse of the filler bead radius $1/r_{NP}$ for various values of the filler volume fraction. A larger reinforcement corresponds to a larger volume fraction of fillers which varied from $\varphi_f = 0.20$ to $\varphi_f = 0.45$ with a step change of 0.05. The slope α of the solid lines depends on φ_f. (b) Dependence of $R - 2.5\varphi_f$ on φ_f^3/r_{NP}. The solid line was obtained from a linear fit of all the data points, and corresponds to the parameter C in Eq. 5.

To summarize, the experiments on the two model systems unequivocally demonstrate that it is not possible to predict the reinforcement by taking into account only the volume fraction of the fillers or their specific surface. The results from the PVA model system, where the filler radius could be varied, followed the scaling law (Eq. 5.5) introduced in Ref. [10] that reflects the role of interactions among the filler particles. We hypothesize that the data on the SBR model system confirms the crucial role of the interactions, because the rubber matrix, which is much harder than the PVA matrix, could effectively amplify these interactions, thus explaining why the experimental data on the SBR reinforcement deviate even more from the predictions of Eq. 5.4. The data indicate that the polymer matrix-mediated interactions dramatically affect the reinforcement, and should be considered in any model of reinforcement in nanocomposite polymeric systems.

5.4.2 Simulations

5.4.2.1 The simulated reinforcement of the film and particulate models

We performed coarse-grained molecular-dynamics simulations of non-entangled polymer chains, as outlined in the Simulation Models and Methods section. Both film and particulate models were uniaxially and affinely elongated under a constant strain rate $\dot{\gamma} = 0.001\tau^{-1}$ (*i.e.* the length of the box-sides laterally to the direction of deformation was kept constant) at $T = 0.6\varepsilon/k_B$ (which was above the glass transition temperature of the simulated systems), and $P = 0\varepsilon/\sigma^3$. The deformation was imposed on the whole system as if it were homogeneous (i.e., without the walls in the film model, which, due to the strongly attractive LJ interactions among the beads comprising the walls, did not deform during the elongation simulations). We extracted the linear modulus by fitting the stress-strain curves in the regime of linear stress response (strain < 1%) where any change in density may safely be neglected. Stress-strain curves obtained from the elongation simulations are shown in Fig. 5.5 for both the film and the particulate model.

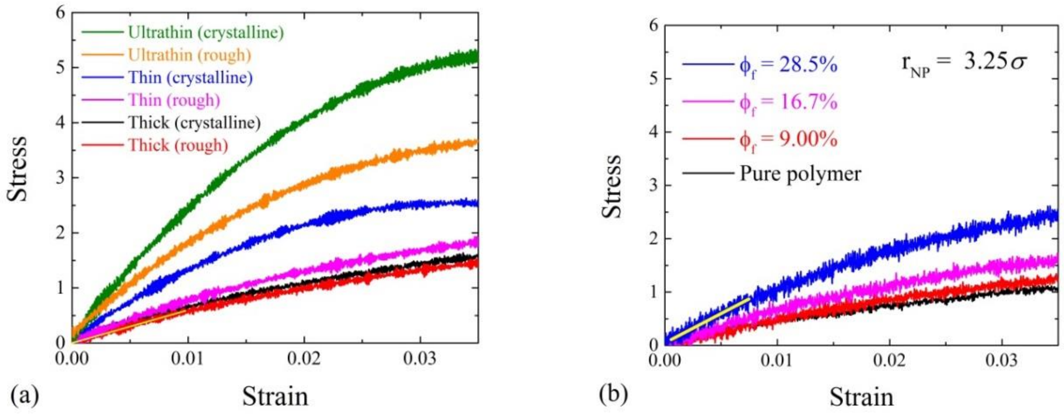

Figure 5.5: Stress-strain plots of (a) the film model for all different film thicknesses, and (b) the particulate model of the nanocomposite for three different volume fractions and a single filler radius $r_{NP} = 3.25\sigma$ as well as for the non-filled, pure polymer matrix. The yellow, solid line illustrates the strain interval used for the extraction of the linear modulus of the systems. All simulations were performed at $T = 0.6\varepsilon/k_B$ and $P = 0\varepsilon/\sigma^3$.

In Fig. 5.6a we present the simulation results for the reinforcement of the films as a function of film thickness. Two competitive effects can be observed: On the one hand, a higher degree of confinement (*i.e.*, smaller film thickness) resulted in a larger reinforcement. On the other hand, the wall roughness decreased the reinforcement. A plausible explanation for the former effect is the following. A strong wall attraction may result in the development of a glassy layer in the polymer-wall interface ($0 < z < 1.3\sigma$) [**21**], the width of which is independent of the film thickness. Therefore, in a thinner film the ‘glassy’ polymer will occupy a larger volume fraction of the film, thus resulting in greatly increased film-averaged relaxation times. Hence, under constant temperature, thinner films will lie closer to their glass-transition temperature, and therefore their response to the applied strain will be more pronounced. Further implications concerning the effect of polymer glassification on the reinforcement are considered in the Discussion section of this Chapter.

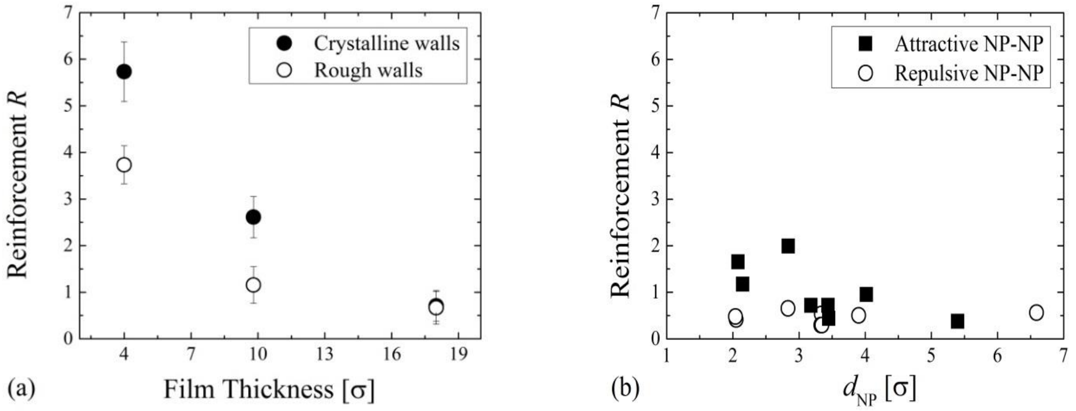

Figure 5.6: (a) Reinforcement of the films versus the film thickness. (b) Reinforcement of the particulate systems versus the average distance between the surfaces of the NPs for attractive and repulsive NP-NP interactions. No significant reinforcement was observed in the particulate systems with repulsive NP-NP interactions.

Furthermore, the reinforcement decreased when the crystalline walls were replaced by rough ones. Presumably, this was the result of a less-packed interfacial polymer layer near the rough walls than near the crystalline ones, which effectively decreased the attraction of the monomers to the walls. Consequently, the glassy layer mentioned above was less important in the films with rough walls than in those with crystalline ones, which was the cause of the smaller reinforcement in the films with rough rather than crystalline walls.

In our simulations of particulate systems, the reinforcement was strongly influenced by the type of NP-NP interaction, as we show in Fig. 5.6b. The average NP-NP distance was the same for both types of interactions. The calculated reinforcement was relatively small $(R \leq 1)$ for the systems with short-range repulsive NP-NP interactions, as well as for the systems with attractive NP-NP interactions when the surface-distance d_{NP} between the NPs was larger than the LJ cut-off distance r_{cut}^{out} (in which case the system was effectively reduced to a system with short-range repulsive NP-NP interactions). On the other hand, for $\varphi_f = 28.5\%$, $\varepsilon_{NP-NP} = \varepsilon$, and $d_{NP} < 3.5\sigma\ (= r_{cut}^{out})$ the calculated reinforcement increased abruptly with a decreasing particle distance, and attained a maximum value of $R \approx 2$.

With the exception of the ultrathin film, which showed a pronounced reinforcement, the values of *R* obtained in films and particulate systems were comparable. We consider this as an indication that confinement effects in the polymer films are replaced by another reinforcing factor in the particulate systems; for the latter the effective confinement of the polymer chains is significantly smaller than in the film model, due to the curvature of the spheroidal NPs. As will be discussed later, this could correspond to the development of a filler network in particulate systems with attractive NP-NP interactions at relatively small NP distances.

5.4.2.2 Comparison of the reinforcement among the particulate simulation model and the experimental samples

In qualitative agreement with the reinforcement models of Eq. 5.4, as well as with the experimental results (see Figure 3), a higher volume fraction of fillers resulted in a larger reinforcement of the simulated particulate systems, as shown in Fig. 5.7. The same conclusion can be obtained from the film model, if we regard the *thinner* film as a simplified model of a particulate system with a *higher* volume fraction of fillers, since a smaller film thickness also led to a higher reinforcement. In the absence of attractive NP-NP interactions the Einstein formula, Eq. 5.4, predicted the reinforcement of the particulate systems with the highest accuracy. On the other hand, the calculated reinforcement values of the particulate systems with attractive NP-NP interactions was in between the values predicted by the Guth and Eilers formulae.

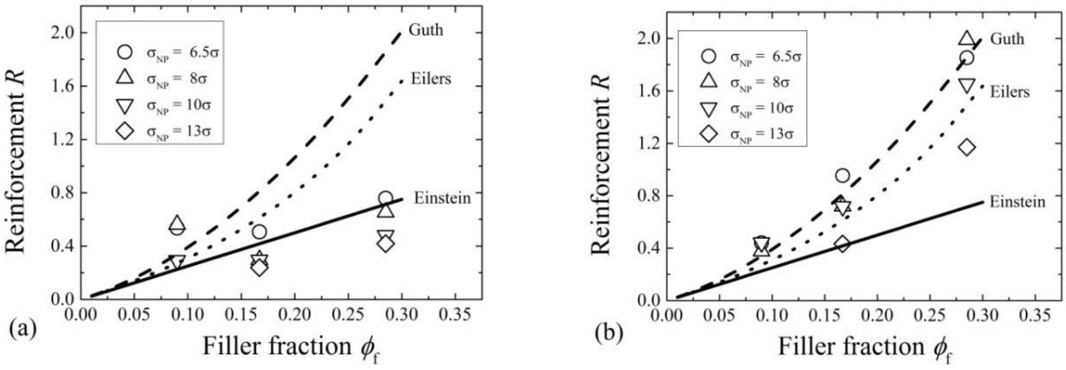

Figure 5.7: Reinforcement versus filler volume fraction φ_f computed from simulations with repulsive (a) and attractive (b) NP-NP interactions. Data are shown for various values of the NP

diameter σ_{NP}. The lines offer a comparison to three different reinforcement models (Eq. 5.4) that are frequently used for the calculation of the reinforcement in polymer composites. The width of the error bars was smaller than that the data points.

The agreement with the theoretical predictions (Fig 5.7a) at rather high volume fractions (above 25%) is surprising because the Einstein model was developed for infinitely dilute systems where the motion of a single particle is not disturbed by the other particles; this cannot be the case at such high filler concentrations. The agreement with Guth and Eilers formulae (Fig. 5.7b) is surprising because in these models the hydrodynamic interactions between many particles are taken into account, but in the present simulations the systems are different only by the additional Lennard-Jones, excluded-volume interactions. It is not immediately obvious why the hydrodynamics is also changing in this case. Both observations were unexpected, and are being considered in the Discussion and Conclusions section.

The reinforcement of the particulate simulation model roughly increased linearly with the inverse radius of the NPs (Figure 5.8), which is similar to the experimental curves of Fig. 5.4. The slope of R as a function of $1/r_{\mathrm{NP}}$ depended on the filler volume fraction. Note that at a constant volume fraction of fillers, a smaller NP radius resulted in a larger filler-polymer interfacial area, a smaller average NP-NP distance (not shown), and a larger reinforcement (for both attractive and repulsive NP-NP interactions). In the particulate systems with attractive NP-NP interactions, a smaller NP radius resulted in a noticeably higher value of R only for volume fractions $\varphi_f > 9\%$. For $\varphi_f = 9\%$ the radius of the NPs did not affect the reinforcement, whereas for $\varphi_f = 28.5\%$ the reinforcement attained a maximum value when $r_{NP} \approx 4\sigma$, Fig. 5.8. In the particulate systems with repulsive NP-NP interactions, the effect of the NP size on R was relatively weak but still present.

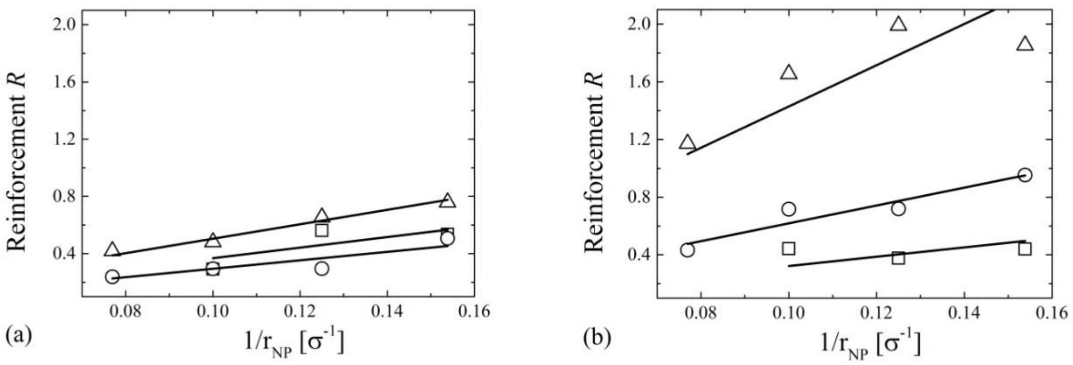

Figure 5.8: Reinforcement as a function of the inverse radius of the nanoparticles r_{NP}, for systems with repulsive (a) and attractive (b) NP-NP interactions. The square, circular, and triangular data points denote the reinforcement of the particulate system with φ_f = 9.0, 16.7, and 28.5%, respectively. This figure can be compared with the experimental results shown in Figure 5.4a. The width of the error bars was smaller than that the data points.

When $R - 2.5\varphi_f$ was plotted as a function of φ_f^3/r_{NP} (Fig. 5.9) a linear scaling was obtained for both types of NP-NP interactions that were used in the simulations of the particulate systems. Furthermore, for each type of NP-NP interactions, the data for all values of the NP diameter fell roughly onto a single straight line, in accordance with the experimental results, although the quality of the linear fitting was lower in the simulations than in the experiments. The slope of the straight line is connected to the experimental factor C (from Eq. 5.5) which has been interpreted as the maximum distance between the centers-of-mass of the filler particles beyond which they no longer interact [**2**]. The factor C was calculated equal to 70 and 480σ for the simulations of the particulate systems with and without attractive NP-NP interactions, respectively. As mentioned previously, the *average* NP-NP distance did not depend on the NP-NP interactions.

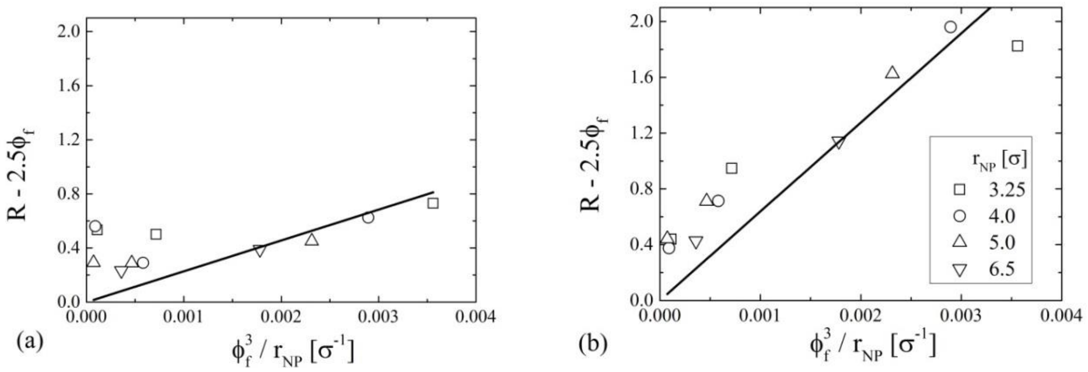

Figure 5.9: Reinforcement of the simulated particulate systems, arising from coupled hydrodynamic interactions and surface effects, versus φ_f^3/r_{NP} for repulsive (a) and attractive (b) NP-NP interactions. For each type of the NP-NP interaction, the data for all values of the NP radius r_{NP} roughly fell onto a single straight line. This figure can be compared with the experimental results shown in Fig. 5.4b. The width of the error bars was smaller than that of the data points.

5.4.2.3 Microscopic mechanisms of reinforcement

Our simulation results show that the reinforcement is enhanced by a higher filler volume fraction φ_f, a smaller particle radius r_{NP}, and by employing attractive rather than repulsive NP-NP interactions. We will now focus on the microscopic structure and dynamics of the simulated particulate systems. To this end we calculated the monomer distribution between the NPs (Fig. 5.10) and the average mean-square displacements (MSD) of the monomer beads g_0^m (Fig. 5.11).

The first observation was that the width of the polymer-filler interface $(\approx 1\sigma)$ was unaffected by the volume fraction and the radius of the NPs as well as the NP-NP interaction energy (not shown). Furthermore, a higher concentration of monomer beads was observed at the polymer-filler interface than in the rest of the system. We also found that the density of the monomer beads in the polymer-filler interface was higher for a higher φ_f (Fig. 5.10a) or a smaller r_{NP} (Fig. 5.10b), whereas it was not affected by the NP-NP interaction strength, although the latter appeared to be one of the main causes of the reinforcement (note that, for the polymer films, the film thickness – or equivalently, the NP-NP distance — has been reported to have no effect on the number of interfacial monomers [**33**]).

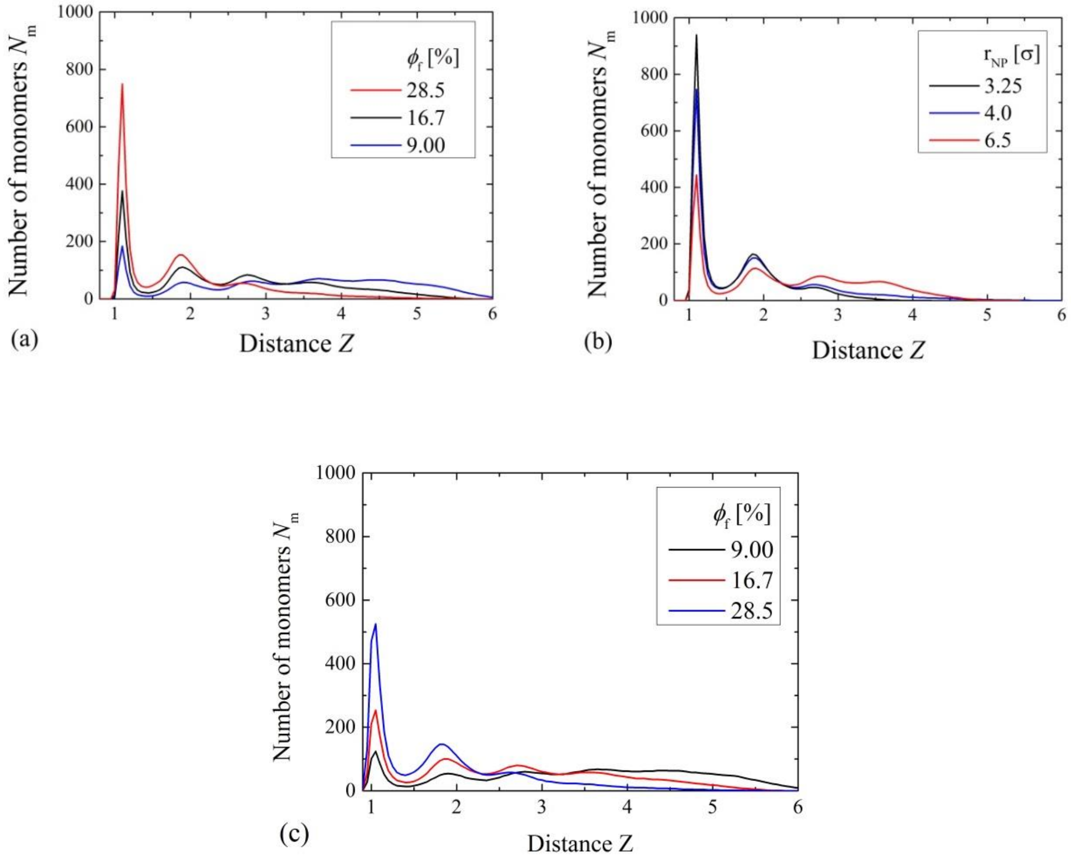

Figure 5.10: Number of monomer beads as a function of the distance from the surface of a NP, with $\varepsilon_{mf} = 2\varepsilon$ and $\varepsilon_{mm} = 2\varepsilon$. Results are shown for (a) $r_{NP} = 4\sigma$ and different values of the filler volume fraction, and (b) $\varphi_f = 28.5\%$ and two different values of the NP radius. The density profiles overlapped for the systems with attractive and repulsive NP-NP interactions. (c) The same as Figure 10a but with $\varepsilon_{mf} = \varepsilon_{mm} = \varepsilon$.

A higher concentration of monomers at the NPs' surfaces when the filler volume fraction was increased under constant NP radius was because a higher filler volume fraction resulted in a larger monomer-filler contact area. On the other hand, it was not clear whether the high monomer concentration at the filler-matrix interfacial area was induced by the monomer-filler interaction strength. In order to assert to which degree the monomer concentration was induced by the strong monomer-filler LJ attraction ($\varepsilon_{mf} = 2\varepsilon$ $\varepsilon_{mm} = 2\varepsilon$), we recalculated the density profiles by performing simulations with $\varepsilon_{\mathrm{mf}} = \varepsilon_{\mathrm{mm}} = \varepsilon$ (Fig. 5.10c).

It is evident that, even when $\varepsilon_{\mathrm{mf}} = \varepsilon_{\mathrm{mm}}$, the monomers still displayed a tendency to concentrate near the surfaces of the NPs, although to a lesser degree than in the case in which $\varepsilon_{\mathrm{mf}} = 2\varepsilon_{\mathrm{mm}}$. When the monomer-filler interaction strength was reduced by half, the number of monomers that were concentrated at the interfaces was approximately reduced by half as well. Therefore, we may conclude that strong monomer-filler interactions enhance monomer concentration near the NPs, but they are not the main cause of it. Previously published results [**21, 33**] from simulations of polymer films with solid walls, as the ones studied in the current manuscript, have revealed a higher monomer density near the walls than in the middle of the film, even when the wall-polymer and monomer-monomer interaction strengths were equal. This ordering effect is induced by to the fact that the wall, and equivalently the surface of the NP, is more structured than the bulk polymer, hence this difference in ordering between the wall and the bulk induces a "gradient of ordering" along the direction perpendicular to the wall (or equivalently along the radial direction, in the particulate simulations).

Shifting the focus to the simulation results on the dynamics, we found that the MSD of the chains' center-of-mass was only weakly affected by the NP-NP interaction strength and the filler volume fraction (not shown). On the other hand, the MSD of the monomer beads g_0^m increased slower with time for a higher φ_f or a smaller r_{NP} (Fig. 5.11a). Systems with attractive NP-NP interactions displayed a slower increase in g_0^m than systems with repulsive interactions (Fig. 5.11b), whereas the NP-NP interactions did not affect the density profiles (Fig. 5.10). This indicates that the interactions among the NPs affect the properties of the polymer matrix by inducing dynamical changes without altering its structure. Further, the effect of r_{NP} on R was weaker than the effect of the NP-NP interactions: for instance, Figure 11b illustrates that the reinforcement of systems with a larger r_{NP} and attractive NP-NP interactions was higher than the reinforcement of systems with a smaller r_{NP} and repulsive interactions.

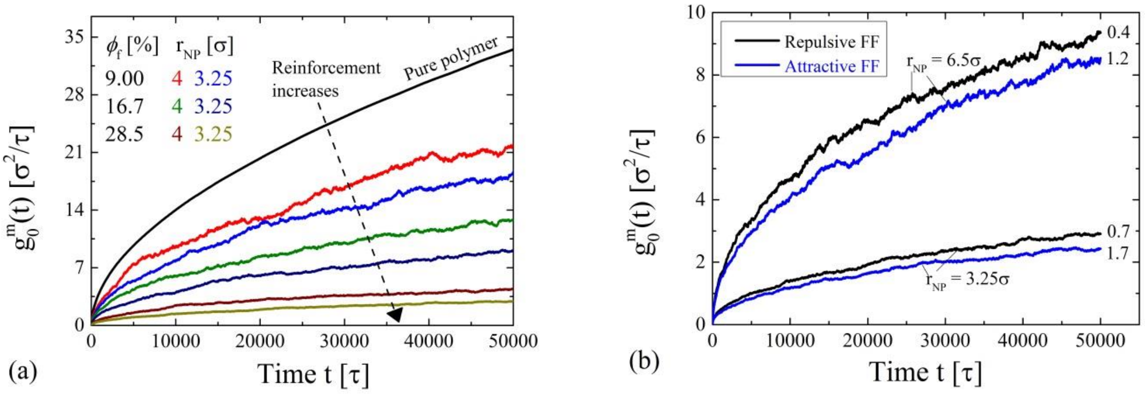

Figure 5.11: (a) Dependence of the mean-square displacement of the monomer beads g_0^mon φ_f and r_{NP} for the particulate systems with repulsive NP-NP interactions. The r_{NP} colors in the legend correspond to the colors of the curves. A monotonic dependence of *R* on g_0^m was also observed in the particulate systems with attractive NP-NP interactions. (b) Dependence of g_0^m on the NP-NP interactions and r_{NP}. The numbers on the right end of each curve denote the calculated values of the reinforcement for each simulated system.

5.5 Discussion and Conclusions

It is well established that the addition of particles in a polymer matrix results in the reinforcement of its mechanical properties. However, many questions concerning the origin of the reinforcement still remain unanswered. In this study we present a comparison between experimental and simulation results for the reinforcement of filled polymer systems.

The experimental results indicate that the polymer mediated NP-NP interactions are affected by the filler-matrix interactions, because the latter affects the properties of the matrix. In the experimental model (PVA gel) system we can safely assume that direct NP-NP interactions are absent because of the large size of the fillers, whereas in the filled rubber, which matrix had a higher modulus, it is possible that the hardness of the matrix may have induced strong NP-NP interactions already at small filler volume fractions. The detection of a radius-dependent reinforcement in the experimental model system for $\varphi_f < 25\%$ demonstrates that the presence of nanometric glassy layers is inessential in regards to the reinforcement of nanoparticle-filled materials, because their presence should make no difference in systems with fillers as large as those employed in the PVA model system.

For the experimental model system, the hydrodynamic models employed in this study were able to provide with an accurate prediction of the mechanical reinforcement only for low filler volume fractions; for larger filler volume fractions we observed that the reinforcement was dependent on the filler radius. However, in the filled SBR rubber, the hydrodynamic models could not predict the experimental data even at very low values of the filler volume fraction. A formula was derived in a previous study [**2**], which was also used here, that takes additionally into account the dependence of the reinforcement on the radius of the filler particles.

The Einstein model of the reinforcement was able to predict accurately the reinforcement in both the experiments of the PVA model system (only for $\varphi_f < 20\%$) as well as the simulations with no direct NP-NP interactions (for $\varphi_f < 30\%$). The validity of the model for such high values of the filler volume fraction was unexpected. We attribute the agreement among the obtained data and the Einstein model's predictions to the fact that the simulation conditions were more complex than those of the simplified assumptions of the Einstein model. The derivation of the Einstein model is based on the Navier-Stokes hydrodynamic equations which are solved so as to determine the flow pattern around a single spherical particle [**39**]. The main assumptions of the model are the following: the inertia of the translational and rotational motion of the particle is ignored; the motion of the particle is determined solely by the stress to which the particle is exposed at its surface (therefore, its motion does not depend on the state of other particles in the system); and lastly, the velocity field of the deformation vanishes at the surface of the particle (no-slip boundary conditions) [**40**]. These assumptions, however, might break-down in our MD simulations. The simulated NPs were non-spherical, they possessed internal structure, and as will be shown in Chapter 6, an increasing value of strain led to increasing (i.e., non-zero) velocities of the polymer segments lying at the surfaces of the NPs.

For larger volume fractions of fillers, the reinforcement of the experimental samples and the simulations of the particulate systems with direct NP-NP interactions followed the reinforcement models of Guth and Eilers, which take into account the matrix-mediated hydrodynamic interactions among the NPs. Peculiarly, it seems that direct NP-NP interactions enhanced the hydrodynamic interactions among the NPs. This can be explained by that the attractive LJ interactions affected the structure of the polymer matrix, which surely affected the hydrodynamics of the systems. To affirm that that was indeed the case, we compared the radius of gyration of the chains as a function of strain, among the particulate systems with and without attractive NP-NP interactions, Fig. 5.12. It is clear that the polymer matrix responded differently to the applied strain, depending on whether the NPs were interacting directly through LJ forces or not: at the same strain value, the component of the radius of gyration of the polymer chains along the strain direction was larger in the particulate systems with repulsive LJ interactions than in those with attractive ones. As it seems then, the NP-NP interactions played indeed a “modifying” role: the polymer matrices in the particulate systems with and without direct NP-NP interactions exhibited different structural properties, and therefore it highly probable that they induced different hydrodynamic interactions.

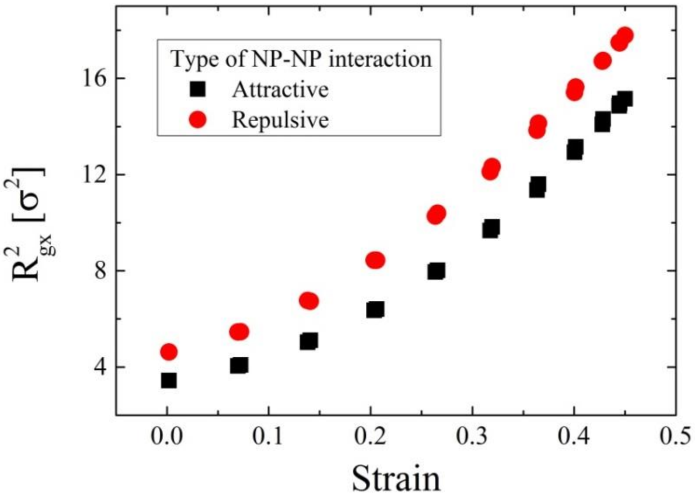

Figure 5.12: Squared radius of gyration of the polymer chains as a function of the instantaneous strain, as calculated by the simulations of the particulate systems with and without attractive NP-NP interactions.

The observed similarities among experimental and simulation results allows for a more detailed study of the causes of the reinforcement observed in the experimental samples through the study of the structural and dynamical properties of the simulated systems. According to the first interpretation of the reinforcement [**41, 42**], it is the interactions among the NPs (e.g., van der Waals forces [**44**]) that produce the main part of the reinforcement. In this context, when fillers were added to the polymer matrix, we observed an increase of about 50% in the linear modulus (regardless of the NP-NP interaction type). In the present simulation results, systems with attractive NP-NP interactions displayed a reinforcement which increased sharply once the average distance between the surfaces of the NPs became smaller than the LJ cut-off radius (or, in other words, when the NPs began to interact directly with each other and, on average, retained their interaction throughout the duration of the simulations). This observation may serve as a further indication that, for high enough volume fractions of fillers, the development of an attractive filler network, resisting deformation, could indeed be an important source of reinforcement. Further simulations, though, utilizing a larger number of filler particles, are needed so as to study the sensitivity of the reinforcement on the cut-off radius of the NP-NP interaction potential function. On the other hand, at low filler volume fractions the reinforcement of the particulate systems was similar, whether attractive or repulsive NP-NP interactions were used, presumably because indirect (i.e., matrix-mediated) hydrodynamic interactions among the NPs are more relevant to the reinforcement than direct NP-NP interactions.

A higher filler volume fraction led to a smaller NP-NP distance, and to the densification of the monomer beads at the filler-polymer interfaces. As a consequence, a higher filler fraction resulted in a more confined polymer matrix and a slower diffusion of the monomer beads. The type of NP-NP interactions, though, did not affect the structural properties of the particulate systems. We conclude that the increased densification of the polymer matrix close to the attractive surfaces of the NPs (owing to an increased volume fraction of fillers) was the main cause for the small increase of the reinforcement observed in the simulations with repulsive NP-NP interactions, as well as in systems with attractive NP-NP interactions and an average NP-NP surface-distance d_{NP} larger than the LJ cut-off radius r_{cut}^{out}. For $d_{NP} < r_{cut}^{out}$ additional contributions (ostensibly stemming from the development of an energetic NP network) induced a further increase of the reinforcement in the systems with attractive NP-NP interactions. Additionally, NP-NP interactions were evidently more important in increasing the reinforcement than the use of a smaller particle size.

Comparing the two simulation models (films and particulates) we saw that the structural properties of the polymer matrix displayed strong similarities among the film and particulate models, which can be clearly seen in the comparison among the polymer density profiles observed in the particulate model (Fig. 5.10) and from the density profiles of the polymer films, which are discussed in Chapter 4 [**21, 33**]. Also, with the exception of the strongly confined, ultrathin films, the values of the reinforcement in both models were comparable. This allows us to conclude that the confinement effects are replaced by another reinforcing factor in the particulate systems with smaller curvature of the NPs. This additional mechanism seemed to be the direct, attractive interactions among the NPs, which was absent in the film model where the walls did not interact with each other.

Overall it seems that the simulations were in a different parameter regime than the experiments: presumably, in the simulations, a much weaker coupling among the polymer matrix and the NPs was present at the interfaces, which led to less densification of the polymer matrix as compared to that of the experiments. Follow-up work should therefore include a broader variation of the filler-matrix interaction strength. The filler particles were much smaller than in the experiments in which aggregation of the particles took place. Therefore, filler surface effects in simulations are quite important: for the same filler volume fraction, the small particle radius in the simulations as compared to the radius of the experimental agglomerates, leads to an extremely large overall interfacial area.

References

[1] Tjong, S. C., *Mater. Sci. Eng. R-Rep.* **2006**, *53*, 73–197.

[2] Mermet-Guyennet, M. R. B.; de Castro, J. G.; Varol, H. S.; Habibi, M.; Hosseinkhani, B.; Martzel, N.; Sprik, R.; Denn, M. M.; Zaccone, A.; Parekh, S. H.; Bonn, D., *Polymer* **2015**, *73*, 170-173.

[3] Masnada, E.; Merabia, S.; Couty, M.; Barrat, J-L., *Soft Matter* **2013**, *9* (44), 10532-10544.

[4] Sosson, F.; Belec, L.; Chailan, J.-F.; Carriere, P.; Crespy, A., *J. Appl. Polym. Sci.* **2010**, *117* (5), 2715-2723.

[5] Smallwood, H. M., *J. Appl. Phys.* **1944**, *15* (11), 758-766.

[6] Heinrich, G.; Klüppel, M.; Vilgis, T. A., *Curr. Opin. Solid St. M.* **2002**, *6* (3), 195-203.

[7] Rattanasom, N.; Saowapark, T.; Deeprasertkul, C., *Polym. Test.* **2007**, *26* (3), 369-377.

[8] Guth, E., *Rubber Chem. Technol.* **1945**, *18* (3), 596-604.

[9] Suzuki, N.; Kiba, S.; Kamachi, Y.; Miyamoto, N.; Yamauchi, Y., *Phys. Chem. Chem. Phys.* **2012**, *14* (10), 3400-3407.

[10] Mermet-Guyennet, M.; de Castro, J. G.; Habibi, M.; Martzel, N.; Denn, M.; Bonn, D., *J. Rheo*l. **2015**, *59* (1), 21-32.

[11] Payne, A. R., *J. Appl. Polym. Sci.* **1962**, *6* (21), 368-372

[12] Payne, A. R., *J. Appl. Polym. Sci.* **1962**, *6* (19), 57-63.

[13] Staniewicz L., Vaudey T., Degrandcourt C., Couty M., Gaboriaud F., Midgley P., *Sci. Rep.* **2014**, *4*, 7389.

[14] Garnier, P.; Le Cam, J. B.; Grédiac, M., *Mech. Mater.* **2013**, *56*, 84-94.

[15] Merabia, S.; Sotta, P.; Long, D. R. A, *Macromolecules* **2008**, *41* (21), 8252-8266.

[16] Cassagnau, P., *Polymer* **2003**, *44* (8), 2455-2462.

[17] Ramier, J.; Gauthier, C.; Chazeau, L.; Stelandre, L.; Guy, L., *J. Polym. Sci. Part B Polym. Phys.* **2007**, *45* (3), 286-298.

[18] de Castro, J. G. *Understanding the viscoelastic behavior of silica filled rubber*, PhD Thesis, Universiteit van Amsterdam: Amsterdam, 2014.

[19] Zeng, Q.; Yu, A.; Lu, M., *Prog. Polym. Sci.* **2008**, *33* (2), 191-269.

[20] Allegra, G.; Raos, G.; Vacatello, M., *Prog. Polym. Sci.* **2008**, *33*, 683.

[21] Batistakis, C.; Lyulin, A. V.; M. A. J. Michels, M. A. J., *Macromolecules* **2012**, 45, 7282.

[22] Hattemer, G. D.; Arya, G., *Macromolecules* **2015**, *48*, 1240.

[23] Mori, T.; Tanaka, K., *Acta Metallurgica* **1973**, *21* (5), 571-574.

[24] Benveniste, Y., *Mech. Mater.* **1987**, *6* (2), 147-157.

[25] Raos, G., *Macromol. Theory Simul.* **2003**, *12* (1), 17-23.

[26] Christensen, R. M., *J. Mech. Phys. Solids* **1990**, *38* (3), 379-404.

[27] Christensen, R. M.; Lo, K. H., *J. Mech. Phys. Solids* **1979**, *27* (4), 315-330.

[28] Glomann, T.; Schneider, G. J.; Allgaier, J.; Radulescu, A.; Lohstroh, W,; Farago, B.; Richter, D., *Phys. Rev. Lett.* **2013**, *110* (17), 178001.

[29] Pryamitsyn V.; Ganesan V., *Macromolecules* **2006**, 39, 844–56.

[30] Sen S.; Thomin J. D.; Kumar S. K.; Keblinski P., *Macromolecules* **2007**, 40, 4059–67.

[31] Montes, H.; Lequeux, F.; Berriot, J., *Macromolecules* **2003**, *36* (21), 8107-8118.

[32] Kröger, M., *Phys. Rep.* **2004**, *390*, 453-551

[33] Davris, T.; Lyulin, A. V., *J. Chem. Phys* **2015**, *143*, 074906.

[34] Plimpton, S., *J. Comput. Phys*. **1995**, *117*, 1.

[35] Mark, J. E. *Physical Properties of Polymers Handbook*, 2nd ed., Springer: New York, 2007.

[36] Batistakis, C.; Michels, M. A. J.; Lyulin A. V., *Macromolecules* **2014**, *47*, 4690 – 4703.

[37] Fryer, D. S.; Peters, R. D.; Kim, E. J.; Tomaszewski, J. E.; de Pablo J. J.; Nealey, P. F.; White, C.C.; Wu W. L., *Macromolecules* **2001**, *34*, 5627.

[38] Kremer, K.; Grest G. S., *J Chem Phys* **1990**, *92*, 5057.

[39] Toda K., Furuse H., *J. Biosci. BioEng*. **2006**, *102* (6), 524.

[40] Landau L. D., Lifshitz E. M., *Mechanics*; Butterworth-Heinemann: Oxford 1976

[41] Kraus, G. *Reinforcement of elastomers*, Interscience Publishers: New York, 1965.

[42] Medalia, A. I., *Rubber Chem Technol* **1978**; *51*, 437–523.

[43] Israelachvili, J. N. *Intermolecular and surface forces*, Academic Press: New York, 1991.

Chapter 6

Molecular Mechanisms of the Payne Effect in Filled Elastomers: Insights from Computer Modeling

Abstract

Coarse-grained molecular-dynamics computer simulations of a model polymer nanocomposite comprised of monodisperse non-entangled, non-crosslinked polymer chains, and filler nanoparticles, have been carried out under oscillatory shear of varying strain amplitude and frequency of oscillations. Our studies showed a strong decrease of the storage modulus with increasing strain amplitude, which was accompanied by a maximum in the loss modulus (the so-called Payne effect): the onset of the softening was observed in the linear regime of deformation, at a strain value of about 1%. Moreover, the dependence of G' on the instantaneous strain exhibited both softening and hardening regimes, in agreement with recently reported LAOS experiments. The simulations of the mean-squared displacements of the polymer segments suggest that the observed hardening was caused by the shear-induced decrease of the non-affine segmental diffusion of the monomers of the matrix where the filler particles acted as effective crosslinks. The strain softening with increasing strain amplitude is connected to the dynamic heterogeneity of the polymer matrix.

∗The contents of this chapter are being prepared for publication.

6.1 Introduction

Innovations in the production and usage of polymer-based composites has led to a significant global growth of their application areas, such as in automotive, rail, naval, transport, construction and infrastructure, defense and aerospace, medical and healthcare, electrical and electronics, telecommunication, as well as in other industries. [**1, 2**]. This growth has been driven by new methods of synthesis of polymers filled with inorganic materials which impart additional properties to them, the most important of which are the combination of light weight and high strength [**3**]. The market size of filled plastic materials could easily grow further, provided one can remediate the lack of understanding of reliable correlations between the microscopic structure and macroscopic properties of particle-filled polymer matrices, particularly under dynamical conditions. Such understanding can result in unique, new mechanical properties of these materials.

Polymer nanocomposites are just at their infancy of development, but offer huge potential for future applications and energy savings. The observation [**4-6**] that, other things being equal, the effectiveness of the filler increases with an increase in the surface-to-volume ratio has provided a large impetus to the shift from micro- to nano-sized particles. Therefore, polymer-based nanocomposites are considered an important branch of the emerging field of nanotechnology [**7**].

Rheological experiments [**8**] show that the mechanical reinforcement upon the addition of filler particles is primarily controlled by the inter-particle interactions mediated to some extent by the polymer matrix. The more specific role of the polymer matrix still remains unclear, in particular, the role or even the existence of the glassy adsorbed polymer layer surrounding the filler particles [**7, 9**].

Large amplitude oscillatory shear (LAOS) experiments have been performed recently by Mermet-Guyennet et al. [**10**]. They showed that although the overall rheology of particle-filled gels and polymers (melts and crosslinked networks) exhibited strain softening (i.e., Payne effect, [**11**]), within a single oscillatory cycle the systems exhibited strain hardening. Their conclusion was that the experimental deformation rate is the important time parameter of the problem, not an intrinsic time scale: the overall softening was a consequence of the molecular rearrangements due to the imposed deformation. This conclusion is in agreement with the reported strain-rate frequency superposition rheology results of Wyss et al. [**12**]. As the segmental relaxation seems to be responsible for the observed softening, it is important to clarify the details of the molecular rearrangements which lead to the Payne effect; in this respect, computer simulations look promising.

The key issue in understanding the molecular origin of the reinforcement and its dependence on the applied deformation and the Payne effect, which has so far remained unresolved, is the exact molecular mechanisms, at a nanometer scale, that induce changes in the properties of the polymer matrix (e.g. mechanical reinforcement). These mechanisms are crucial; understanding them would allow us to predict how the microstructure of a polymer nanocomposite affects its macroscopic properties and, therefore, to control the performance of polymer materials by adding rationally designed nanostructured fillers [**13**]. In order to reveal the mechanism, it is necessary to couple the interactions of different components of a composite at the molecular level with spatial structuring of filler nanoparticles in the polymer matrix at the mesoscale. In turn, the spatial structuring is affected by macroscopic flow patterns during processing. To deal with these phenomena, the computer simulation methods look rather perspective as they enable more precise prediction of the nanocomposite's macroscopic properties and performance in applications and, ultimately, allow in the future rational, molecular-level design of the nanocomposite. Such dynamic simulations on a coarse-grained level are carried out in the present chapter.

Since complex interactions between constituent phases at the atomic level ultimately manifest themselves in macroscopic properties, a large range of length and time scales must be, in principle, addressed in such simulations, and a combination of modelling techniques is therefore required to simulate meaningfully the bulk-level behavior of nanocomposites. Raos et al. [**14**] were among the first who studied the effect of the interactions between stiff colloidal filler particles and polymer networks by using large scale, coarse-grained Dissipative Particle Dynamics (DPD) simulations. However, the nonlinear viscoelastic results of their simulations were rather different from the experimentally observed Payne effect. The authors conclude that its origin is not entirely related to the particle-particle interactions. The reasons of the observed discrepancies could also be in the specificity of the soft DPD potentials used in these simulations. At the same time, recent DPD simulations of Gavrilov et al. [**15**] reproduced nicely the experimental reinforcement in elastomer nanocomposites.

In elastomer-based nanocomposites the filler nanoparticles play the role of the temporal crosslinks. The formation of the temporal networks and the role of the polymer nanoparticles interactions have been studied by Kutvonen et al. [**16, 17**] by coarse-grained molecular-dynamics (MD) simulations, where filler particles were represented as Lennard-Jones spheres. The authors found that the observed reinforcement is correlated with the minimization of the relative mobility of the filler particles with respect to the polymer segments. Definitely this conclusion should be checked and studied further for different, non-spherical filler shapes [**18**].

Various molecular mechanisms of the Payne effect and reinforcement for polymer nanocomposites filled with model nanofillers (mainly spherical) are studied by Chen et al., [**19**] and in a series of publications from the Liu and Lyulin groups [**20-22**]. The role of direct particle-particle interactions and of the segmental orientation at the particle–matrix interface was investigated. Still, questions remain about the dominant molecular mechanism, and the effects caused by more realistic shapes of the filler particles.

The main aim of this work has been to further elucidate, using molecular-dynamics simulations, the seeming contradiction between usual non-linear viscoelastic measurements and the Lissajous analysis of the same material, by investigating microscopic phenomena which cannot be readily probed in experiments. Namely, from a strain sweep the material appears to display strain softening, whereas the Lissajous analysis of a single oscillation cycle indicates that the material displays strain hardening. We subsequently focus on understanding the strain softening, notably the observation that the amplitude depends on the deformation rate. Finally, we probed the effect of using attractive or repulsive interactions among the nanoparticles on the mechanical properties and the underlying microscopic dynamics of the simulated nanocomposite.

The simulated models and the algorithms are explained in the next section. The results of the shear deformation are summarized in Section 3. The chapter is finalized with our conclusions.

6.2 Models and Methods

Filled rubbers, among numerous other materials, exhibit strain softening at high strain amplitudes during a strain sweep in oscillatory rheology: the modulus decreases with increasing strain amplitude. On the other hand, when the nonlinear elastic response is analyzed within a single oscillation cycle (i.e., at constant strain amplitude) these systems are often reported to exhibit strain hardening. We attempted to reproduce that behavior by performing MD simulations of a polymer matrix filled with nanoparticles (NPs). Although the polymer matrix of the simulated systems consisted of non-crosslinked and non-entangled chains, the relatively fast deformation rates accessible to MD simulations allow the system to display rubber-like properties. Therefore, the results of our simulations can be applicable to rubbers. The particulate system with $\varphi_f = 28.5\%$ and $\mathrm{r_{NP}} = 4\sigma$ (Chapter 5) was subjected to sinusoidal deformation, and the resulting mechanical response was calculated as a function of the deformation time. But whereas the previous chapter was dedicated to the study of the reinforcement at low values of the strain amplitude, in this Chapter the simulated system is exposed to sinusoidal deformation so as to study the drop of the reinforcement as the strain amplitude is increased.

The value of the strain amplitude was varied from 0.01 to 0.45 which lies beyond the linear stress-strain regime. Moreover, to perform the non-equilibrium simulations, the SLLOD equations of motion were used [**23**]. At each strain amplitude, $\gamma_{\max}$, ten oscillatory cycles were performed. Each cycle lasted for 1,000τ, thus resulting in a total oscillation time of 10,000τ for a given $\gamma_{\max}$. The time frequency of oscillations was $v = 0.001\tau^{-1}$ which corresponds to an angular frequency of $\omega = 0.0063\tau^{-1}$, unless otherwise mentioned (Table 6.1). Lastly, attractive NP-NP interactions were always used for the nanocomposite, with the exception of section 6.5 where both attractive and repulsive NP-NP interactions are used so as to study the effect of the NP-NP interactions on the Payne effect.

Table 6.1: Values of the angular frequency, ω, and the ordinary frequency, v, which were used in the simulations.

v [τ^{-1}]	ω[rad τ^{-1}]
0.001	0.0063
0.005	0.0314
0.01	0.0628
0.05	0.3140
0.1	0.6280

6.3 Computing moduli using LAOS simulations

Polymer nanocomposites exhibit strain softening behavior among subsequent oscillation cycles of increasing strain amplitude [**11, 14**]. This is the so-called Payne effect, first discovered in the 1960’s. However, during a single oscillation cycle of constant strain amplitude, the same materials exhibit strain hardening at high values of strain. In the non-linear regime of stress response, though — where the Payne effect is observed — the definition of the moduli is not unique. Recent experiments have attempted to elucidate the seemingly paradoxical strain softening/hardening behavior [**10**] and concluded that the strain hardening observed in polymer nanocomposites is a local effect, and depends on the employed method of calculating the moduli. Here, we compared two methods of extracting the moduli of our simulated systems (*i.e.*, Eq. 6.1 and 6.4). The first is the usual non-linear viscoelastic measurement; it is based on the instantaneous stress response of the material (Eq. 6.1), and will be discussed forthwith. The second method is based on the analysis of Lissajous curves, *i.e.*, stress-strain plots, and will be discussed subsequently (Eq. 6.4).

The components of the complex modulus as calculated by a rheometer [10] — and in most cases by MD simulations as well [21, 22] — are extracted by fitting the instantaneous stress response to Eq. 6.1 (using n = 1, 3). We note that the terms G_1' and G' will be used interchangeably.

$$\sigma(t) = \gamma_{max} \sum_{n,odd} [G_n'(\omega, \gamma_{max}) \sin(n\omega t) + G''_n(\omega, \gamma_{max}) \cos(n\omega t)] \qquad (6.1)$$

The fitting procedure is illustrated in Fig. 6.1, where the instantaneous stress response of the composite system is depicted at γ_{max} = 0.02 and 0.45. As seen in Fig 6.1, the fluctuations in the calculated stress were more pronounced for smaller values of the strain amplitude (e.g., γ_{max} = 0.02) than for larger ones (e.g., γ_{max} = 0.45). Furthermore, the *Mullins effect* — a phenomenon commonly observed in filled elastomers, due to which the elastic modulus of the first cycle is higher than that in subsequent ones under cyclic deformation conditions — was not reproduced in the simulations: the stress response of the simulated nanocomposite was identical during all the oscillatory cycles. This implies an absence of irreversibly damaged covalent filler-matrix bonds in the simulated nanocomposite.

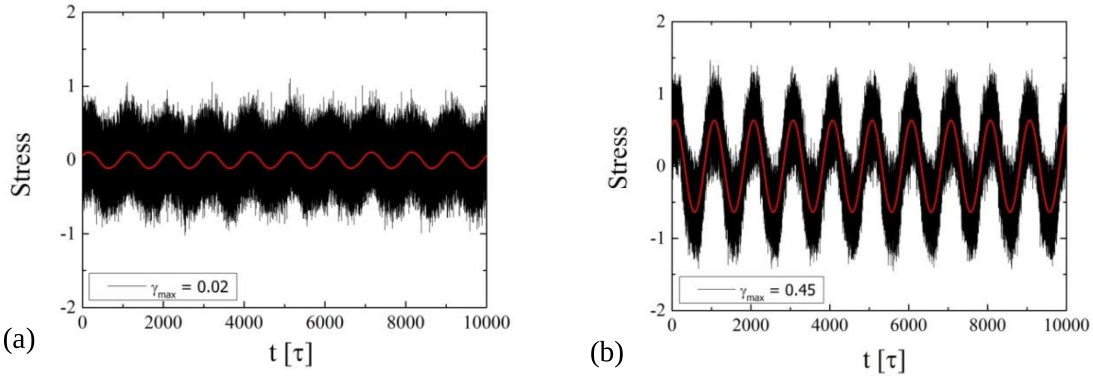

Figure 6.1: Stress versus time at $\gamma_{\max}$ = 0.02 and 0.45. The red lines are the fitting curves based on Eq. 6.3. At each strain amplitude, the instantaneous stress is depicted during all 10 oscillatory cycles.

Nevertheless, the *Payne effect* (the drop in G' with the accompanied maximum of G’’ with increasing strain amplitude) was indeed reproduced by using Eq. 6.1, at least qualitatively (Fig. 6.2a-b). Note that G' and G'' are identical to G_1' and G_1'' of Eq. 6.1.

According to the Lissajous curves of Figs. 6.2c-e, non-linear terms, *i.e.*, higher order harmonic contributions to the stress (G_3' and G_3''), should be taken into account when $\gamma_{\max}$ is relatively high, since the stress-strain curves were not perfect ellipsoids. Strangely, although higher harmonics should be zero at small strain amplitudes and increase with increasing strain amplitude, the opposite was produced by the usage of Eq. 6.1 (Fig. 6.3). To elucidate what seems to be a paradox, we attempted to compute the moduli using a different method.

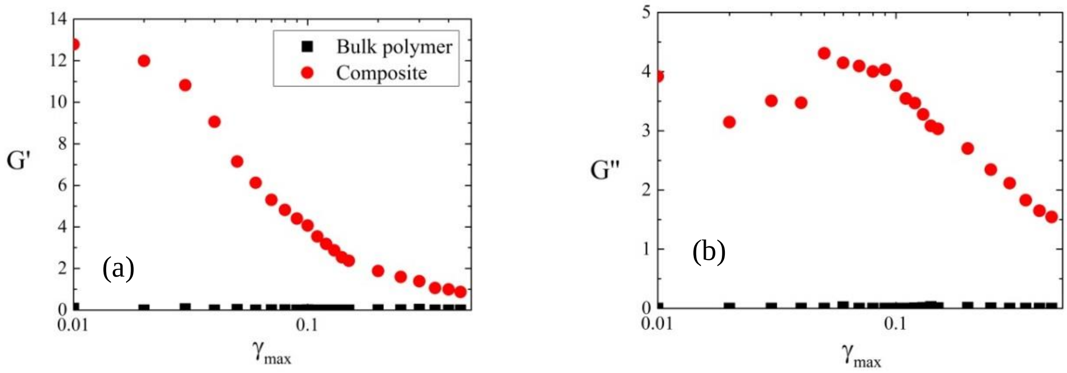

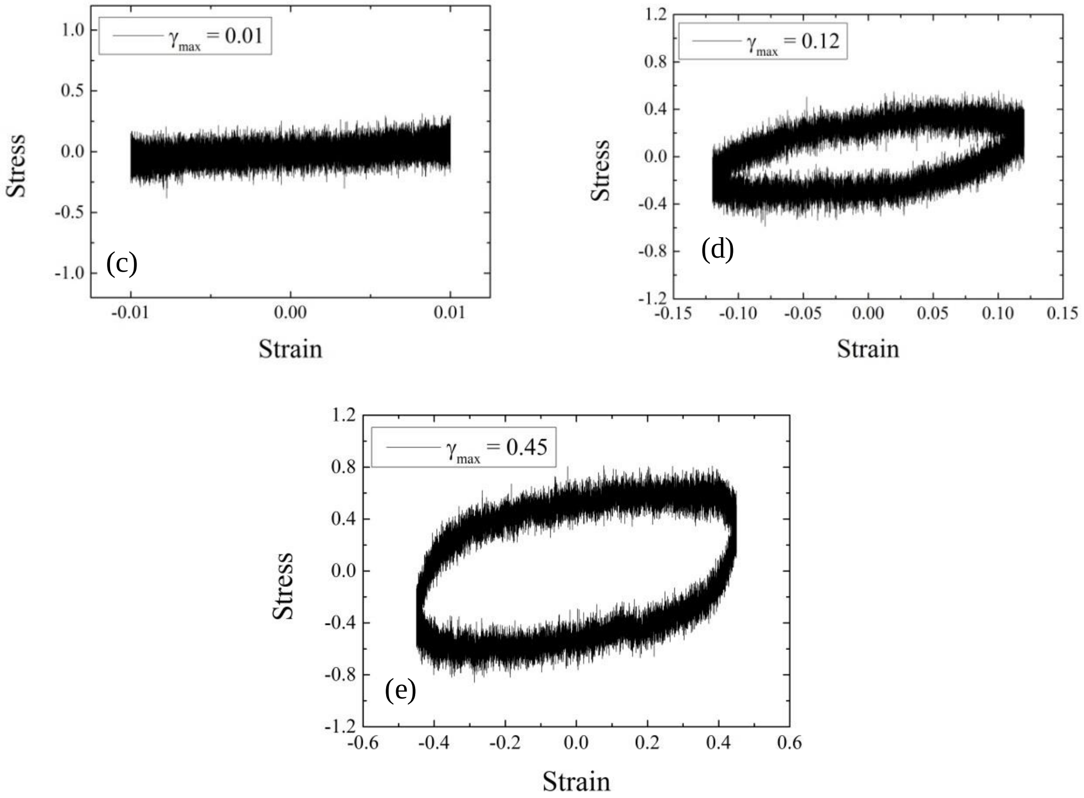

Figure 6.2: Elastic (a) and viscous (b) moduli versus strain amplitude γ_{max}. The moduli were extracted with the method described above. The c, d, and e panels depict the Lissajous curves for three values of the strain amplitude, i.e., γ_{max} = 0.01, 0.12, and 0.45.

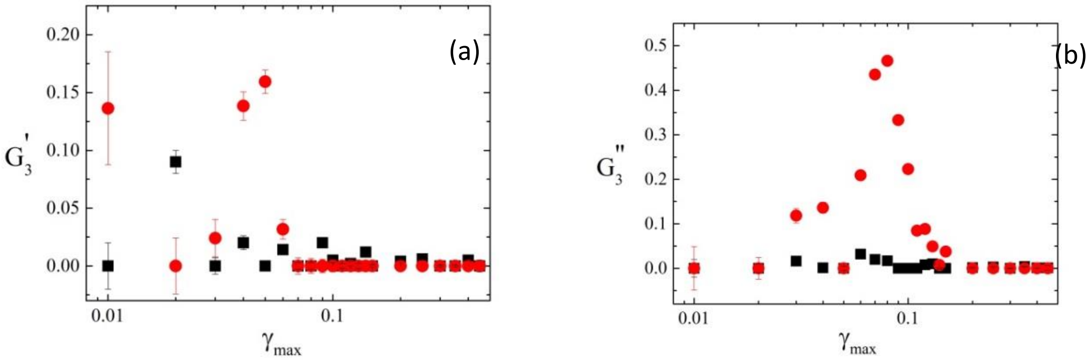

Figure 6.3: The 3rd elastic (a) and viscous (b) harmonic contributions to the stress versus the strain amplitude. The black and red data points correspond to the unfilled polymer and the nanocomposite, respectively.

In the regime of non-linear stress response, the moduli do not have a unique definition [**24**]. Two of the most commonly used definitions are depicted in Eq. 6.2 and 6.3.

$$G' = \frac{\omega}{\pi \gamma_{max}^2} \oint \sigma(t)\gamma(t)dt \tag{6.2}$$

$$G'_M = \left(\frac{d\sigma}{d\gamma}\right)_{\gamma=0} \tag{6.3}$$

Eq. 6.2 gives an elastic modulus as calculated by a rheometer's software (based on Eq. 6.1): the term G' in Eq. 6.2 is identical to the term G'_1 in Eq. 6.1. Eq. 6.3 gives an elastic modulus as the slope of the strain-strain curve at zero strain [**10**]. We plotted the stress-strain curves for the nanocomposite and the unfilled polymer (Fig. 6.4) by averaging the stress response over the ten oscillation cycles of constant strain amplitude, and extracted the terms G'_M and G'_3 by fitting the data of Fig. 6.4a to Eq. 6.4 (which can be derived from Eq. 6.1, taking into account the definition of G'_M from Eq. 6.3) [**10**].

$$\sigma_e(t) = G'_M\gamma + 4G'_3\frac{\gamma^3}{\gamma_{max}^2} \tag{6.4}$$

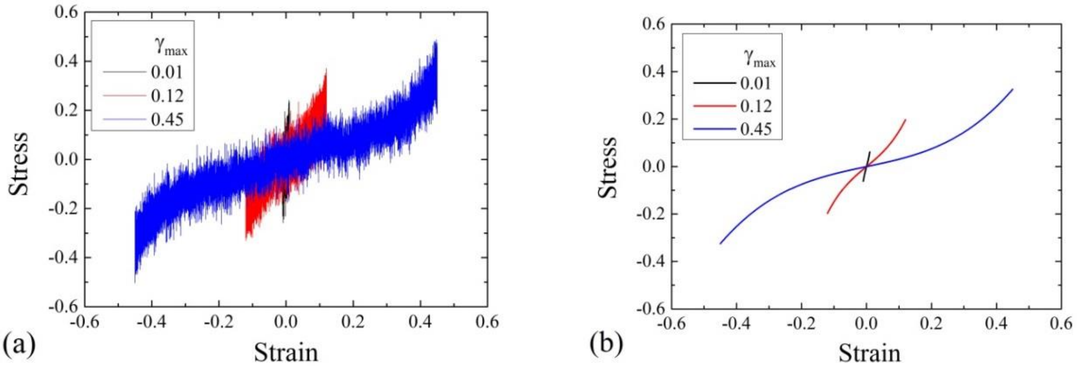

Figure 6.4: Elastic stress, σ_e, versus strain for different strain amplitudes (for the system with attractive LJ NP interactions). The two panels: (a) raw simulation data, (b) simulation data fitted to Eq. 6.4.

The term σ_e refers to the elastic stress which in the classical, linear viscoelastic regime can be obtained from the total stress $\sigma(t) = G'\gamma(t) + G''\gamma(t)/\omega = \sigma_e(t) + \sigma_v(t)$, where σ_v is the viscous stress. This separation of the total stress into elastic and viscous components can be generalized to the non-linear regime according to Eq. 6.5 [29].

$$\sigma(t) = \frac{\sigma(t) + \sigma(-t)}{2} + \frac{\sigma(t) - \sigma(-t)}{2} = \sigma_e(t) + \sigma_v(t) \tag{6.5}$$

The strain softening with increasing strain amplitude is clearly visible as the change in the slope at zero strain (*i.e.*, the decrease in G'_M with increasing strain amplitude). For large strain values, though, a slight upturn of the curves was observed. This upturn indicates a strain hardening response. Before discussing the strain hardening, though, we will first compare the values of the moduli we extracted by using equations 6.1 and 6.4. The results are depicted in Fig. 6.5.

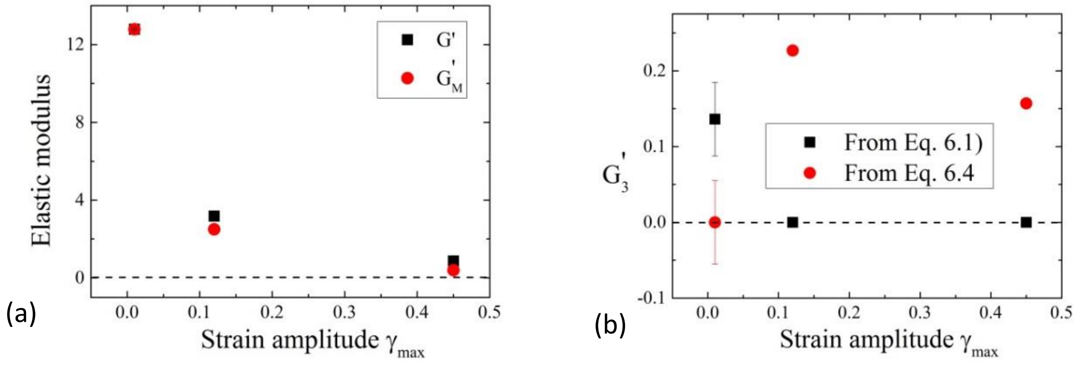

Figure 6.5: (a) Elastic moduli and (b) 3rd order elastic harmonic versus the strain amplitude. The G' was calculated by fitting the simulation data to equation 6.1, and the G'_M by fitting the data in Fig. 6.4a to equation 6.4. Equation 6.1 gives seemingly unphysical results for the 3rd order elastic harmonics. The problem was solved when Eq. 6.4 was used to extract the moduli.

Both equations produced similar values for the elastic modulus (*i.e.*, $G' \approx G'_M$). However, only Eq. 6.4 gave physically logical results for the higher harmonics, with G'_3 being equal to zero at the linear regime of stress response and increasing when strain-hardening was observed, as was expected. Therefore, Eq. 6.4 produced a more reliable prediction for the higher elastic harmonic contributions to the stress.

Turning our attention to the strain hardening that was observed at high values of the instantaneous strain, we will attempt to answer the following question: is the strain hardening an intrinsic property of the polymer matrix, or is it caused by the presence of the NPs? To provide with an answer, we plotted a normalized version of the stress-strain curves of Fig. 6.4 for the nanocomposite as well as for the unfilled polymer. Specifically, the elastic stress was normalized by the stress amplitude, $\sigma_{\max}$, and the strain was normalized by the strain amplitude, $\gamma_{\max}$ (Fig. 6.6).

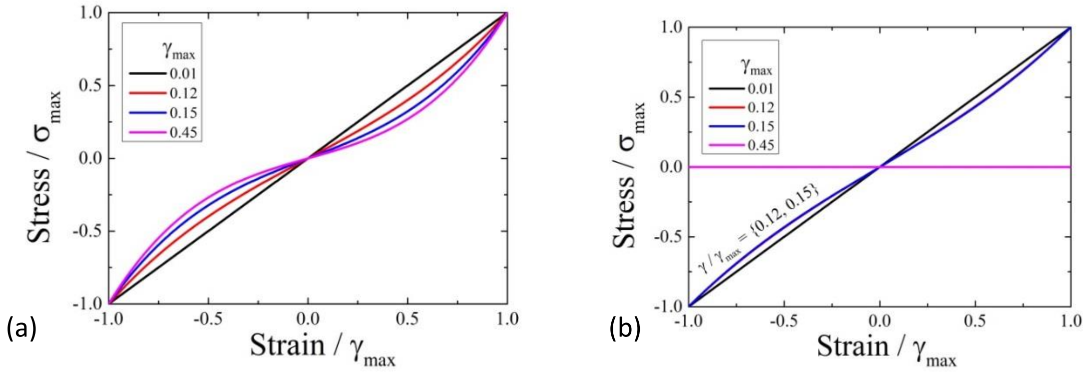

Figure 6.6: Elastic stress, σ_e, normalized by the stress amplitude, $\sigma_{\max}$, versus strain normalized by the strain amplitude, $\gamma_{\max}$, for (a) the nanocomposite and (b) the unfilled polymer. Each curve refers to a different value of the strain amplitude.

The strain hardening appeared at $\gamma_{\max} > 0.01$, in both the nanocomposite and the unfilled polymer. However, the unfilled polymer had surpassed its yield point at $\gamma_{\max} = 0.20$, whereupon the unfilled polymer exhibited liquid behavior, and the stress became independent of strain. At $\gamma_{\max} < 0.20$ both the composite and the unfilled matrix exhibited strain hardening. The hardening was more pronounced in the nanocomposite than in the unfilled polymer. Thus, we conclude that the strain hardening produced by the simulations was an intrinsic property of the matrix, but it was further enhanced by the presence of the NPs.

6.4 Microscopic mechanisms of the strain hardening

To elucidate the microscopic causes of the strain hardening observed at large strain values, we calculated the non-affine displacement (NAD) of the monomer beads for both the nanocomposite and the unfilled polymer. The calculations were based on Eq. 6.6.

$$g_0^a = \langle \left| \boldsymbol{r}_j(t) - \boldsymbol{r}_j(0) \right|^2 \rangle \tag{6.6}$$

The term $r_j(t)$ is the coordinate of bead j at time t, $r_j(0)$ the coordinate of the same bead at the initial time of the deformation, and a denotes the constituent of the system; i.e., $a = p$ for the monomer segments of the matrix, $a = P$ for the center-of-mass (COM) of the polymer chains, and $a = NP$ for the nanoparticles. While calculating the NAD we did not subtract the displacement of each constituent due to the convective velocities imposed on them by the deformation of the simulation box. In Fig. 6.7 the NAD of the monomer beads is depicted at $\gamma_{max} = 0.45$ for the nanocomposite (Fig. 6.7a) and for the unfilled polymer (Fig. 6.7b). Each data point in the graph denotes the NAD of the monomer beads between two consecutive strain values.

In the unfilled polymer, the NAD of the monomer beads was nearly unaffected by the imposed strain as well as by the strain amplitude (Fig. 6.7b). This seems to correspond well with the constant elastic modulus and the absence of a maximum point in the viscous modulus as the strain amplitude was increased, as depicted in Fig. 6.2a-b for the unfilled polymer. On the other hand, that was not the case for the NAD of the monomer beads in the nanocomposite. Under constant strain amplitude, the NAD of the monomer beads was higher during the eccentric (from γ = 0 to γ = γ_{max}) than the concentric (from γ = γ_{max} to γ = 0) contraction of the nanocomposite. Furthermore, as the strain increased from the unstrained state, the NAD of the monomer beads increased until the strain attained a value of about 0.15; a further increase of the strain led to the decrease of the NAD of the monomer beads. This was more prominent at the highest employed strain amplitude (γ_{max} = 0.45): at smaller values the resolution was too coarse to affirm whether the same behavior was also reproduced. Nevertheless, the same behavior was also observed for the NPs and for the COM of the polymer chains, with the only differences being a smaller displacement and worse statistical quality.

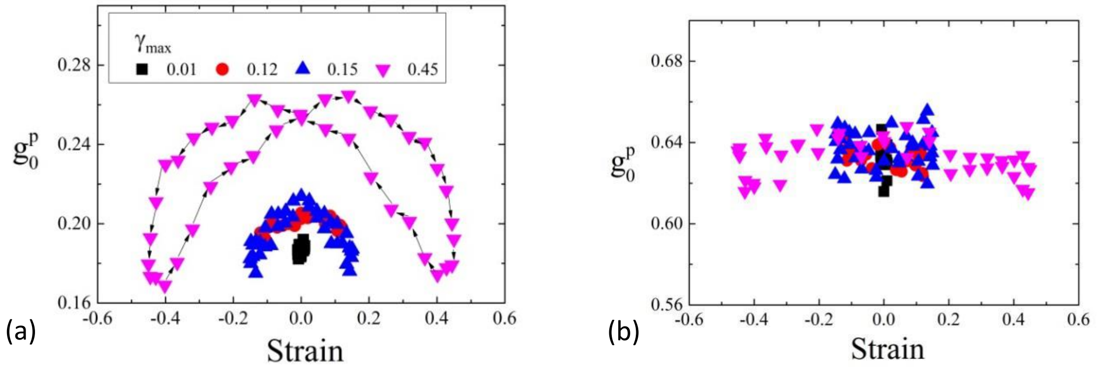

Figure 6.7: Non-affine displacement (NAD) of the monomer beads for the nanocomposite (a) and the unfilled polymer (b). The dependence of the NAD on strain is depicted for four different values of the strain amplitude. Each point on the graph denotes the NAD of the monomer beads between two consecutive strain values.

The calculated NAD implies that, at zero strain, increasing γ_{max} led the monomer beads to a higher mobility, which seems to correspond to the observed strain softening with increasing γ_{max} (i.e., the Payne effect). However, when $\gamma = \gamma_{max}$, the NAD of the monomer beads was independent of γ_{max}. In particular, the higher the value of γ_{max}, the more abrupt was the drop in the NAD of the monomer beads, so that when $\gamma = \gamma_{max}$ the mobility of the monomer beads was the same for all different values of γ_{max}. The decreased mobility of the monomer beads at high values of strain seem to correspond to the observed strain hardening.

Moreover, at $\gamma_{max} = 0.45$, the component of the radius of gyration of the polymer chains along the deformation direction attained a maximum value of $R_{gx}^2 = 16\sigma$ (Fig. 6.8), in both the nanocomposite and the unfiled polymer; the components of the R_g along the lateral directions were not noticeably affected by the strain (not shown). At equilibrium conditions we calculated $R_{gx}^2 \approx 4\sigma$. Therefore, during the deformation simulations, the chains were highly stretched along the strain direction. On average, the radius of gyration of the polymer chains in the nanocomposite was smaller than that of the polymer chains in the unfilled polymer. This difference implies that the NPs acted as weak crosslink junctions which inhibited to a small degree the stretching of the polymer chains. Lastly, from a comparison among Figs. 6.6 and 6.8 it can be seen that the strain hardening appeared once the R_{gx}^2 of the nanocomposite became larger than the R_g^2 of the Gaussian coil (about 8.33σ) [**25**].

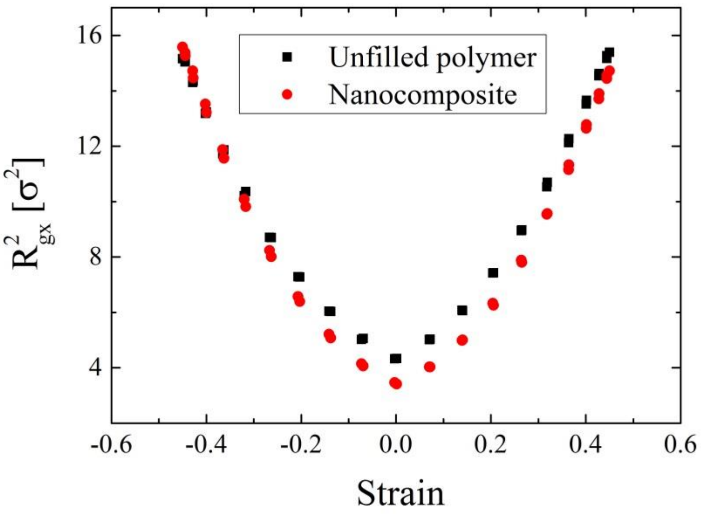

Figure 6.8: The radius of gyration of the polymer chains in the nanocomposite and the unfilled polymer as a function of the applied strain at $\gamma_{\max}$ = 0.45.

Since the interaction among monomers and NPs was attractive, we should expect that the relaxation times of the monomer beads will be higher in the composites than in the unfilled polymer. To this end we calculated the means-squared displacement for both the monomer beads and the NPs. At very short times ($0.01\tau - 0.1\tau$) a ballistic regime with a slope close to two is commonly distinguished in the MSD. The ballistic regime is followed by a plateau, where the tagged monomer is trapped in a cage created by its neighboring monomers. As soon as the monomer escapes from the cage after some characteristic time τ_α (the α-relaxation time [**26, 27**]) the diffusive Rouse regime follows, with an exponent of 0.5.

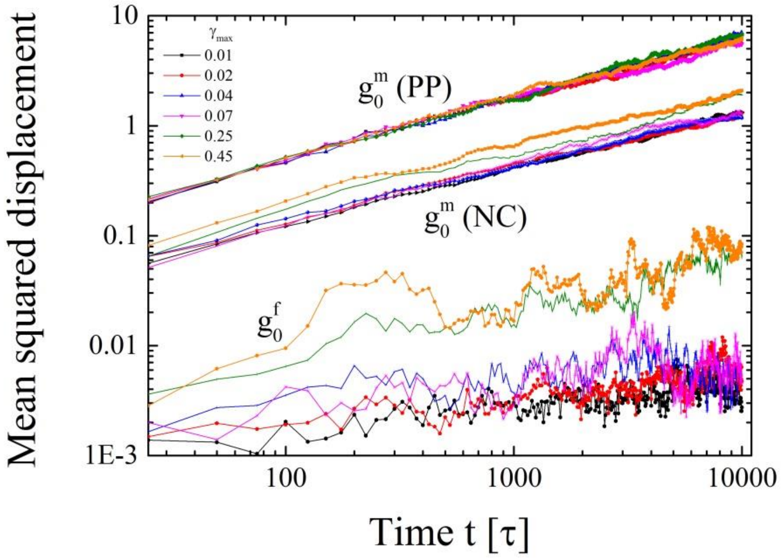

Figure 6.9: Instantaneous mean squared displacement of the monomer-beads, g_0^m, and of the filler-beads, g_0^f, in the pure polymer (PP) and in the nanocomposite (NC).

The slope of the mean squared displacement (MSD) of the monomer beads (Fig. 6.9) was calculated equal to about 0.68 both in the unfilled polymer and in the composite. This is larger than the Rouse exponent normally expected, probably due to the small length of the simulated chains. Furthermore, the timescale of the cage-escape was apparently less than 10τ; the Rouse time, *i.e.*, the time within which linear (not sub-linear) dependence should be expected, was surely longer than 10,000τ; and the characteristic deformation time at $\omega = 0.0063\tau^{-1}$ was about 300τ. Hence, the relaxation time of the monomer-beads was longer than the characteristic deformation time, and therefore we conclude that the relaxation time of the polymer chains' COM was much longer than the characteristic time of deformation. This means that the system was always out of equilibrium (rather than being close to equilibrium) during the deformation. We note that the statistical quality of the curves in Fig. 6.9 is worse than what it would have been had we taken into account multiple initial times in the calculation of the MSD.

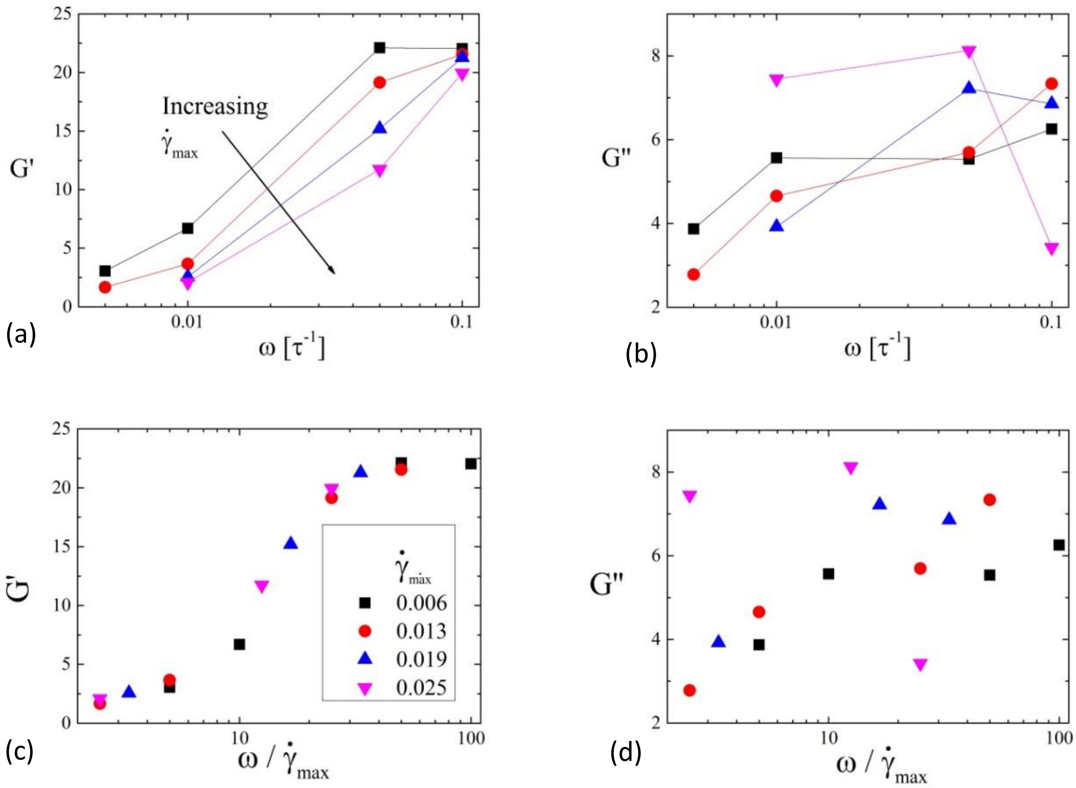

Figure 6.10: Elastic and viscous modulus versus (a, b) the angular frequency and (c, d) the inverse strain amplitude. Each curve corresponds to a specific value of the maximum strain rate.

Since the controlling time of the simulations was the characteristic deformation time, and not an intrinsic time of the deformed system, we expected to be able to create a master curve for the dependence of the moduli on the oscillation frequency, $G^*(\omega)$ [**12**]. Apparently, the maximum shear rate, $\dot{\gamma}_{max} = \omega\gamma_{max}$, emerged as the important variable for the construction of the master curve. By plotting the moduli as a function of the angular frequency for different values of $\dot{\gamma}_{max}$, we observed that the elastic and viscous modulus depended on the value of ω (Fig. 6.10a-b). Most importantly, though, the curves of Fig. 6.10a seemed to be parallel to each other, which implies that a master curve may be created for G' under different values of $\dot{\gamma}_{max}$. That was not the case for G'' (Fig. 6.10c-d), for which the data points were more scattered than those of G', although a trend can still be seen if the data points at the highest $\dot{\gamma}_{max}$ are ignored owing to their peculiar behavior of decreasing sharply at the maximum ω that was employed in the simulations. The shifting factor for creating the master curve was the inverse strain amplitude $\gamma_{max}^{-1} = \omega\dot{\gamma}_{max}^{-1}$. Hence, the dominant time scale in the nonlinear regime of stress response was the one imposed by the time frequency of oscillations, *i.e.*, $1/\nu = 2\pi/\omega$ [**12**].

6.5 Microscopic mechanisms of the Payne effect

Following the study of Chapter 5 on the effect of the NP interactions on the reinforcement of the simulated polymer nanocomposites, we probed in this Chapter the effect of NP interactions on the loss of that reinforcement, namely, on the Payne effect [**11, 14**]. To this end we calculated the elastic and viscous moduli as a function of the strain amplitude for the composites with attractive and repulsive NP-NP interactions (Fig. 6.11). It is obvious that the reinforcement was higher in the nanocomposite with attractive rather than repulsive NP-NP interactions, with a higher reinforcement leading to a more pronounced drop in the elastic modulus with increasing strain amplitude. The maximum value of the viscous modulus was larger when attractive NP-NP interactions were used. At the same time, that maximum was observed at a higher strain amplitude in the composite with attractive NP-NP interactions than in that with repulsive ones.

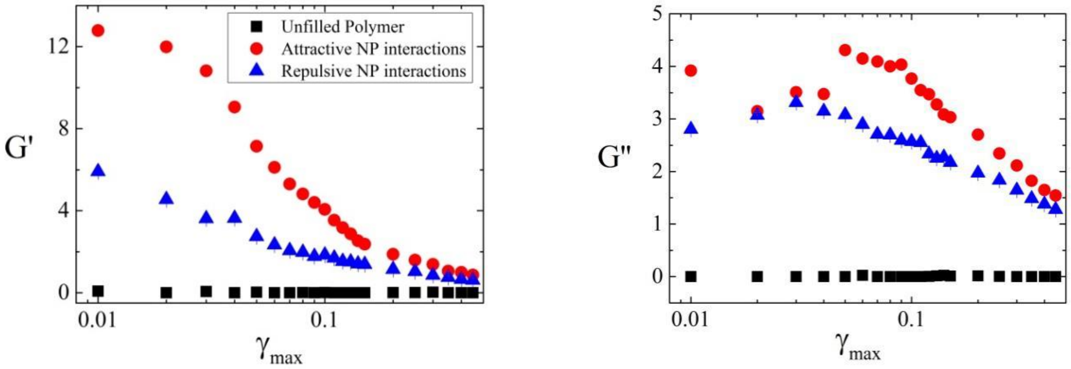

Figure 6.11: Payne effect for the unfilled polymer and the nanocomposite with attractive and repulsive NP interactions.

In Figs. 6.12 and 6.13 we have plotted the spatial profiles of the instantaneous MSD (consisting of random and convective motions) of the monomer beads for the composite with attractive and repulsive NP interactions, respectively. Depending on the values of the strain amplitude, there were four to five different dynamical layers of polymer between the NPs. As it has been already shown experimentally for glassy polymers, increasing the strain amplitude led to a narrower spatial distribution of relaxation times of the polymer segments [**28**].

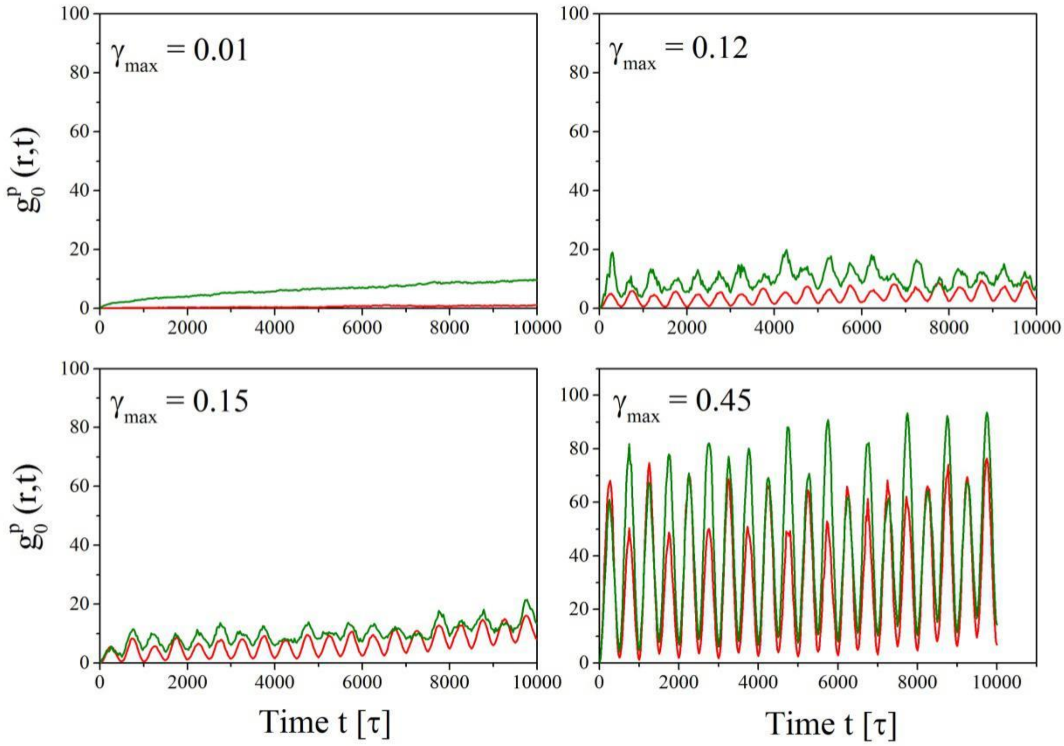

Figure 6.12: Spatial profiles of the instantaneous MSD (consisting of random and convective motion) of the monomer beads in the composite with *attractive* NP-NP interactions. Only the first and last layers are shown so as to better illustrate the effect of the strain amplitude on the dynamic heterogeneity of the polymer matrix.

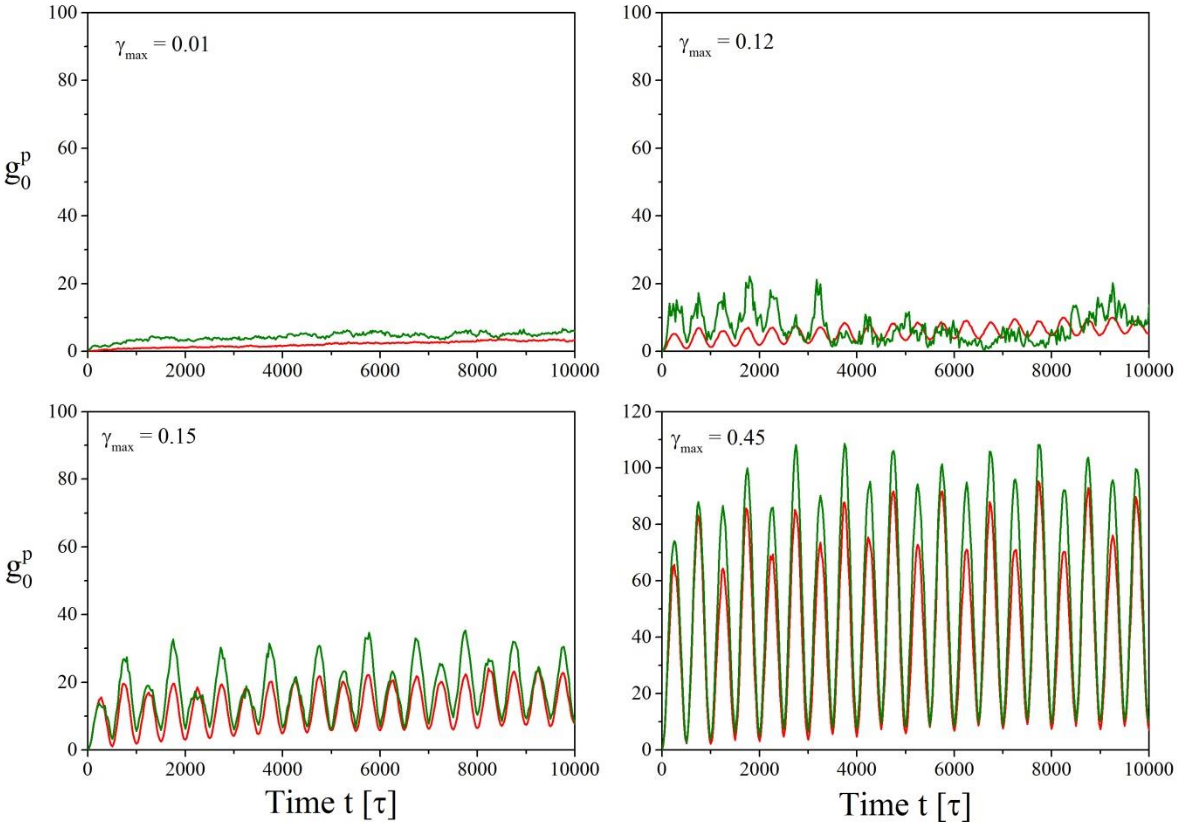

Figure 6.13: Spatial profiles of the instantaneous MSD (consisting of random and convective motions) of the monomer beads in the composite with *repulsive* NP-NP interactions. Only the first and last layers are shown so as to better illustrate the effect of the strain amplitude on the dynamic heterogeneity of the polymer matrix.

Apparently, when attractive NP-NP interactions were used, at very low strain amplitudes there was an immobile polymer layer ($g_0^p \approx 0$) surrounding the NPs, which broke down (*i.e.*, g_0^p became larger than zero) as the strain amplitude was increased (Fig. 6.14). At $\gamma_{\max} = 0.01$, this glassy layer had an average width of about 2σ. When repulsive interactions were used, no immobile polymer layer was detected: the mobility of the monomers nearest to the NPs was larger than zero, but the difference in mobility among the layers was smaller when repulsive rather than attractive interactions were used (albeit to a small degree). As a consequence, while the strain amplitude was increased, higher dynamic heterogeneity was observed in the nanocomposite with attractive rather than repulsive NP interactions. It seems, then, that the NP interactions modified the dynamical properties of the polymer matrix, as well as its structural properties (as was affirmed in Chapter 5).

6.6 Conclusions

The main aim of this work has been to elucidate the contradictory behavior of polymer nanocomposite to exhibit both strain hardening and strain softening behavior under LAOS experiments. To this end we performed Molecular-Dynamic simulations of a model nanocomposite and concluded that the observed strain hardening arose from the decrease in the non-affine displacement of the polymer segments of the matrix which were caused by the extreme elongation of the polymer chains along the deformation direction. We also affirmed that the controlling timescale of the simulations was the deformation time, not any intrinsic timescale of the system. Furthermore, we studied the effect of using attractive versus repulsive interactions among the nanoparticles on the Payne effect. The simulation results showed that the reinforcement and its subsequent drop with increasing strain amplitude were higher in the nanocomposite with attractive rather with repulsive NP interactions. Probing the mean-square displacement of the monomer beads as a function of the distance from the NPs’ surface, we saw the presence of a glassy polymer layer surrounding the NPs when attractive NP interactions were used, but that glassy layer was not observed when repulsive NP interactions were used. Lastly, the use of attractive NP interactions enhanced the dynamic heterogeneity of the polymer matrix in comparison with that when repulsive NP interactions were used, which corresponded to the higher reinforcement and Payne effect observed in the former than in the latter system. It seems, then, that the NP interactions modified both the structural (Chapter 5) and dynamical properties of the polymer matrix. Further studies should involve the usage of additional values for the filler volume fraction and the radius of the NPs, to further affirm the general applicability of the currently presented results presented.

References

[1] Giannelis E.P., *Adv. Mater.*, **1996**, *8*, pp. 29–35.

[2] Ray S.S., Okamoto M., *Prog. Polym. Sci.*, **2003**, *28*, 1539–1641.

[3] Tjong S.C., *Mater. Sci. Eng. R*, **2006**, *53*, 73–197.

[4] Zhu A. J. Sternstein S. S., *Compos. Sci. Technol.*, **2003**, *63*, 1113–1126.

[5] Samet Varol H., Alejandra Sánchez M., Lu H., Baio J. E., Malm C., Encinas N., Mermet-Guyennet M. R. B., Martzel N., Bonn D., Bonn M., Weidner T., Backus E. H. G., Parekh S. H., *Macromolecules*, **2015**, *48,* 7929–7937.

[6] Allegra G., Raos G., Vacatello M., *Prog. Polym. Sci.*, **2008**, *33*, 683-731.

[7] Moll J. F., Akcora P., Rungta A., Gong S., Colby R. H., Benicewicz B. C., Kumar S. K., *Macromolecules*, **2011**, *44*, 7473-7477.

[8] Long D., Sotta P., *Rheol. Acta*, **2007**, *46*, 1029 – 1044.

[9] Cagliardi S., Arrighi V., Fergusson R., Telling M. T. F., *Physica B: Condens. Matt.,* **2001**, *301,* 110-114.

[10] Mermet-Guyennet M. R. B, de Castro J. G. , Habibi M., Martzel N., Denn, D. Bonn M. M., *J. Rheol.,* **2015**, *59*, 21-32.

[11] Payne, A. R., *J. Appl. Polym. Sci.,* **1965**, *9,* 2273–2284.

[12] Wyss H. M., Miyazaki K., Mattson J., Hu Z., Reichman D. R., Weitz D., *Phys. Rev. Lett.*, **2007**, *98,* 238303.

[13] Kumar K., Jouault N., *Macromolecules,* **2013**, *46*, 3199-3214.

[14] Raos G., Moreno M., Elli S., *Macromolecules*, **2006**, *39,* 6744-6751.

[15] Gavrilov A. A., Chertovich A. V., Khalatur P. G., Khokhlov A. R., *Macromolecules*, **2014**, *47,* 5400.

[16] Kutvonen A., G. Rossi, T. Ala_Nissila, *Phys. Rev. E*, **2012**, *85*, 041803.

[17] Kutvonen A., Rossi G., Puisto S. R., Rostedt N. K. J., Ala-Nissila T., *J. Chem. Phys.*, **2012**, *137,* 214901.

[18] Litvinov V. M., Orza R. A., Kluppel M., van Duin M., Magusin P. C. M. M., *Macromolecules*, **2011**, **44**, 4887 – 4900.

[19] Hagita K., Morita H., Doi M., Takano H., *Macromolecules*, **2016**, *49,* 1972-1983.

[20] Chen Y., Li Z., Wen S., Yang Q., Zhang L., Zhong C., Liu L, *J. Chem. Phys.*, **2014**, *141*, 104901.

[20] Wang L., Zheng Z., Davris T., Li F., Liu J., Wu, L. Zhang L., Lyulin A. V., *Langmuir,* **2016**, *32*, 8473-8483.

[21] Li J., Zhang L., Cao D., Wang W., *Phys. Chem. Chem. Phys*., **2009**, *11*, 11365-11384.

[22] Liu J., Gao Y., Cao D., Zhang L., Guo Z., *Langmuir*, **2011**, *27*, 7926-7933

[23] Evans D. J., Morriss G. P., *Statistical Mechanics of Non-equilibrium Liquids,* Academic Press: London 1990.

[24] Hyun K., Wilhelm M., Klein C. O., Cho K. S., Nam J. G., Ahn K. H., Lee S. J., Ewoldt R. H., McKinley G. H., *Prog. Polym. Sci*., **2011**, *36*, 1697–1753.

[25] Rubinstein M., Colby R. H., *Polymer Physics*, Oxford University Press: Oxford 2003.

[26] Leutheusser E., *Phys. Rev. A* **1984**, *29*, 2765–2773.

[27] Hansen J. P., Levesque D., Zinn-Justin J., *Liquids, Freezing and the Glass Transition*, North Holland: Amsterdam 1991.

[28] Lee H-N, Paeng K., Swallen S. F., Ediger M. D., *Science*, **2009**, *323*, 5911.

[29] Kwang Soo Cho, Kyu Hyun, Kyun Hyun Ahn, Seung Jong Lee, *J. Rheol*., **2005**, *49*(3), 747-758.

Chapter 7

Conclusions and Outlook

Abstract

Various experimental and computational studies have shown that polymers under nanoscale confinement or filled with rigid nanoparticles exhibit distinct structural, dynamical and mechanical properties from the pure polymer matrix. The main goal of the thesis was to study the effect of the film thickness and the crosslink density on the dynamical and mechanical properties of polymers confined between solid walls, as well as the mechanical properties of filled elastomers as they are affected by the volume fraction and size of the filler particles and by the nature of the interactions among the nanoparticles; namely the enhancement of the rigidity at small strain amplitudes, and its corresponding loss with increasing strain amplitude. To this end we performed molecular-dynamics simulations using coarse-grained models so as to explain universal mechanisms of the probed properties of the simulated systems. In this chapter we summarize the main conclusions of the thesis and propose perspectives for future studies.

Chapter 3: Molecular-dynamics simulations of crosslinked polymer films: equilibrium structure and glass-transition temperature

The Chapter deals with the equilibrium structural study of polymer films, capped between two crystalline walls. Attractive polymer-wall interactions were employed. Three different film thicknesses were used, which were larger, smaller, and about the same order of magnitude with the end-to-end distance of the chains in the non-confined polymer. Our goal was to understand how the film thickness and the polymer crosslink density affect the structural properties of the confined polymer.

- The relative effect of the degree of confinement and the crosslink density has been studied. The main conclusion of this chapter is that confining the polymer matrix leads to a larger increase of its glass-transition temperature than the increase which is induced by the incorporation of chemical crosslinks.
- In the direction perpendicular to the walls, the polymer displayed solid-like structure, whereas in the direction parallel to the walls, it displayed an amorphous structure similar to that of the non-confined polymer.

Chapter 4: A coarse-grained molecular-dynamics study of segmental structure and mobility in capped crosslinked copolymer films

The Chapter deals with the equilibrium dynamical study of the polymer films presented in the previous Chapter, and specifically of the segmental dynamics as a function of film thickness and mesh size (the end-to-end distance of the sub-chains in the crosslinked polymer networks). Our goal was to see the relative effect of both crosslinking and confinement on segmental mobility.

- The main conclusion of this chapter is that the polymer dynamics in films with attractive walls (and by extension the mechanical properties of the films) are controlled by the concentration of monomers at the wall-polymer interface.
- Increasing the degree of confinement and the crosslink density resulted in a monotonic slowing-down of segmental mobility on all studied

length-scales (and an increase of the glass-transition temperature), an increased concentration of monomers at the wall-polymer interface, and in a higher dynamic heterogeneity.

- The high concentration of monomers close to the crystalline walls decreased when the crystalline walls were replaced with non-crystalline ones.

Chapter 5: Filler size effects on reinforcement in elastomer-based nanocomposites: experimental and simulational insights into physical mechanisms

This Chapter deals with the study of the reinforcement in the polymer films of the previous Chapters as well as in polymers filled with rigid nanoparticles. All simulated systems were elongated under a linearly increased strain. The varying parameters for the filled polymer systems were the volume fraction and size of the nanoparticles. We also compared the reinforcement which was calculated by our simulation results with predictions of shear distortion models commonly used in industry. Our goal was to affirm the validity the simulation models in predicting the qualitative behavior of polymer nanocomposites, and provide a microscopic picture for the observed macroscopic mechanical properties of the simulated polymer nanocomposites.

- The main conclusion is that nanoparticle-nanoparticle interactions played a “modifying” role in regards to the structural properties of the polymer matrices in the particulate systems, and in the case of repulsive interactions, they induced different hydrodynamic interactions from what was expected by the shear-distortion models.
- The reinforcement (*R*) increased with decreasing radius of the nanoparticles and attractive nanoparticle interactions, with the latter having a larger effect than the former.
- A higher filler volume fraction led to the densification of the matrix at the filler-matrix interfaces, and had a noticeable effect on the *R* only when attractive nanoparticle-nanoparticle interactions were employed.

Chapter 6: Molecular Mechanisms of the Payne Effect in Filled Elastomers: Insights from Computer Modeling

The two goals of this Chapter has been, first, to elucidate the microscopic mechanisms of the strain hardening and strain softening observed in polymer nanocomposite exposed to LAOS experiments, and second, to probe the microscopic causes of the Payne effect while varying the type of nanoparticle interactions. To this aim we exposed the systems of the previous chapter to oscillatory shear deformation.

- The main conclusion is that the controlling timescale of the simulations was the deformation time, not an intrinsic timescale of the system, i.e., our systems were out of equilibrium and controlled by extrinsic conditions.
- Indiscriminate fit of high-order harmonics in LAOS may lead to erroneous conclusions.
- The strain hardening produced by LAOS simulations is an intrinsic property of the polymer matrix, but it is further enhanced by the presence of the nanoparticles (NPs).
- The main conclusion on local mobility was that the strain hardening observed in LAOS experiments arose from the decrease in the non-affine displacement of the polymer segments of the matrix which were caused by the extreme elongation of the polymer chains along the deformation direction.
- The reinforcement and the subsequent softening (*i.e.*, the Payne effect) with increasing strain amplitude were higher in the nanocomposite with attractive rather with repulsive NP-NP interactions. An immobile polymer layer surrounded the NPs at low strain amplitudes only when attractive NP-NP interactions were used.
- Attractive NP-NP interactions enhanced the dynamic heterogeneity of the polymer matrix in comparison with that when repulsive NP-NP interactions were used, which corresponded to the higher reinforcement and Payne effect observed in the former than in the latter system.

General Conclusions and Outlook

Overall, a smaller film thickness (which ideally corresponds to a higher volume fraction or smaller size of fillers) leads to smaller polymer-density variations, higher dynamic fragility, higher dynamic heterogeneity, and a larger reinforcement. This might indicate that, besides the effect of using a constant number of nanoparticles with larger size-dispersity, inhomogeneity in the polymer properties of the matrix might be brought about also by an increasing amount of nanoparticles with uniform size. Additionally, when crystalline walls were replaced by rough ones, the structural inhomogeneity and the dynamic heterogeneity of the polymer decreased. The reinforcement followed the same trend.

The same observations were made in the particulate systems when a higher volume fraction of fillers, or attractive — as opposed to repulsive — nanoparticle interactions were used. Therefore, there seems to be a one-to-one correspondence among the reinforcement and the dynamic heterogeneity of the polymer in the simulated films and particulate systems. This observation is in agreement with experimental results of our collaborators at the University of Amsterdam, according to which a higher polydispersity of the NPs' — which increases the inhomogeneity of the polymer matrix — retained the reinforcement and, at the same time, decreased the Payne effect.

Therefore, the further and more detailed study of the effect of structural inhomogeneity and dynamic heterogeneity of the polymer matrix, as well as the development of new methods for their control, is deemed to be a promising research route on which to focus in future studies of the mechanical properties of polymer nanocomposites. To this end, a larger parameter space of the filler volume fraction and the radius and dispersity of the nanoparticles should be studied, so as to increase the reliability of the conclusions presented in this chapter.

Further studies of the connection between the wall-roughness, the corresponding slowing-down of the dynamics, and the final connection of these with the mechanical reinforcement and the Payne effect in thin polymer films is highly desirable. Our results on the current stage cannot provide definite answers to these questions. Therefore a more extended study should be performed in this regard.

The Payne effect is highly important for the rubber industry. Therefore the incorporation of chemical crosslinks in the particulate models that were utilized in the simulations, besides enriching the overall knowledge about polymer-based composites, would also provide additionally insight specifically directed to the rubber industry.

Lastly, the mechanical properties of polymer nanocomposites pose a multiscale problem, for the impact of specific length-scale phenomena is yet to be clearly elucidated. A multiscale study should therefore provide us with further insight on the mechanisms that give rise to the non-linear viscoelastic properties of filled polymers. The models that we used in this thesis were simple bead-spring models which allow avoiding chemical details and performing large scale computer simulations. Smaller length scales should be considered in future studies by simulating chemically specific polymers, which would allow an immediate comparison among simulations and experimental studies. On the other hand, the insight which was gained by our Molecular-Dynamics simulations can be used to determine parameters for more coarse-grained simulations so that larger length-scales can be reached.

Summary

Coarse-grained molecular-dynamics simulations of segmental motion and mechanical properties in polymer films and nanocomposites

The aim of the project was to study the mechanical properties of polymer nanocomposites (PNC), in cooperation with the UvA and the industrial partners Michelin (tires) and SKF (rubbery sealants). PNC are materials in which inorganic nanoparticles (NP), commonly referred to as fillers, are added to a polymer matrix so as to increase their rigidity at low strain amplitudes. This enhancement of rigidity is colloquially called reinforcement. However, at higher strain amplitudes, an abrupt decrease of the reinforcement is observed, which is accompanied by an increase of viscous losses — this is the so-called "Payne effect" which restrains the performance of this family of materials as well as the development of possible new applications. The goal of the project was to connect the viscoelastic properties of the materials with their microstructure, and the microstructure with the interactions among the polymer and the NPs at the molecular scale. This could lead to the design of new materials with tailored specific mechanical properties through the tuning of the molecular interactions.

We performed coarse-grained molecular-dynamics simulations on two different types of systems: a polymer film capped between two solid walls, and a polymer matrix filled with NPs. Our goal was to investigate the effect of the molecular interactions, the degree of polymer confinement, the polymer crosslink density, the filler particle size, and the filler volume fraction, on the equilibrium and non-equilibrium structure and dynamics, and on the mechanical properties of the simulated systems. The most important results are briefly mentioned below.

We observed that the degree of confinement did not influence the equilibrium structure of the polymer along the direction parallel to the wall of the film, whereas it induced the development of density layers along the perpendicular direction. The increased glass-transition temperature (T_g) under stronger confinement could be attributed to the slow relaxation of monomers that lie close to the crystalline substrates, in comparison with the faster and bulk-like relaxation in the middle layers of the film — these slowly relaxing further layers gradually enclosed a larger volume fraction of the film as the

film thickness was decreased. The glass-transition temperature displayed a steep increase once the crosslink mesh-size became smaller than the radius of gyration of the bulk chains — this was accompanied by a monotonic slowing-down of segmental dynamics on all studied length-scales, as quantified by the decay of the incoherent-scattering function. These observations could be attributed to the smaller maximum attainable displacement of the monomer units and to the decreased width of the bulk density layer in thinner films. Higher dynamic heterogeneity was also observed when smaller values of film thickness and mesh-size were used, with more fragile glass-forming films displaying larger T_g values.

Concerning the NP-filled polymer systems, we observed similarities among our simulation results and the experimental results of our collaborators, which allowed for a more detailed study of the causes of the reinforcement observed in experimental samples through the study of the structural and dynamical properties of the simulated systems. We observed an increase up to 50% in the elastic modulus when NPs were added to the polymer matrix. Furthermore, in systems with attractive NP interactions, the reinforcement sharply increased when attractive NP interactions were employed and the average distance between the surfaces of the NPs was smaller than the Lennard-Jones cut-off radius: a strong indication that the development of a filler network is an important source of reinforcement for large volume fractions of fillers. On the other hand, at low filler volume fractions the reinforcement of the particulate systems with attractive NP-NP interactions was similar to that of systems with repulsive NP-NP interactions. This indicates that at low filler volume fractions, indirect (i.e., matrix-mediated) interactions among the NPs are more relevant than direct NP-NP interactions. A higher filler volume fraction resulted in a smaller distance between the NPs, and in a densification of the monomer units at the filler-polymer interface. As a consequence, a higher filler fraction resulted in a more confined polymer matrix and a slower diffusion of the monomer beads. Last, the development of a NP network was evidently more important in increasing the reinforcement than the use of a smaller NP radius.

In order to study the Payne effect, we performed large amplitude oscillatory shear (LAOS) simulations. The simulations showed that the controlling timescale of the simulations was the deformation time and not an intrinsic timescale of the system, i.e., our systems were out of equilibrium and controlled by extrinsic conditions. Furthermore, we probed the microscopic causes of the observed strain hardening at large strain values: according to the simulation results, the strain hardening observed in LAOS experiments arose from the decrease in the non-affine displacement of the polymer segments of the matrix which were caused by the extreme elongation of the polymer chains along the deformation direction. Lastly, we found that attractive NP interactions enhanced the dynamic heterogeneity of the polymer matrix in comparison with that when repulsive NP interactions were used, which corresponded to the higher reinforcement and Payne effect observed in the former than in the latter system.

The main conclusions of this work are that the mechanical properties of polymer systems filled with NPs are mostly affected by the direct and polymer-mediated NP interactions, and that a higher volume fraction of NPs increases both the reinforcement and the dynamic heterogeneity of the confined polymer matrix.

Curriculum Vitae

Theodoros Davris was born on 14th of August 1982 in Athens, Greece. After finishing his high-school education, he was admitted to the Aristotle University of Thessaloniki to study Chemical Engineering. During his undergraduate education his interests were in chemical-process design and simulation. He obtained his engineering degree in 2012 after completing his graduation thesis on scientific-software development for the simulation and control of a polymerization reactor, under the supervision of Prof. Costas Kiparissides. In 2013 he moved to the Eindhoven University of Technology to work as a PhD student in the group Theory and Simulation of Polymers and Soft Matter, under the supervision of dr. A.V. Lyulin and prof. dr. M.A.J. Michels. The results of his PhD research are described in this dissertation, and they have been published at international conferences and in scientific journals.

List of Publications

Davris T., Lyulin A., Mermet-Guyennet Marius R.B., Bonn D., Filler size effects on reinforcement in elastomer-based nanocomposites: experimental and simulational insights into physical mechanisms, *Macromolecules*, **2016**, *49* (18), 7077–7087.

Wang L., Zheng Z., Davris T., Li F., Liu J., Wu Y., Zhang L., Lyulin A.V., Influence of morphology on the mechanical properties of polymer nanocomposites filled with uniform or patchy nanoparticles, *Langmuir*, **2016**, *32* (33), 8473–8483.

Davris T., Lyulin A.V., Coarse-grained molecular-dynamics simulations of capped crosslinked polymer films, *Polymer Composites*, **2015**, *36* (6), 1012.

Davris T., Lyulin A.V., A coarse-grained molecular dynamics study of segmental structure and mobility in capped crosslinked copolymer films, *Journal of Chemical Physics*, **2015**, *143*, 07490.

Acknowledgements

The work presented in this thesis would not have been possible without close professional associations with many different persons. I take this opportunity to acknowledge them and express my sincere gratitude for helping me in the completion of the Ph.D. thesis.

Primarily, I thank my research supervisors, dr. Alexey Lyulin and prof. dr. Thijs Michels, for contributing immensely to the completion of the thesis with their assistance and dedicated involvement in every step throughout the process. I express my gratitude for their support and understanding over the past four years. Special thanks belong to Alexey for his daily help and support.

I would also like to express the deepest appreciation to my committee members, Dr. Arlette Baljon, prof. dr. Peter. Bobbert, prof. dr. Daniel Bonn, Dr. Angelo Simone, and prof. dr. Federico Toschi, for reading and approving the thesis, and for their insightful comments.

I would like to thank Dr. Marius Mermet-Guyennet, Nicolas Martzel, Prof. Florian Müller-Plathe, Prof. Doros N. Theodorou, dr. Hans Wyss, dr. Babak Hosseinkhani, and Dr. Kostas Karatasos, for our fruitful discussions.

Last, I thank all the members of my group for helping me in one way or another, and especially Dr. Chrysostomos Batistakis for his daily scientific help during the first year of my PhD project.